An Exploration of the Effects of Clouds on the Characterization of a Remote Earth

A Thesis

submitted to

Indian Institute of Science Education and Research Pune
in partial fulfillment of the requirements for the
BS-MS Dual Degree Programme
by

Soumil Kelkar

Indian Institute of Science Education and Research Pune
Dr. Homi Bhabha Road,
Pashan, Pune 411008, INDIA.

May, 2024

Supervisor: Ravi Kopparapu and Prabal Saxena
Co-supervisor: Joy Monteiro
© Soumil Kelkar 2024

Certificate

This is to certify that this dissertation entitled **An Exploration of the Effects of Clouds on the Characterization of a Remote Earth** towards the partial fulfilment of the BS-MS dual degree programme at the Indian Institute of Science Education and Research, Pune represents work carried out by Soumil Kelkar at NASA Goddard Space Flight Center and the Indian Institute of Science Education and Research, Pune, under the supervision of Ravi Kopparapu and Prabal Saxena, Solar System Exploration Division, NASA Goddard Space Flight Center with Joy Monteiro, Department of Earth and Climate Science, Indian Institute of Science Education and Research, Pune, as a co-supervisor, during the academic year 2023-2024.

Ravi Kopparapu   Prabal Saxena   Joy Monteiro

Committee:

Ravi Kopparapu

Prabal Saxena

Joy Monteiro

Prasad Subramanian

Declaration

I hereby declare that the matter embodied in the report entitled **An Exploration of the Effects of Clouds on the Characterization of a Remote Earth** are the results of the work carried out by me at the Solar System Exploration Division, NASA Goddard Space Flight Center, and the Department of Earth and Climate Science, Indian Institute of Science Education and Research, Pune, under the supervision of Ravi Kopparapu and Prabal Saxena, Solar System Exploration Division, NASA Goddard Space Flight Center, with Joy Monteiro, Department of Earth and Climate Science, Indian Institute of Science Education and Research, Pune, as a co-supervisor, and the same has not been submitted elsewhere for any other degree. Wherever others contribute, every effort is made to indicate this clearly, with due reference to the literature and acknowledgement of collaborative research and discussions.

Soumil Kelkar

IISER Roll no.: 20191091

Date: 14th March 2024
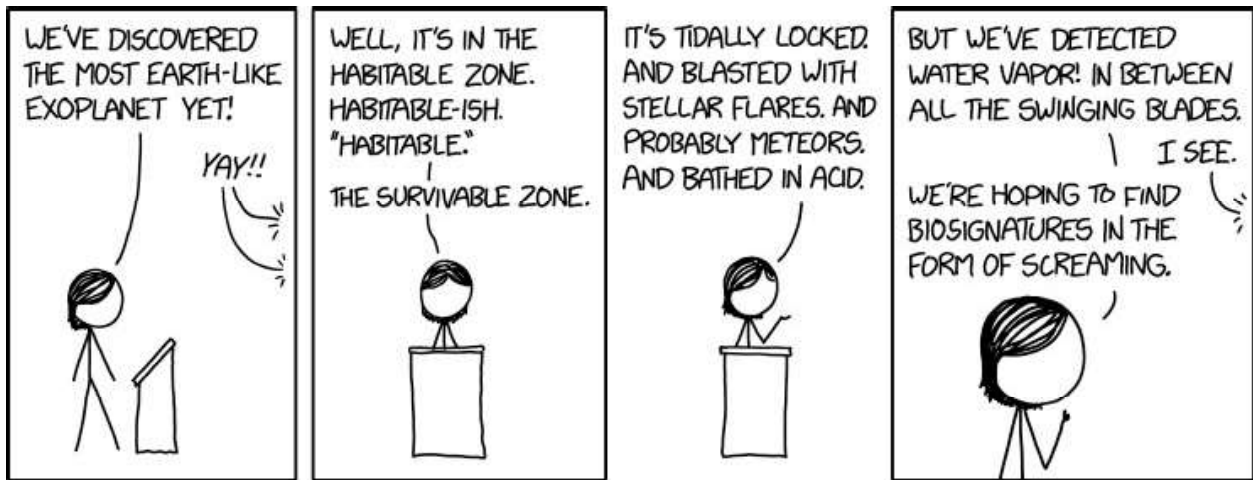
This thesis is dedicated to finding aliens.

Acknowledgements

I am immensely grateful to my supervisors Ravi Kopparapu and Prabal Saxena for their amazing support throughout the duration of my thesis. Their professional as well as personal guidance was a huge help not only in my research work but in general as well and I appreciate all that they have done for me, especially during my stay in the U.S. I was just an amateur with an interest in exoplanets and they made me passionate about pursuing research in this field and also helped me mature as a researcher. Thank you for inviting me to spend a few months at NASA Goddard and for connecting me with the other amazing people who work there. Thank you for making me feel at home and for providing me with constant encouragement in our weekly meetings which pushed me to do amazing research. Thank you for being my number-one support system when I was living alone in a completely new country. Thank you for inviting me to your home during festival seasons and thank you for taking me out for beer and brisket. I couldn't have asked for a better pair of advisors to supervise my research, thank you for everything.

I have been working with Joy for about a few years now and he has always been kind, supportive, and in general, very calm and chill. He supervised my first ever research project, on computational epidemiology (yes he does that too), which started as a cute summer-time project and has now blossomed into an extensive paper tackling the intricacies of public health responses during an epidemic. He introduced me to Ravi and Prabal and I will always be grateful to him for that. I was extremely glad of his expertise in atmospheric science and I acknowledge all the valuable inputs he has provided throughout this project. I would also like to extend my gratitude to all of the amazing researchers at NASA Goddard, who showed interest in my work, held extensive discussions with me, and gave me valuable input. Specifically, I thank Vincent Kofman and Geronimo Villanueva for helping me out with PSG and in general always being there for me whenever I had any queries.

My life in IISER would have been incomplete without an amazing group of friends who have been there for me since day one. Abir, Aditi, Akshata, Arsh, Ashli, Asmita, Drishti, Parijat, Pradyun, Shivam, Vibha, and many others, we were a bunch of misfits who somehow found each other, but I consider you guys as my family now. We have been through so much together and I consider these 5 years as the best years of my life just because I had all of you. You have helped me grow so much as a person, helped me mature as an individual and

I would be nowhere without you. Going to classes and dining together, those daily visits to MDP at night, those long walks and gossip sessions, those daily afternoon coffee breaks, those nights spent vibing to Bollywood music, those video calls during lockdown birthdays, I am going to miss all of it. Here's to all the amazing memories which we have shared together and will hopefully share in the future as well, because honestly, I don't think I'll make such beautiful friends in my life ever again. I love you guys.

My stay in the U.S., however brief, was filled with amazing experiences, and it is all because of the wonderful community of people I found at NASA and at home. Ally, Ferris, Harrison, Michele, Thea, Kiet, and everyone else, thank you for everything you did for me. I was terrified of making new friends in a different country, but y'all made it so easy. Thank you for taking care of me, for driving me around everywhere, and for inviting me to your homes for some fun get-togethers. I hope y'all have amazing careers ahead, and hopefully, I'll see some of you in grad school. I am also extremely grateful to the NASA Peer community, and all the amazing mentors including Joe, Alex, Taylor, Erini, Jenna, Kristen, and of course, Katie, our work mom, who helped me through every step of the Ph.D. application process and provided me constant support and guidance in general as well.

Last but not least, I am extremely grateful to my parents, Mahesh and Nilima for everything they have done for me. I am who I am only because of their constant support and encouragement throughout my life and I cannot thank them enough for it. They gave me the freedom and stability to pursue my dreams, however unconventional they may be, and they have taken me out of some tough times whenever I felt like giving up. Every teenager goes through a phase where they hate their parents, so did I, but when you get older, you start to realize that they were right. They have made me into the kind of person I am today and I will always dedicate all my achievements to them. I still remember the teary smiles on their faces when I was leaving for NASA, I know it must have been terrifying to send your kid to a new country, but I hope I made you proud. I love you.

Funding & Financial Support

Abstract

The Habitable Worlds Observatory (HWO) is an upcoming mission concept based on the recommendation of the 2020 Astronomy and Astrophysics decadal survey. A primary goal of HWO is to identify and characterize Earth-like exoplanets through reflected light spectroscopy. However, a planet's spectrum is dynamic and only represents a time-dependent snapshot of its properties. Changing atmospheric conditions due to climate and weather patterns, particularly variation in cloud cover can significantly affect the spectrum in ways that complicate the understanding of a planet's baseline atmospheric properties. Variable cloud patchiness and cloud properties affect the detectability of atmospheric constituents, and also greatly influence the radiative transfer that determines a planet's spectrum. This has considerable implications for observations of potentially habitable exoplanets and thus it is critical to study and characterize the effects of clouds on their spectra. In this work, we construct an accurate model of a remote Earth using NASA's MERRA-2 dataset which assimilates data from a variety of satellites orbiting Earth. Utilizing the Planetary Spectrum Generator (PSG), we simulate observations of this remote Earth at different configurations using the HWO mission concepts. Our findings quantify the effects of clouds on the reflected light spectra as well as on the detectability of atmospheric constituents, specifically biomarkers like O_2, O_3, and H_2O. Through this work, we aim to develop a comprehensive suite of 'cloudy' spectra that will be vital in making accurate atmospheric retrievals and determining the optimal design specifications and observation strategies for the HWO mission.

Contents

Appendices 109

References 117

List of Tables

List of Figures

Part I

Introduction

Chapter 1

Exoplanets 101

1.1 Exoplanet demographics

Exoplanets are defined as planets present outside the Solar System that might be orbiting stellar hosts of their own. After the first detection of a planetary system in 1992 (Wolszczan and Frail, 1992) and the first detection of an exoplanet around a main sequence star in 1995 (Mayor and Queloz, 1995), more than 5500 exoplanets have been detected, as of today[1]. Figure 1.1 shows the mass/radius-period distributions of the exoplanets detected so far, with the Solar System planets also labeled for reference. The different methods of detection are color-coded. A quick glance at this plot reveals that there is a dearth of detected exoplanets which have properties similar to the Solar system planets, especially the inner rocky planets, including Earth. Most of these detected planets have masses and radii much bigger than Earth, similar to the outer giant planets. However, almost all of these planets have shorter orbital periods and a significant fraction of them have periods shorter than Earth, which means that they orbit much closer to their host star.

This radius-period distribution is used to categorize exoplanets into different classes, as shown in figure 1.2. In this plot, the stellar flux is a proxy for distance from the host star or the orbital period. Some important classes from this figure are (i) the rocky planets which include warm rocky planets like the Earth or hot rocky planets like Mercury or Venus (these planets are our main target for trying to detect habitable worlds outside our solar system),

---

[1]NASA Exoplanet Archive - https://exoplanetarchive.ipac.caltech.edu/
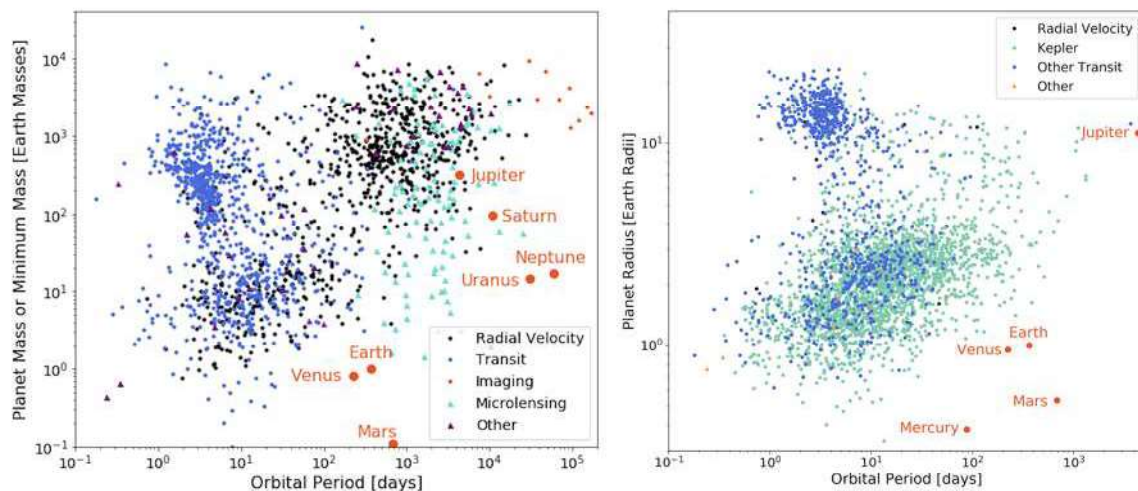
Figure 1.1: The demographics of the detected exoplanet population. The various detection methods are color-coded. Figure taken from Gaudi et al., 2021.

(ii) Super-Earths which are potentially rocky worlds which are more massive than the Earth but lighter than the ice giants Uranus and Neptune - no planets from this class exist in our Solar System, (iii) sub-Neptunes which form the upper limit of the Super-Earth class and are typically smaller than Neptune (although they might be more massive) and (iv) hot Jovians/Jupiters which are Jupiter-sized gas giants which orbit at short distances from their host star.

Referring to the classification scheme given in figure 1.2, an analysis of the exoplanet demographics shown in figure 1.1 reveals that the majority of the exoplanets detected so far belong to the classes of hot/warm Jupiters, sub-Neptunes and super-Earths - all three classes which have no analogs in our Solar System. This poses the question - how common is our Solar system architecture? The Solar system has rocky planets in the temperate zone and gas/ice giants farther out but observations show that a majority of the stars host close-in compact systems of hot Jupiters, super-Earths, and/or sub-Neptunes (Batygin and Laughlin, 2015; Dong and Zhu, 2013; Fang and Margot, 2012; Howard et al., 2012; Miguel et al., 2011; Youdin, 2011). The absence of Solar system analogs in the majority of planetary systems detected so far challenges our understanding of planetary formation and places important observational constraints on current theories of planetary formation. This also seems to suggest that our Solar system architecture is quite rare, however, our detection methods are not yet sensitive enough to detect Solar system analogs, so the jury is still out on the occurrence rates of planetary systems similar to our Solar System.
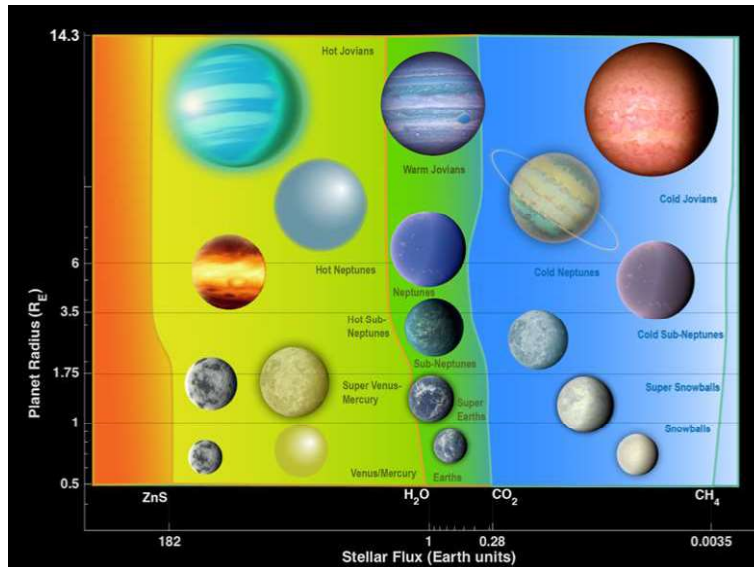
Figure 1.2: Exoplanets can be divided into different classes based on their radius and their orbital period/distance from the host star. The boundaries represent where different chemical species condense, according to equilibrium chemistry calculations. Figure taken from R.K. Kopparapu et al., 2020, with the classification boundaries described in R.K. Kopparapu et al., 2018.

1.2 Exoplanet detection methods

Exoplanets are too far away and too faint, thus they cannot be detected just by pointing a telescope at a region around a star. Their presence has to be directly inferred by identifying their effects on the host star, this is the basis for three widely used detection techniques - (i) radial velocity, (ii) transits, and (iii) microlensing. Some planets can be directly imaged as well, however, in these cases, the light from the star is blocked out by using a coronagraph, and then only the much fainter planets become visible. Figure 1.3 shows the distribution of exoplanets, color-coded by the techniques used to detect them. The radial velocity and transit techniques dominate this chart as it is comparatively easier to detect exoplanets using these techniques. Some of these techniques are briefly explained in the sections below.

1.2.1 Radial velocity technique

The radial velocity is one of the oldest techniques to be used to detect the presence of exoplanets. The first exoplanet detected around a main sequence star, 51 Pegasi b, was detected using this method (Mayor and Queloz, 1995). As shown in figure 1.4 the core
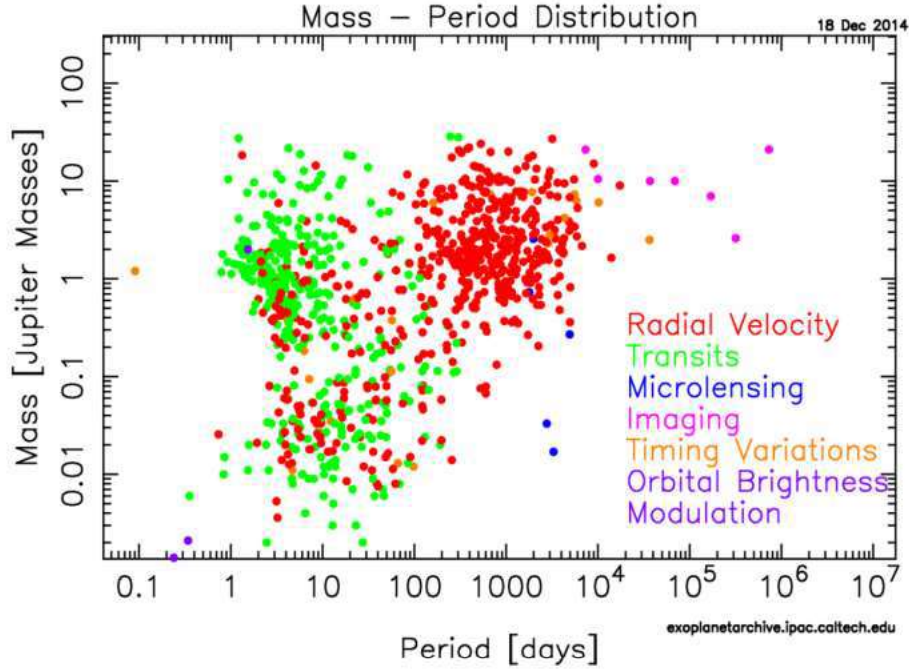
Figure 1.3: Mass period distribution of confirmed exoplanets color-coded by the different techniques used to detect them. Figure taken from Akeson et al., 2013.

principle behind this technique is very simple. In a star-planet system, both the star and planet orbit around the common center of the mass. This 'wobble' in the stellar motion can be detected via Doppler spectroscopy. As the star orbits around the common center of mass, it has a component of motion directed towards the observer. When the star appears to move towards the observer, its spectral lines are blue-shifted to lower wavelengths and when it appears to move away from the observer, its spectral lines are red-shifted to higher wavelengths. Measuring these spectral shifts as the star orbits gives a periodic signature of the orbital velocity along the line of sight. The presence of such a periodic signature suggests the presence of a planet around the star (after accounting for other sources of noise that can cause a similar signature).

Moreover, this technique can be used to estimate the mass of the planet. The radial velocity semiamplitude is defined as

$$K = \frac{v_{max} - v_{min}}{2} \tag{1.1}$$

where v_{max} and v_{min} correspond to the maxima and minima in the periodic velocity curve.
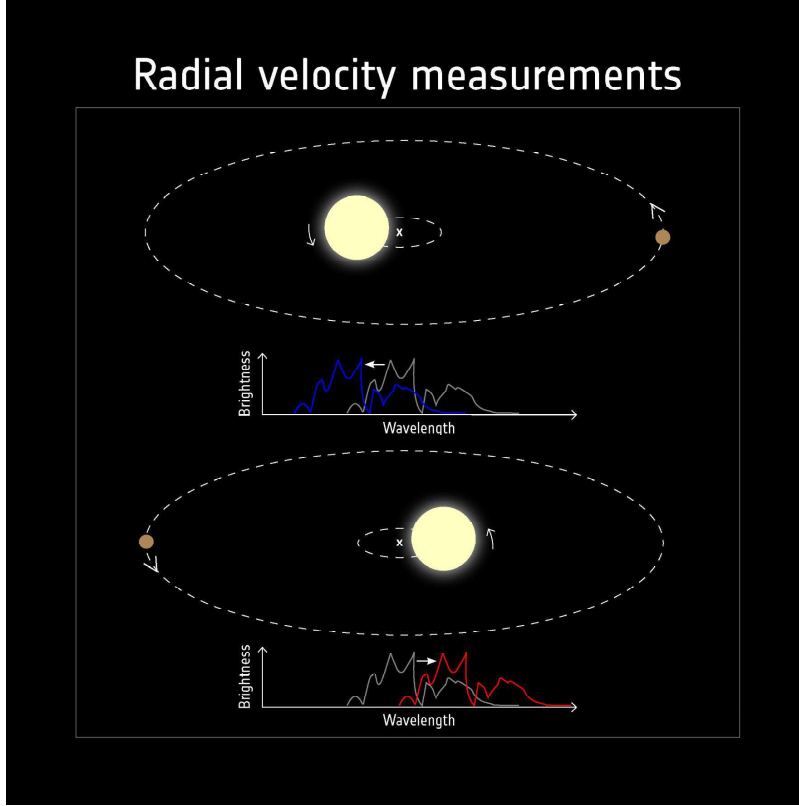
Figure 1.4: The principle behind the radial velocity technique. Credit: *ESA*.

Using Kepler's laws of motion, we can derive an expression for K. In practical units,

$$K = \frac{28.43 \text{ms}^{-1}}{\sqrt{1 - e^2}} \frac{M_p \sin i}{M_{Jup}} \left(\frac{M_p + M_s}{M_\odot} \right)^{-2/3} \left(\frac{P}{1 \text{yr}} \right)^{-1/3} \tag{1.2}$$

where e is the eccentricity of the planet's orbit, M_p and M_s are the planet and stellar masses, P is the orbital period and i is the orbital inclination. K, e, M_s and P can be computed or estimated observationally, and putting in all the values, we get an upper limit on the planet's mass in the form of $M_p \sin i$.

This technique is more sensitive to detecting massive planets around low-mass stars, as they exert a higher gravitational influence on the star which results in a significant stellar wobble. For comparison, the typical semi-amplitude values generated by Jupiter-mass planets around M dwarfs are of the order of 10 m/s which can be detected, while the semi-amplitudes generated by Earth-mass planets are of the order of 1 cm/s which are well beyond the capabilities of our current instruments. Figure 1.3 also confirms this as a majority of the

planets detected by the radial velocity technique have masses which lie between 0.1 M_{Jup} and 10 M_{Jup}.

1.2.2   Transits

A transit is an event where the exoplanet passes in front of its host star as viewed from Earth. An occultation is when the exoplanet goes behind its host star. The number of exoplanets detected by this method has significantly increased since the launch of the Kepler mission in 2009 and the TESS mission in 2018, both of which were dedicated to finding exoplanets by the transit method. As shown in figure 1.5, when the planet passes in front of the star, there is a dip in the star's brightness and this dip can be measured to infer the presence of an exoplanet. This dip is just due to the simple fact that the planet blocks some amount of starlight during the transit.
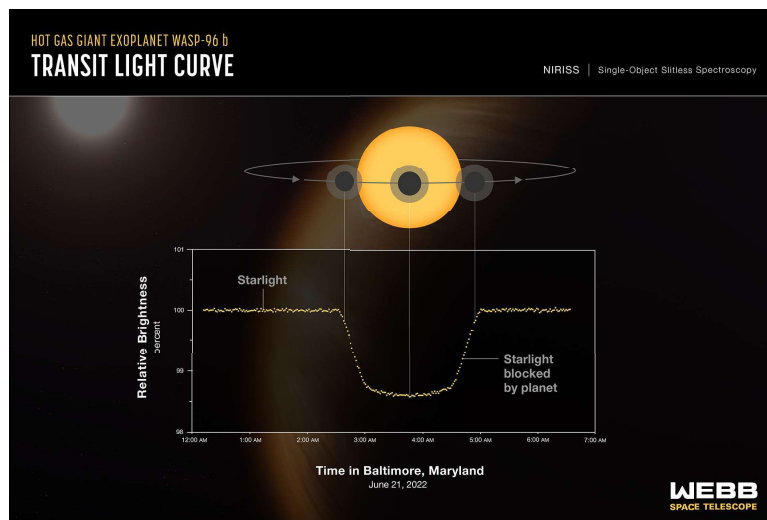
Figure 1.5: A transit light curve, as taken from the JWST's NIRISS instrument of the WASP-96 star system. Credit: *NASA, ESA, CSA, STScI*

A major disadvantage of this method is that transits can only be viewed if the planetary system lies in an edge-on or close to an edge-on orientation with respect to an observer. From geometrical considerations, we can thus calculate the probability that a randomly placed observer can see a transit. For a limiting case when the planet is in a circular orbit (e=0) and is much smaller than the star ($R_p << R_s$), the probability of transit is given by

$$p = \frac{R_s}{a} \tag{1.3}$$

where a is the semi-major axis. This implies that transits of close-in planets with shorter orbital periods are more common and these planets are more likely to be detected by limited observing programs. Thus, the transit method is biased towards detecting planets with short orbital periods. This can also be seen from figure 1.3 where the distribution of the planets detected by transits is skewed towards periods between 1 and 100 days, much smaller than that of Earth. The depth of the light curve, δ, can be approximated as

$$\delta = \left(\frac{R_p}{R_s}\right)^2 \tag{1.4}$$

Thus a measurement of the transit depth yields an estimate of the planetary radius. If the planet has also been characterized by the radial velocity technique which gives an estimate of the mass, we can calculate the average bulk density of the planet, which is useful in classifying a planet as rocky/gaseous.

Observing a short-period planet over multiple orbits gives a periodic signal in the light curve as the planet performs multiple transits. Variations in the timing of this transit can signal the presence of moons or other planets in the system whose gravitational influence slightly changes the orbit of the transiting planet. This method of inferring the presence of other planets is termed the transit timing variation (TTV) technique and has been successfully utilized to detect a few planets.

1.2.3 Microlensing

A microlensing event occurs when a star in the foreground passes close to the line of sight to a more distant star in the background. The foreground star acts as a gravitational lens, magnifying the background source star. If there's a planet orbiting the lens star, it can perturb the light curve and lead to a characteristic short-lived signature from which the planet mass and the star-planet separation can be estimated. A major disadvantage of this method is that a lensing event is a one-time occurrence which will likely never repeat. However, this technique is comparatively more sensitive to detecting Earth-mass planets at relatively large separations.

1.2.4   Direct Imaging

As the name suggests, this technique involves directly imaging a region around a star to detect any planets. However, in many cases, the star is about a billion times brighter than the planets in the system, and simply taking a snapshot will not reveal any planets. Thus, the stellar light has to be blocked, and many coronagraphs have been designed in the past few years for that purpose. Figure 1.6 shows the directly imaged HR 8799 system, where 4 planets are clearly visible in the image upon blocking the star.
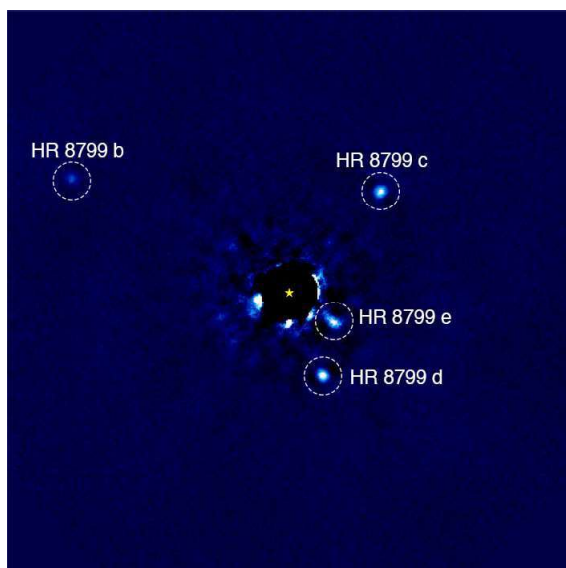
Figure 1.6: The HR 8799 system imaged by the Keck telescope. Upon blocking the stellar light, the 4 planets are clearly visible in the image. Image taken from Marois et al., 2010.

As explained in a later section, the coronagraph blocks light from a finite region around the star, and this region is called the inner working angle (IWA) of the coronagraph. Thus, any close-in planets within this IWA are also blocked out. This technique is comparatively more sensitive to planets at large separations, including Earth-sized planets present in the habitable zone of their host star (R.K. Kopparapu et al., 2013).

The dearth of Earth-sized rocky exoplanet detections still remains a massive observational gap in our current understanding of exoplanets. To fill in this gap, the 2020 Astronomy and Astrophysics decadal survey (National Academies of Sciences and Medicine, 2023) recommended a large ultraviolet/visible/infrared telescope to find and characterize potentially habitable planets around nearby stars. Based on this recommendation, NASA is laying the groundwork for a flagship mission concept, currently referred to as the Habitable Worlds

Observatory (HWO). This mission concept builds on earlier concepts including the Large Ultraviolet Optical Infrared Surveyor (LUVOIR) (LUVOIR Team, 2019) and the Habitable Exoplanets Observatory (HabEx) (Gaudi et al., 2020).

1.3 Exoplanet characterization

The mass, radius, period, distance from the host star and a few other parameters can be estimated using the detection techniques mentioned above. Other properties like density, surface temperature, or metallicity can be calculated from this set of parameters. As shown in figure 1.7, this density can be ingested into theoretical models to infer the internal planetary composition.
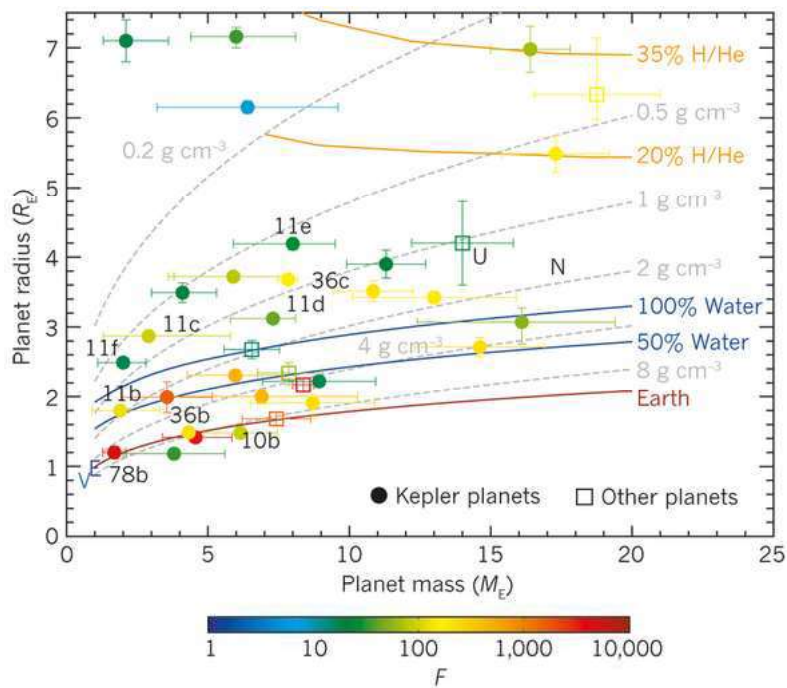
Figure 1.7: Mass-radius plots for transiting exoplanets with the theoretical model curves for each composition. The planets are color-coded by the amount of bolometric flux received as compared to Earth. Figure taken from Lissauer et al., 2014.

However, none of these techniques tell us what the exoplanet's atmosphere is made of or whether it even has an atmosphere. To characterize an exoplanet's atmosphere, we have to resort to spectroscopy. There are two ways in which planetary spectra are measured, (i) transit/transmission spectroscopy and (ii) direct imaging spectroscopy. When a planet transits in front of its host star, light from the star passes through the atmosphere enveloping

the planet where it gets absorbed/scattered by different atmospheric molecules. The size of the planet and subsequently the transit depth is different in different wavelength bands, depending on the amount of light absorbed/scattered in the atmosphere. Thus, during transmission spectroscopy, the transit depth is measured in different wavelength bands, which is used to construct the planet's spectrum. For example, figure 1.8 shows the spectrum of the planet WASP 39b obtained by transmission spectroscopy using JWST's NIRSpec PRISM instrument. The best-fit model to the spectrum is also shown, and absorption bands corresponding to the different atmospheric constituents are labelled.
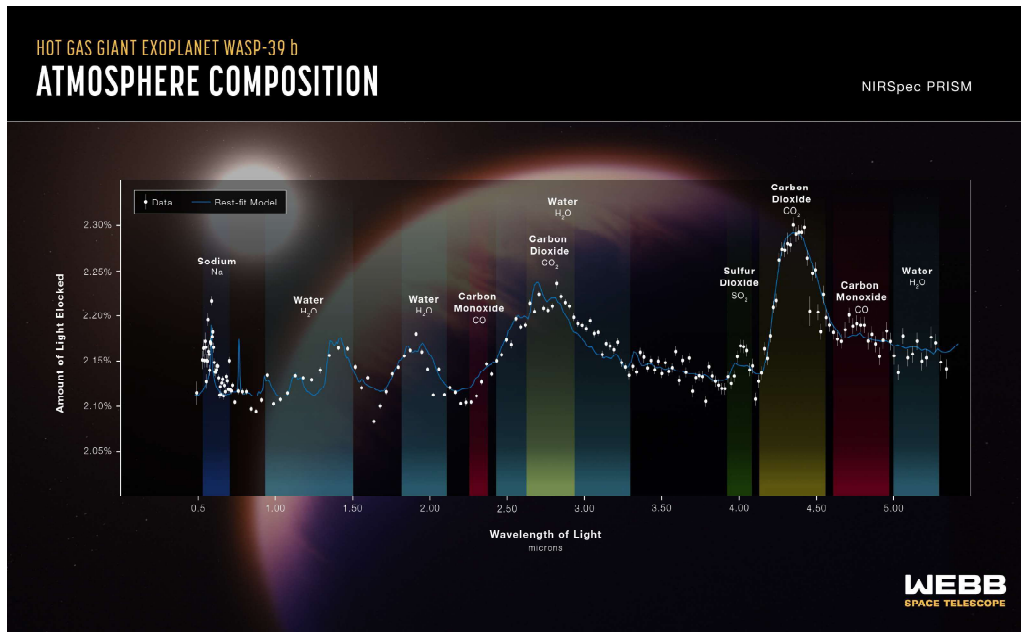
Figure 1.8: Spectrum of the planet WASP 39b obtained by transmission spectroscopy using JWST. Credit: *NASA, ESA, CSA, Joseph Olmsted (STScI)*

In direct imaging spectroscopy, all the light collected from the directly imaged planet is passed through a spectrometer to generate the spectrum of the planet. In addition to finding Earth-like planets in the habitable zone, the main goal of the HWO mission is to characterize their atmospheres using direct imaging spectroscopy.

Spectroscopy is a useful tool to estimate the atmospheric composition of exoplanets, and this analysis is very important in the context of finding habitable or inhabited worlds. Biosignatures are characteristic molecules or features which indicate the presence of life on the planet. These are substances (processes) which cannot be made (which cannot be sustained) in the absence of life. Biosignatures are not to be confused with the molecules/elements which

we know to be essential for life. For example, oxygen on Earth is absolutely essential for the survival of life. In addition to photosynthesis, there are other abiotic sources of oxygen, including photolysis of ozone in the upper atmosphere that produce oxygen. Thus oxygen by itself is not a biosignature because it can be produced via abiotic pathways as well. It is the presence of both oxygen and methane in significant quantities in Earth's atmosphere which indicates the presence of life on Earth, because this implies that the atmosphere is in strong chemical disequilibrium which is only possible if these gases are replenished by biotic pathways. Thus, chemical disequilibrium in a planet's atmopshere may indicate the presence of life (Krissansen-Totton et al., 2016, 2018; A. Young et al., 2023; A.V. Young et al., 2024). However, there are some molecules including organo-sulphur gases like di-methyl sulphide (DMS) which we know are only produced by bacteria, amongst other life forms and there exist no abiotic pathways to produce them. These molecules constitute an important class of biosignatures (Schwieterman et al., 2018; Seager et al., 2013).

1.4 Clouds on Exoplanets

Clouds are ubiquitous on Earth and other solar system planets, and they are likely to be present in the atmospheres of exoplanets as well. A cloud is referred to as any condensate that forms when the vapor pressure of an atmospheric constituent exceeds the saturation vapor pressure. In this way, cloud formation provides a sink for an atmospheric constituent. Earth is dominated by clouds composed mostly of water vapor, however, there is a huge diversity in the composition of clouds on planets in our Solar System. This includes sulphuric acid clouds on Venus (Hansen and Hovenier, 1974), CO_2 ice clouds on Mars (Montmessin et al., 2007), and ammonia clouds on Jupiter (Brooke et al., 1998), to name a few. Given the diversity in the estimated planetary and atmospheric compositions of exoplanets detected so far, we would also expect their atmospheres to host clouds and other aerosols of varied compositions. A haze is referred to as any condensate produced by photochemistry or other non-equilibrium chemical processes, however, the term is used interchangeably with cloud. A general framework of clouds in the atmospheres of Solar system planets is given in Sánchez-Lavega et al., 2004 and a comprehensive summary of clouds and cloud formation in exoplanet atmospheres is given in Gao et al., 2021; Helling, 2019; Marley et al., 2013.

Clouds affect a planet's radiation budget in three important ways - (i) by reflecting shortwave solar radiation back to space, (ii) by absorbing and re-emitting/scattering longwave thermal radiation emitted by the surface, and (iii) also by emitting their own thermal radiation.

Clouds can complicate the radiative transfer processes in an exoplanet's atmosphere and significantly impact the planet's spectrum. Clouds tend to have high albedos, especially in the visible wavelength band, and thus any planet with a cloudy atmosphere will reflect much more light than a cloudless planet, enhancing the continuum in the reflected light spectrum. Clouds improve the detectability of atmospheric constituents in the visible band, especially those present in significant amounts above the cloud layer, by boosting their absorption signals (*Kelkar et.al, in prep*). The effects of clouds on the reflected light spectra were modelled by Cahoy et al., 2010; Marley et al., 1999; Sudarsky et al., 2003 for giant exoplanets and by Kitzmann et al., 2011a for Earth-like exoplanets. Since clouds enhance a planet's albedo, they may impact whether a planet is visible or not via direct imaging. The impact of clouds on this detectability is explored in Kitzmann et al., 2011b; Tinetti et al., 2006a. Clouds are a significant contributor to the greenhouse effect as they absorb and re-emit outgoing longwave radiation emitted by the surface. Thus, the presence of clouds has a profound impact on the thermal emission spectrum of a planet. Due to the greenhouse effect, clouds dampen the spectra features of certain gases in the infrared. The effects of clouds on the thermal emission spectra of planets have been discussed in Hearty et al., 2009; Kitzmann et al., 2011b; Tinetti et al., 2006a; Vasquez et al., 2013. Furthermore, clouds also affect spectral signatures originating from the surface, for example, the vegetation red edge signal characteristic of surface vegetation, as shown in models (Montanes-Rodriguez et al., 2006; Tinetti et al., 2006b) and observations of Earth (Arnold et al., 2002; Hamdani et al., 2006).

In the context of the Habitable Worlds Observatory (HWO) whose main goal is to find and characterize nearby Earth-like exoplanets, an investigation into the impacts of clouds on the characterization of a remote Earth atmosphere stands as an important science pre-cursor. By treating Earth as an exoplanet and conducting a detailed analysis of its spectrum across days with varying cloud coverage provides us with the most accurate quantification of the effects of clouds. This analysis is extremely useful when interpreting spectra of Earth-like exoplanets which might be obtained in the future by space and ground-based missions. Moreover, a quantification of the effect of clouds will address retrieval algorithms and improve their accuracy in determining the atmospheric composition from observed spectra. HWO is scheduled for launch in the late 2030s, and none of the design specifications have been finalized yet. Thus, we also conduct a comparison between all the mission concepts and evaluate their performance in trying to detect important gases for atmospheres with varying cloud coverage. Through this work, we hope to address some of the design and observational strategies for the HWO mission and thus optimize its performance.

Part II

Methods

Chapter 2

Constructing a remote Earth

2.1 Remote Earth characteristics

In this work, Earth is characterized as an exoplanet and is assumed to be situated a few parsecs away, orbiting a Sun-like star in a circular orbit. To construct an accurate model of a remote Earth, we replicate the surface and atmospheric properties of Earth using data from remote sensing satellites. To construct the ground map, we use data from the MODerate resolution Imaging Spectroradiometer (MODIS) (Friedl and Sulla-Menashe, 2015) instrument aboard the Terra and Aqua satellites, which takes high resolution maps of the Earth's surface. Using these maps, we divide the ground coverage into 5 surface types - ocean, snow, grass, soil, and forest. All of these surfaces are modelled to have different wavelength-dependent albedos, as shown in figure 2.2a. To construct the atmosphere, we use the Modern-Era Retrospective analysis for Research and Applications, Version 2 (MERRA-2) (Gelaro et al., 2017) package, which assimilates data collected from different satellites orbiting Earth and produces one comprehensive dataset. Specifically, we make use of the M2I3NVASM component (Global Modeling and Assimilation Office (GMAO), 2015) which is an instantaneous 3-dimensional 3-hourly data collection that consists of assimilations of meteorological parameters at 72 model layers such as temperature, wind components, and mixing ratios of ozone, liquid water, and water-ice clouds. More details about the dataset are given in Appendix A.

Using the MERRA-2 data allows us to accurately replicate the Earth's atmosphere in our remote Earth model. The average temperature profile of the atmosphere is given in figure 2.1a. The atmosphere is composed of N_2, O_2, CO_2, CH_4, N_2O, CO, H_2O and O_3 along with liquid water and water-ice clouds. The vertical abundance profiles of the dominant gases and aerosols are given in figure 2.1b. The aerosol particles are assumed to have a constant size of $5\mu m$ and $100\mu m$ respectively for the liquid and ice clouds.

(a)   (b)
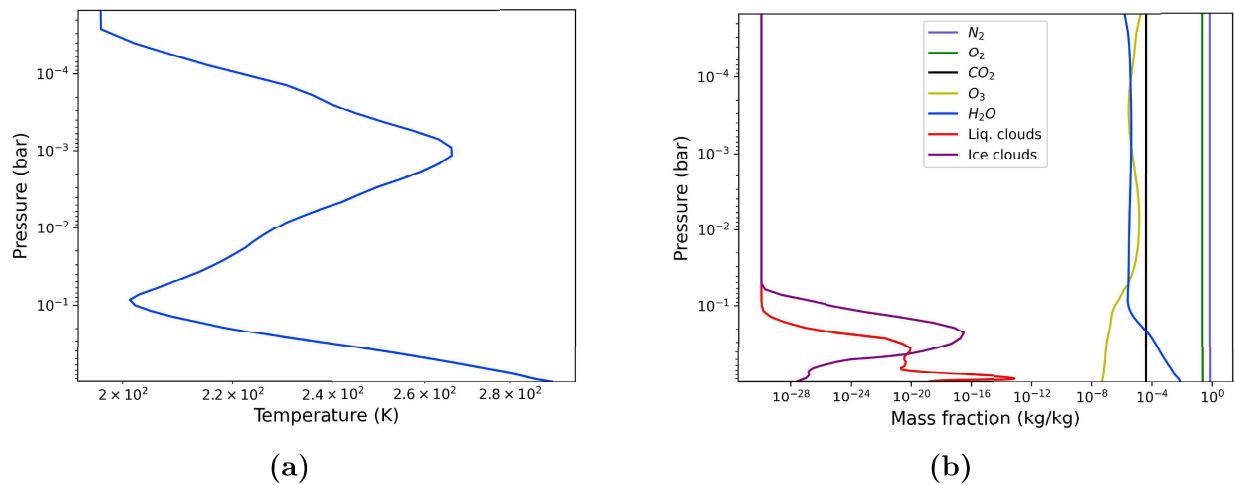
Figure 2.1: (a) The average temperature profile of the atmosphere, (b) The vertical abundance profiles for the dominant gases and aerosols present in the atmosphere. The abundance of each constituent is denoted by its mass fraction in each layer of the atmosphere.

2.1.1   Albedo of the planetary surface

As mentioned before, we divide the ground cover into 5 surface types - ocean, snow, forest, grass, and soil. Each of these surfaces has different wavelength-dependent albedos as shown in figure 2.2a. These albedos have been taken from the USGS spectral library (Kokaly et al., 2017). The net albedo of the surface is just a linear sum of the individual albedo of each surface type weighted by the fraction of area covered by that surface type in the visible disc. It is evident that the ocean has the lowest albedo throughout this wavelength range. Thus, as shown in figure 2.2b, as the planet rotates, the net albedo of the surface decreases as the fraction of ocean cover in the disc increases. Note the significant increase in the albedos of forest and grass at roughly $0.7\mu m$. This is the characteristic vegetation red edge signal which indicates the presence of surface vegetation.
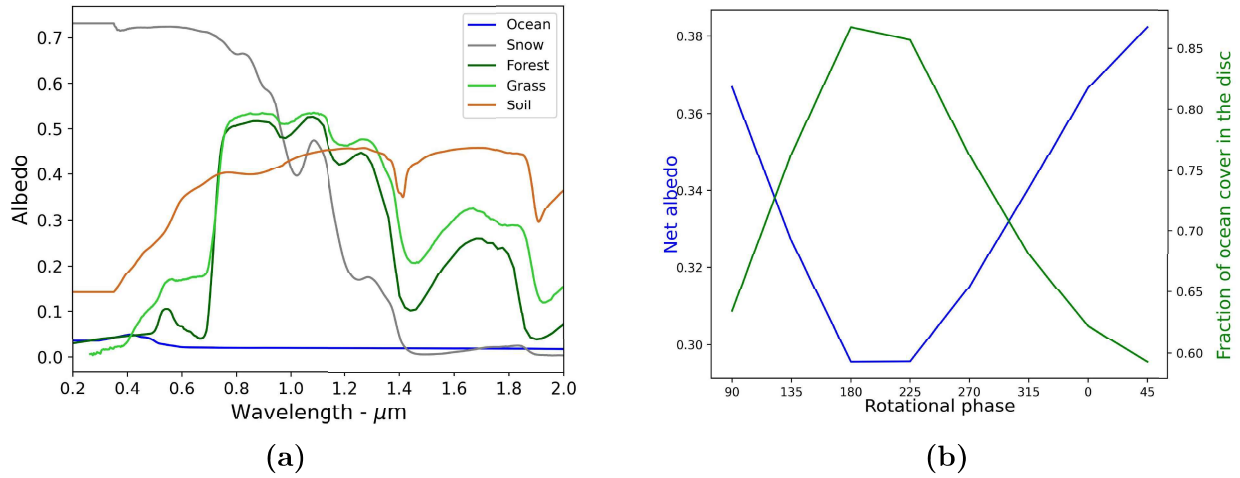
Figure 2.2: (a) Surface albedos for five different surface types - Ocean, Snow, Forest, Grass, and Soil - across the three wavelength bands considered in the spectra. (b) - Evolution of the net albedo of the surface with rotational phase. The net albedo is negatively correlated with the fraction of ocean cover in the disc.

Chapter 3

Planetary Spectrum Generator

The Planetary Spectrum Generator (PSG) is a radiative transfer model suite which combines state-of-the-art radiative transfer codes, spectroscopic and planetary databases to accurately synthesize and retrieve planetary spectra for any given planetary system. It can simulate observations for a broad range of wavelengths from any given observatory or mission concept. We specifically use the GlobES module of PSG which takes in our model for a remote Earth and accurately simulates the spectrum given a range of observational and instrumental parameters. The different aspects of the calculations done will be explained here briefly, but to find out more about using PSG, please refer to the web interface (https://psg.gsfc.nasa.gov), the original paper describing the tool (G.L. Villanueva et al., 2018) or the PSG documentation handbook (G.L. Villanueva et al., 2022). The parameters used to model the observer-star-planet system are divided into three categories - (i) Geometrical parameters, (ii) Atmosphere and surface parameters, and (iii) Instrumental parameters. We'll describe each of these parameters in detail first, and then explain the radiative transfer calculations done by PSG to simulate planetary spectra.

3.1   Geometrical parameters

A spectroscopic simulation requires an accurate description of the geometry of the system and hence it is essential to specify all the parameters related to the geometry. These are divided into two categories - (a) the parameters that describe the properties of the planet and the host star and (b) the parameters that describe the position and orientation of the

observer with respect to the planet-star system. Table 3.1 describes the former and the corresponding values used for each of them in our simulations.

Parameter	Brief description	Value
Object	The type of target (for eg, planet, moon, asteroid)	Planet
Object name	The name of the target	Earth
Diameter	Size of the target	12742 km
Surface gravity	Surface gravity on the object	9.807 m/s^2
Distance to Sun	Distance between the planet and the host star at a given time	1 AU
Velocity to Sun	The RV amplitude for exoplanets[a]	0 km/s
Day length	Apparent rotational period of the target	1 day
Parent star type	The classification type based on spectral characteristics	G-type
Star temperature	The surface temperature of the star	5777 K
Star radius	The size of the star	1 R$_\odot$

Table 3.1: The parameters that describe the properties of the planet and the host star and the corresponding values for each of them. The first column gives the name of the parameter as it is shown on the PSG web interface. [a]The RV amplitude is described in Section 1.2.1.

PSG allows us to set the appropriate observational geometry given a range of parameters. Based on the viewing geometry and distance to the host star, PSG switches between three

geometrical regimes, (i) Orbital and in-situ view, (ii) Observatory view (for planets within 0.1 pc), and (iii) Observatory view (planets beyond 0.1 pc). For the last case, PSG includes the contribution of the host star to the field of view of the instrument. Given an observing geometry, PSG computes the set of incidence and emission angles using a set of sampling algorithms. These angles ultimately inform the radiative transfer codes which compute the amount of light reflected by the planet at each wavelength. More details about the different types of geometries and sampling algorithms to compute the angles can be found in Chapter 2 of the PSG handbook. Table 2 gives a brief description of the parameters which characterize the geometry.

3.2   Atmosphere and surface parameters

PSG allows the user to define any type of atmosphere including the atmospheric constituents and their vertical extent. For atmospheres in hydrostatic equilibrium, a set of parameters like gravity, pressure, and temperature define the vertical structure of the atmosphere. We use the MERRA-2 data to model the atmosphere of our remote Earth, such that the abundance and vertical profiles of all atmospheric gases and aerosols in our remote Earth model match those on Earth. We go through all the parameters that define our atmosphere model, but for more details refer to Chapter 3 of the PSG handbook.

The atmosphere is assumed to be in hydrostatic equilibrium with a surface pressure of 1 bar and a mean molecular weight of 28.97g (similar to that of Earth). The gases present in our atmosphere model are N_2, O_2, CO_2, CH_4, N_2O, CO, H_2O and O_3. N_2 and O_2 are equally distributed throughout the atmosphere with an abundance of 78% and 20.9%. CO_2, CH_4, N_2O and CO are equally distributed with abundances of 400 ppmv, 1.6 ppmv, 1.3 ppmv, and 0.1 ppmv respectively. H_2O and O_3 are not equally distributed and their vertical mixing ratios vary with altitude, as shown in figure 2.1b.

PSG uses correlated k-tables to model the absorption of gases and these are based on the HITRAN/HITEMP database (Gordon et al., 2022; Rothman et al., 2010). These correlated k-opacity tables are precomputed in PSG to make the radiative transfer calculations more efficient. For example, figure 3.1 shows how the line intensity for O_2 varies with wavelength, as taken from the HITRAN database. Apart from line-by-line absorption of gases, PSG allows us to model different atmospheric processes, (i) Rayleigh scattering (the wavelength-dependent elastic scattering of light by particles much smaller than the wavelength of light),

Parameter	Brief description	Value
Sub-solar longitude	Central longitude of the disc facing the host star	*
Sub-solar latitude	Central latitude of the disc facing the host star	0
Season	Orbital phase of the planet in its orbit[a]	*
Viewing geometry	The orientation of the observer w.r.t the planet[b]	Observatory
Disc sub-sampling	No.of distinct regions in the sampling algorithm[c]	1
Beam	FWHM of the instrument's beam or field of view[d]	1 diffraction[e]
Offsets (NS/EW)	Vertical and horizontal offsets w.r.t the observing disc	0,0 arcsec
Sub-observer longitude	Central longitude of the disc facing the observer	*
Sub-observer latitude	Central latitude of the disc facing the observer	0
Relative velocity	Relative velocity between the observer and the target	0 km/s
Distance	Distance between the observer and the surface of the planet	5 pc

Table 3.2: The parameters that describe the observational configuration and the corresponding values for each of them. *These parameters are varied for different simulations. [a]See chapter 8 of this thesis for a description of the orbital phases. [b] See section 6 in Chapter 2 of the PSG handbook for more details about the different types of viewing geometries. [c]Look at figure 5 in chapter 2 of the PSG handbook to see how the disc is sampled. [d]See section 7 in Chapter 2 of the PSG handbook for a description of different beam shapes and calculation of the FWHM. [e]In this case the beam size is defined by the telescope diameter and central wavelength of the bandpass, but it can also be defined in terms of the diameter of the planet.

(ii) Raman scattering (the inelastic scattering of photons by matter) (iii) Refraction of light as it passes through different layers of the atmosphere, (iv) Collision-induced absorption or CIA (Absorption caused by in-elastic collisions between gas molecules which induce quantum transitions) and (v) UV absorption (Absorption of UV photons by molecules which lead to transitions amongst the highly energetic levels). Rayleigh scattering is computed in PSG following the methodology given in Sneep and Ubachs, 2005, while Raman scattering is modelled using the method developed by Pollack et al., 1986 with further adaptations from Oklopčić et al., 2017. PSG uses the refraction indices from https://refractiveindex.info to model refraction in the atmosphere, CIA datasets from HITRAN (Gordon et al., 2022 and references therein) to model CIA and the MPI-Mainz UV/VIS Spectral Atlas (Keller-Rudek et al., 2013) and other UV databases to model UV absorption.
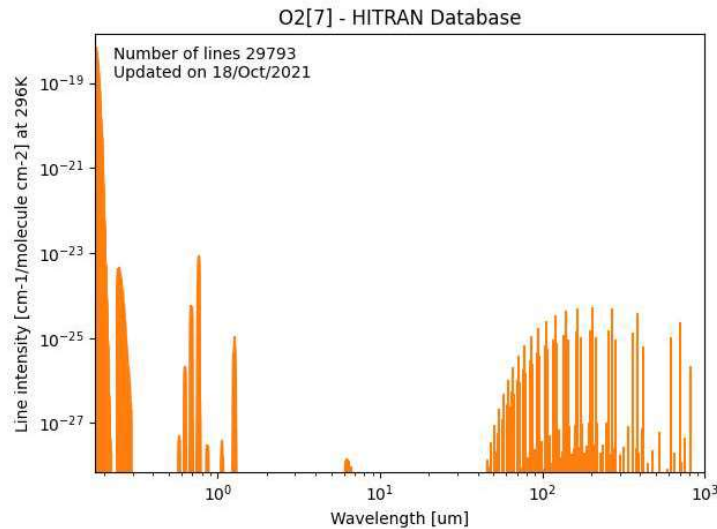
Figure 3.1: Line intensity for O_2 from the HITRAN database (Gordon et al., 2022).

In addition to the gases mentioned above, the atmosphere consists of two scattering aerosols - liquid water clouds and water-ice clouds, whose average vertical abundance profiles are shown in figure 2.1b. The liquid water and water-ice aerosol particles are assumed to have an effective radius of $5\mu m$ and $100\mu m$ respectively. Scattering is an inherently 3D problem which makes it numerically expensive to solve and this problem is further complicated by multiple scattering. PSG keeps track of all the photons as they travel through multiple layers of the atmosphere, which makes the radiative transfer code accurate, but expensive. PSG uses a particular method to solve the integro-differential multiple scattering equation in the

atmosphere. The two parameters that describe this method are given by NMAX and LMAX and they label the number of stream pairs and the number of scattering Legendre polynomials that describe the phase function respectively. This method is briefly described in a later section. PSG provides profiles for three quantities relevant to modelling the Mie scattering by aerosols, (i) the extinction cross-section (in m^2/kg), single scattering albedo (ratio of the amount of light scattered to the total amount of light attenuated), and asymmetry factor (mean cosine of the scattering angle - a measure of the scattering directionality). These profiles are taken from the HITRAN spectroscopic database (Gordon et al., 2017; Massie and Hervig, 2013 and references therein). Figure 3.2 shows these profiles for the liquid water and water-ice aerosols as computed by PSG to perform the scattering calculations.
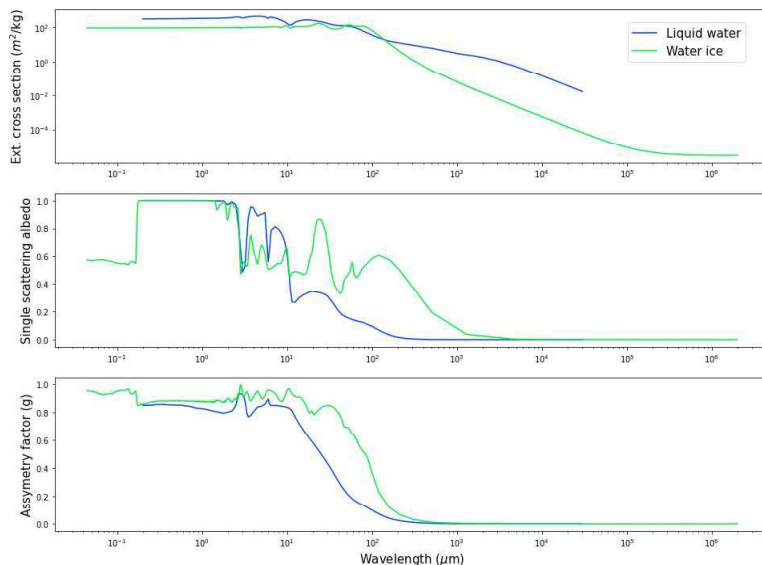
Figure 3.2: The extinction cross-section, single scattering albedo, and asymmetry factor for liquid water (of size 5μm) and water-ice (of size 100μm) aerosol particles as a function of wavelength.

We use high-resolution surface maps of the Earth, as captured by the MODIS observatories, to accurately model the surface of our remote Earth. The landmass and ocean distribution on Earth is replicated in our model. The surface is divided into 5 types - ocean, snow, forest, soil, and grass - each of them having different reflectance properties (for eg. albedo) that vary with wavelength. PSG uses 11 spectral databases (https://psg.gsfc.nasa.gov/helpatm. php#surfaces) to accurately model the reflectances of different surface types across a broad range of wavelengths.

To compute the disk-integrated flux reflected from the surface, PSG uses the parameters given to describe the observing geometry and the direction of incidence and reflected fluxes. Since we compute only the reflected light spectra, we are only concerned with the shortwave fluxes reflected/scattered from the surface, but the same principles apply to longwave fluxes emitted by the surface. To precisely model scattering by the surface, PSG uses three angles to define the geometry, (i) the incidence angle between the source and the normal to the surface, (ii) the reflectance angle between the normal and the detector, and (iii) the phase angle between the source and the detector. These angles, along with the albedo of the surface and other parameters are captured in the bi-directional reflectance distribution function (BRDF) which is a function that describes how light from a source is reflected/scattered by an opaque surface. We assume that the surface is Lambertian, and thus it scatters light isotropically in all directions.

The surface of the planet is not homogenous and is demarcated into the 5 surface types mentioned above, each of them having different optical properties. However, we cannot resolve individual surface types, and we only observe the entire disc of the planet which is an aggregate of the different surface types. Thus we need to employ a mixing model to calculate the effective optical properties of the aggregate. We use the simplest model, the areal linear mixing model which assumes that the entire disc is composed of smaller unresolved patches made up of different surface types and that each patch is homogeneous. Each patch can be treated separately and the properties of the entire disc are simply a linear sum of the individual optical properties of each patch weighted by the corresponding area occupied in the disc. For example, the geometric albedo of the entire disc (at each wavelength) is the sum of geometric albedos of the 5 different surface types weighted by the area occupied by each surface in the disc. Chapter 6 of the PSG handbook gives more details on how different surfaces are modelled in PSG.

3.3 Instrumental parameters

PSG can simulate synthetic spectra for a wide variety of instrumental configurations and wavelength ranges. It has built-in templates for a few instruments and mission concepts, which can be loaded to fix the values of relevant instrumental parameters. To set up our data-to-spectra pipeline, we initially ran all our simulations with the LUVOIR-A mission concept which has a built-in template in PSG. This mission concept is a space observatory that has a 15m big primary mirror with a coronagraph. It is a direct-imaging mission which

will look for planets around nearby stars by imaging these systems in three wavelength bands - UV, visible, and near-infrared. Table 3.3 describes all the relevant instrument and noise parameters for the LUVOIR-A mission concept and brief explanations for a few of them are also provided below. All the parameter values are recommendations taken from the LUVOIR-A mission report (LUVOIR Team, 2019).

Any observation of a planetary system is plagued with background noise and one of these noise sources is the diffuse radiation from the zodiacal plane. This is light scattered by interplanetary dust and refers to the exozodi level in the table 3.3. The value given in the table is scaled relative to the solar system and is taken from Checlair et al., 2021. The mission concept includes a coronagraph which blocks light from the stellar host when observing any planetary system. An ideal coronagraph would block out the star completely, but practical coronagraphs simply reduce the amount of host stellar light by some factor, which is the Contrast given in the table. The lower the contrast value, the better the coronagraph is at reducing stellar noise. In this case, the coronagraph reduces the intensity of stellar light reaching the observer by a factor of 1×10^{-10}. This is perfect for detecting an Earth-like exoplanet because the Earth is about a billion times dimmer than the Sun and reducing the intensity of the Sun by 1×10^{-10} will drastically reduce stellar noise and make it easier to detect the planet. However, there is one significant limitation to using a coronagraph. It blocks out light not just from the stellar host but from a finite area centered around the star. Thus, any planets orbiting very close to the star which are inside this area cannot be detected. The inner working angle (IWA) is the angular separation from the star below which any flux from the system is attenuated. Only planets beyond this IWA and thus planets sufficiently far away from the star are detectable. The IWA is frequently expressed in units of λ/D where λ is a fiducial wavelength and D is the diameter of the mirror. As the mirror size increases, the IWA decreases and the coronagraph becomes more efficient at detecting planets closer to the star. Even beyond the IWA, the coronagraph is not fully efficient and only allows a fraction of light from the planetary system to enter the detector. Figure 3.3a shows the throughput of the coronagraph as a function of the separation from the star. The IWA $= 4\lambda/D$ is labeled and below this separation, the throughput rapidly falls to 0. This coronagraph is far from ideal as even at higher separations, it only allows roughly 27% of the light from the system to enter the detector. In addition to this, the coronagraph also has an optical throughput which is wavelength-dependent, as shown in 3.3b.

Parameter	Value
Diameter	15m
Spectral range	UV: 0.2 - 0.515 μm
	VIS: 0.515 - 1 μm
	NIR: 1 - 2 μm
Resolution	UV: 7 RP
	VIS: 140 RP
	NIR: 70 RP
Exozodi level[a]	4.5
Contrast	1×10^{-10}
Inner working angle (IWA)	4 λ/D
Emissivity of the optics	0.1
Temperature of the optics	270 K
Read noise	UV: 0
	VIS: 0
	NIR: 2.5
Dark noise	UV: 3×10^{-5}
	VIS: 3×10^{-5}
	NIR: 0.002

Table 3.3: The parameters that describe the instrumental configuration for the LUVOIR-A mission concept. [a] Relative to the solar system

Consider our remote Earth orbiting a Sun-like star at a distance of 1 AU in a nearly circular orbit and this system is 5 parsecs away from the observer. At quadrature, the angular separation of the planet and the star is roughly 0.2 arcsec, which corresponds to a separation of 30 λ/D when $\lambda = 0.5\mu$m. Thus the planet is well outside the IWA of the coronagraph. On observing this system through the LUVOIR-A mission concept, the flux from the planet is reduced by a factor of 0.27, and this is the planetary throughput. The flux from the star is reduced by this factor multiplied by the contrast 1×10^{-10}, so the stellar throughput is 2.7×10^{-11}. In addition, both the stellar and planetary flux are scaled by the respective optical throughput at each wavelength.

(a)

(b)
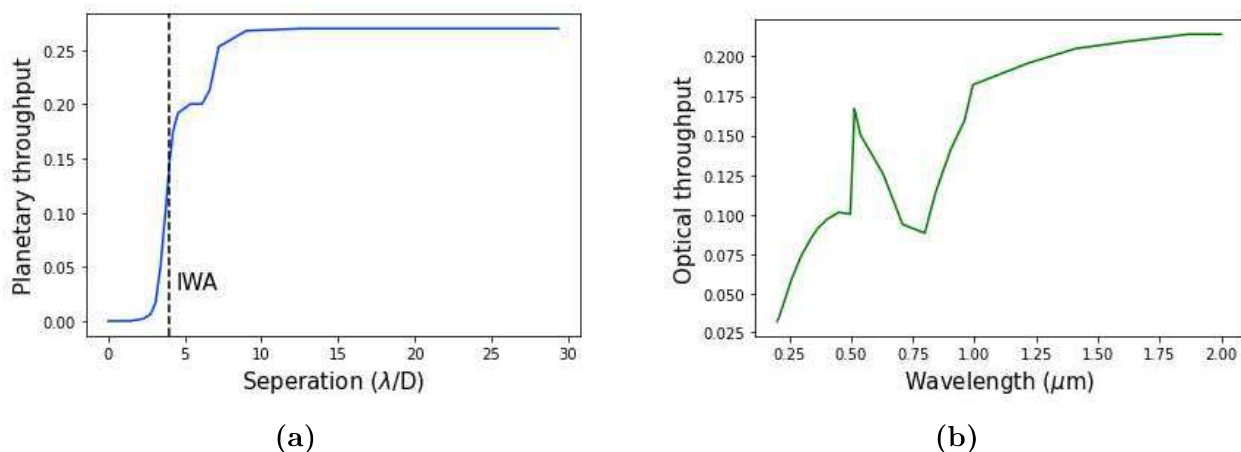
Figure 3.3: (a) Planetary and (b) Optical throughput of the coronagraph for the LUVOIR-A mission concept.

Noise is an integral component of any instrumental configuration and PSG does a precise accounting of all possible sources of noise by keeping track of the instrumental losses and sensitivities. Chapter 8 of the PSG handbook gives a detailed description of the noise simulations performed by PSG but a brief account is given here. The total noise affecting an observation can be divided into three sources, (i) target/scene fluxes (for eg. stellar noise), (ii) background fluxes (zodiacal light or telluric contamination for ground-based telescopes), and (iii) systemic instrument/detector sources. Moreover, the systemic noise from the instrument can be categorized as - (i) optical (collecting area of the instrument, throughput), (ii) thermal (temperature and emissivity of the instrumental optics), (iii) spectral (spectral range and resolution) and (iv) detector (specific noise dependent on the type of detector used). In addition to templates for several instruments, PSG also has different detector models and descriptions of the noise produced by each of them. We assume that our detectors are

charge-coupled devices (CCDs) which work by essentially converting the captured photons into electrons. The charge on each electron is proportional to the intensity of the captured photon and the CCD creates an image by reading these charges. However, some noise creeps in while reading these charges, and thus it is labeled as read noise. Read noise is typically quantified in units of electrons per pixel. The dark noise is an additional source of noise which arises from a background current due to thermally generated electrons within the silicon structure of the CCD. It is expressed in units of number of electrons per second per pixel. Figure 3.4 shows the contribution of different sources to the total noise in the visible band as simulated by PSG from the observational and instrumental parameters as given above.
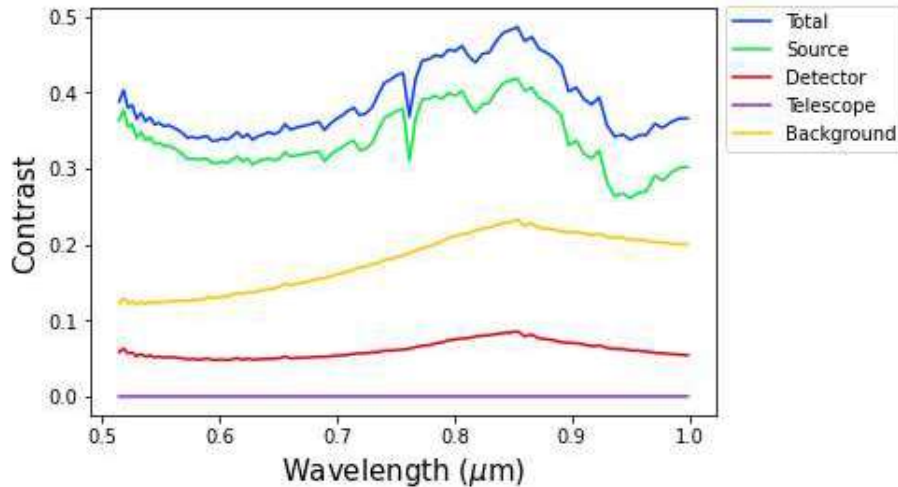
Figure 3.4: The different sources of noise as simulated by PSG.

We select the resolution type as boxcar (as labeled on the web interface) which implies that the separation between simulated spectral points will be as defined by the resolution. The number of pixels is set to 10 and this defines the number of pixels which encompass the beam and the spectral unit. Both of these quantities dictate how the simulated spectrum is projected onto the detector. Furthermore, there are three flags in the instrument section, which indicate whether to include (i) molecular signatures as generated by the radiative transfer model, (ii) continuum signatures from the surface, and (iii) stellar absorption signatures in the reflected light spectra. All three flags are set to 'yes'. Finally, all our initial simulations are run with 3 exposures, each an hour long.

3.4   Radiative transfer and multiple scattering analysis

PSG takes in all the parameters mentioned above to perform radiative transfer calculations and accurately simulates spectra with the given spectral range and resolution. To do so, it utilizes the Planetary and Universal Model of Atmospheric Scattering (PUMAS) which integrates radiative transfer codes and spectroscopic parameterizations to compute spectra via line-by-line calculations (Edwards, 1992; G. Villanueva et al., 2015; Wolff et al., 2009). Our 3d remote Earth model is ingested into the GlobES module of PSG where the 3d atmospheric data is mapped onto a 2d observational grid which is fed to the radiative transfer code. One important point to note here is that our remote Earth model, constructed from the MERRA-2 data has a spatial resolution of 0.625° longitude × 0.5° latitude, however GlobES supports a much lower spatial resolution of 2.5° longitude ×2° latitude, so the MERRA-2 data is first binned to match this resolution. After uploading this data to GlobES, PSG allows the user to further bin the data to even lower resolutions to speed up the radiative transfer calculations. Once these bins are specified, the whole disc is sampled according to these bins. PSG performs the radiative transfer calculations across the whole observable disc and the disc-integrated spectrum is thus calculated as the linear sum of individual spectra weighted by the projected area of each bin.

To perform the radiative transfer calculations, PSG tracks each photon from the source along its path to the observer. Along this path, the incident photons may get absorbed by different molecules in the atmosphere, as well as scattered by aerosol and dust particles. Moreover, new photons are generated via thermal emission from the planet's surface and the atmosphere. Chapters 4 and 5 of the PSG handbook provide a detailed description of how these radiative transfer calculations are done for different types of atmospheres, but a brief description will be provided here. In general, the radiative transfer equation can be written as

$$\mu \frac{\mathrm{dI}(\tau, \mu, \phi)}{\mathrm{d}\tau} = \mathrm{I}(\tau, \mu, \phi) - \mathrm{J}(\tau, \mu, \phi) \tag{3.1}$$

where I is the intensity of light, τ is the optical depth (proxy to altitude), μ is the cosine of the zenith angle, ϕ is the azimuth angle and J is the source function, which can be expressed as

$$\mathrm{J}(\tau, \mu, \phi) = \frac{\mathrm{w}}{4\pi} \int_0^{2\pi} \int_{-1}^{1} \mathrm{I}(\tau, \mu', \phi')\mathrm{P}(\mu, \phi, \mu', \phi') \, \mathrm{d}\mu' \, \mathrm{d}\phi' + \frac{\mathrm{w}}{4\pi} \mathrm{F_s}\mathrm{P}(\mu, \phi, -\mu_0, \phi_0)e^{\frac{-\tau}{\mu_0}} + (1-\mathrm{w})\mathrm{S}(\tau) \tag{3.2}$$

The first term is the multiple scattering term, the second term is the single scattering contribution to the solar diffuse radiation and the last term is the thermal source component. w corresponds to the scattering albedo, F_s is the incident solar flux at the top of the atmosphere, $P(\mu, \phi, \mu', \phi')$ is the phase function at incidence (μ', ϕ') and emission (μ, ϕ) and (μ_0, ϕ_0) are the solar zenith and azimuth angles (with the negative sign for incoming fluxes). In local thermal equilibrium (LTE), $S(\tau) = B(\tau)$ where B is the Planck function. Integrating eq. 4.1 gives

$$I(\tau, \mu, \phi) = I(\tau_0, \mu, \phi)e^{\frac{-(\tau-\tau_0)}{\mu}} + \int_{\tau_0}^{\tau} J(\tau', \mu, \phi)e^{\frac{-(\tau-\tau')}{\mu}} \frac{d\tau'}{\mu} \tag{3.3}$$

In the case of no scattering and LTE, eq. 3.3 reduces to the Schwarzschild equation of radiative transfer. The radiative transfer code in PSG integrates eq. 3.3 numerically along the path of radiation.

The complete radiative transfer calculation can be divided into two parts - from the top of the atmosphere to the surface and from the surface to the observer. Assuming only single scattering, an observer on the surface calculates the downward flux reaching the surface as

$$I^{\downarrow}(\tau_s, \mu, \phi) = \int_0^{\tau_s} J(\tau', -\mu, \phi)e^{\frac{-(\tau_s-\tau')}{\mu}} \frac{d\tau'}{\mu} \tag{3.4}$$

where J includes only the single scattering and the thermal emission term. Similarly, an observer at the top of the atmosphere calculates the upward flux from the surface as

$$I^{\uparrow}(0, \mu, \phi) = I_s(\tau_s, \mu, \phi)e^{\frac{-\tau_s}{\mu}} + \int_0^{\tau_s} J(\tau', \mu, \phi)e^{\frac{-\tau'}{\mu}} \frac{d\tau'}{\mu} \tag{3.5}$$

However, eq. 3.5 is complicated by the fact that the surface is not just emitting thermal radiation, but also reflecting the incident radiance arriving from all possible directions. Thus, I_s includes a thermal component and a reflected radiance component.

This single scattering approximation is only valid for a highly absorbing medium or an optically thin atmosphere but in the majority of other cases where aerosols are the dominant scattering source, the complete radiative transfer equation which involves the multiple scattering term needs to be solved. For this purpose, PSG uses the DISORT package which was specifically developed to efficiently solve the multiple scattering problem (Buras et al., 2011; Stamnes et al., 1988, 2000). Chapter 5 of the PSG handbook gives a comprehensive description of the method used to solve the multiple scattering problem and all the relevant

equations. However, in brief, the core idea of the method is to discretize the azimuthal and zenith angles. Firstly, the ϕ-dependence in eq. 3.3 can be factored out by assuming that the phase function depends only on the angle between the incident and scattered beams, which allows us to write the intensity as a linear combination of Fourier terms.

$$I(\tau, \mu, \phi) = \sum_{m=0}^{2M-1} I^m(\tau, \mu) \cos m(\phi_0 - \phi) \tag{3.6}$$

where 2M is the number of azimuth components. The phase function can be similarly expanded as a series of Legendre polynomials. The zenith angles are discretized by employing the Gaussian quadrature angles (Wiscombe, 1977), and the discretized radiative transfer equation takes the form

$$\mu_i \frac{dI^m(\tau, \mu_i)}{d\tau} = I^m(\tau, \mu_i) - J^m(\tau, \mu_i) \quad m = 0, 1, ...2M-1 \quad i = \pm 1, ... \pm N \tag{3.7}$$

where μ_i is called a 'stream' and this solution is referred to as a 2-N stream solution. Conventionally the number of discretizations of the azimuth and the zenith angles is kept the same, thus, 2M=2N. Now, N is labeled as NMAX in PSG, and it describes the number of stream pairs in the solution. By employing the IMS method (Nakajima and Tanaka, 1988), the number of Legendre polynomials can be expanded beyond 2M up to the desired LMAX number of terms. In our simulations, NMAX and LMAX are set to 1 and 66 respectively.

Part III

Results

Chapter 4

Characterizing the remote Earth spectrum

As mentioned before, our remote Earth is assumed to orbit a Sun-like star in a nearly circular orbit at a distance of 5 parsecs from the observer. The planet's orbit is oriented in an edge-on view such that the observer sees the planet moving across a straight line in the sky. For simplicity, the obliquity of the planet's rotational axis is assumed to be 0°. Initially, the planet is placed at quadrature (see section 8.1), so that it can be observed at its maximum angular separation from the host star, well outside the inner working angle of the coronagraph. To set up our pipeline, we simulate observations with the LUVOIR-A mission concept which is a space observatory concept with a 15 m primary mirror, but we eventually switch to doing simulations with mission concepts with more practical mirror sizes like LUVOIR-B (8m), HWO (6m) and Habex (4m). Initially, each observation is simulated with an exposure time of 3 hours.

Figure 4.1 shows the reflected light spectrum of our remote Earth as simulated by PSG with the LUVOIR-A mission concept. The x-axis is divided into 3 wavelength bands - UV, visible, and near-infrared and these bands are based on the current specifications of the instrument. The y-axis depicts the contrast which is the ratio of the flux from the planet to the stellar flux. These values are scaled by the 'Contrast' value of the coronagraph, 1×10^{-10}. O_3, O_2 and H_2O are the only gases which show dominant absorption in the given spectral range, and their absorption bands are labeled correspondingly. The steady decrease in the continuum from $0.3\mu m$ to $0.6\mu m$ is attributed to Rayleigh scattering by different molecules in the atmosphere.
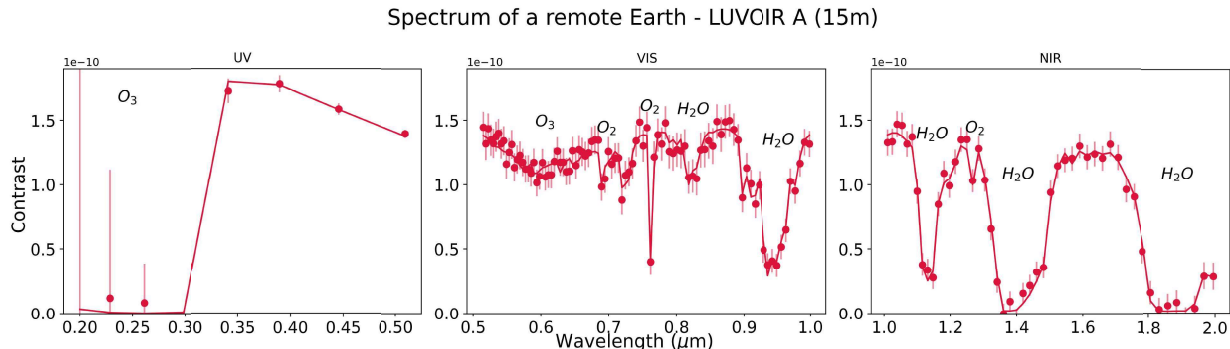
Figure 4.1: Spectrum of a remote Earth in three wavelength bands - UV, visible, and near-infrared as simulated by PSG using the LUVOIR-A mission concept.

In the plot above, the solid line corresponds to a theoretical model spectrum, while the dots and the scatter correspond to this model spectrum convolved with simulated noise from the instrument and binned into the defined spectral resolution. Thus, the solid line corresponds to what the spectrum should look like theoretically while the dots can be interpreted as a real observation which includes noise and scatter. PSG simulates different types of noises, as described in Section 2.2.3, and calculates the total noise by adding up all of them. The contrast values corresponding to the dots C_o are computed as

$$C_o = C_t + rN \tag{4.1}$$

where C_t are the theoretical spectrum values, r is a random number uniformly generated between (-1,1) and N is the noise simulated by PSG. This calculation is done at each wavelength bin. The scatter in the values corresponds to 1σ error bars.

As this planet rotates, different portions of the planet's illuminated disc come into view. As shown in figure 4.2, each portion is labeled by a corresponding rotational phase, which is just the central longitude of the disc facing the observer. We simulate observations of this rotating planet with an exposure time of 3 hrs to match the temporal resolution of the MERRA-2 data. Thus, after each simulation of an observation, we update our remote Earth model with data from MERRA-2 to accurately model the evolution of the atmosphere and its constituent gases and aerosols due to short-term weather patterns. Since there are 8 datasets corresponding to one day, we simulate 8 observations of a planet as it makes one full rotation, with each observation having an exposure period of 3 hours.
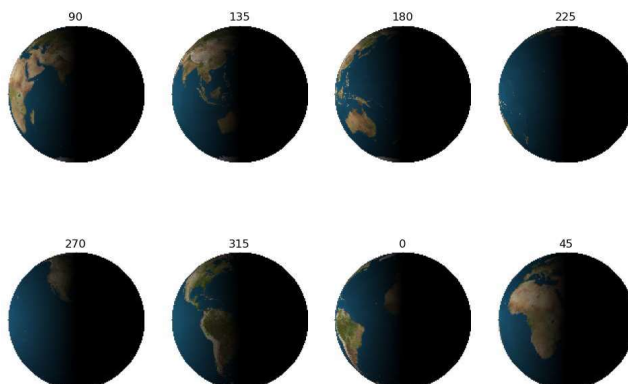
Figure 4.2: The rotational phase which labels each observation of the planet and the corresponding portion of the disc facing the observer. Note that since the planet is located at quadrature, only half of the disk is illuminated.

Figure 4.3 shows the simulated reflectance spectra of a rotating remote Earth. The spectra are color-coded by the rotational phase which labels the corresponding portion of the disc facing the observer. The dots and the scatter have been removed for the sake of clarity and only the theoretical model spectra are plotted. However figure B.2 in Appendix B shows that even when the scatter is included, there is still some disparity which implies that this variation in the spectrum as the planet rotates might be detected, given there are no additional sources of noise. This variation in the spectrum can be attributed to two factors - (i) Net albedo of the illuminated surface which changes with the rotational phase and (ii) the distribution of clouds in the atmosphere over different portions of the disc. An animation of the plot below which shows how the planet's spectrum varies as it rotates is shown here.
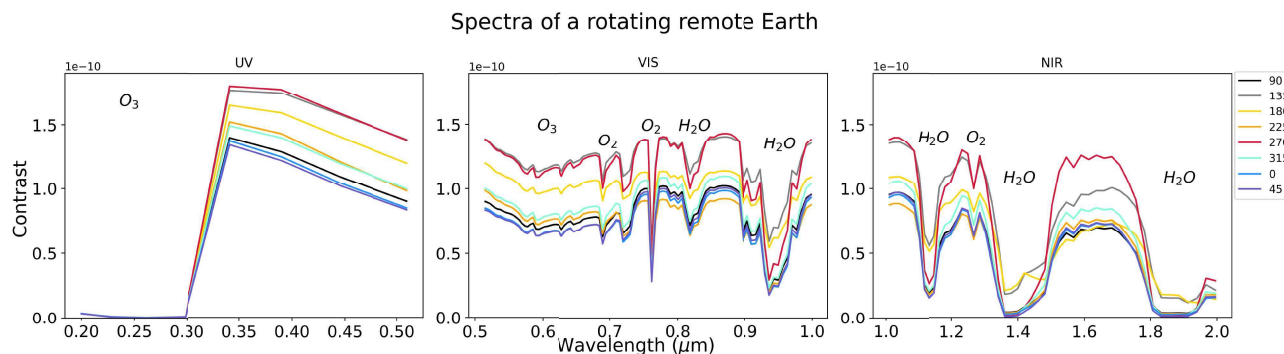
Figure 4.3: Reflectance spectra of the rotating remote Earth simulated using the LUVOIR-A mission concept. The spectra are color-coded by rotational phase which labels different portions of the disc facing the observer. Different absorption bands corresponding to O_3, O_2 and H_2O are also labeled.

Chapter 5

Impact of clouds on the remote Earth spectrum

Before we analyze the impact of clouds, consider two configurations A and B corresponding to rotational phases 270 and 45 respectively. For the sake of clarity, instead of looking at all eight configurations, we'll restrict our analysis to these two cases and present our results accordingly. To start with, figure 5.1 compares the spectra for these two cases, and it is evident that there is a significant difference between the two, and they are well outside each other's error bars.
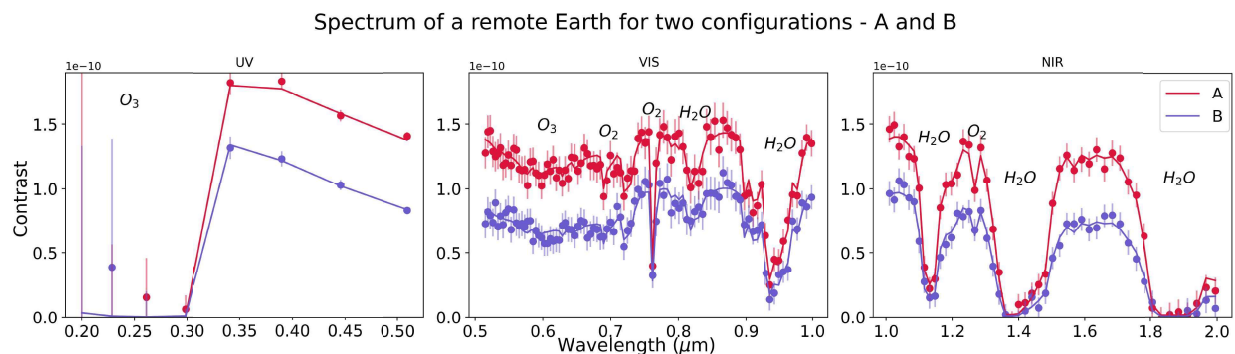
Figure 5.1: Spectra of the remote Earth for the two configurations A and B.

Now consider our remote Earth model with a clear atmosphere devoid of any clouds. Figure 5.2 compares the spectra of cases A and B for such a clear atmosphere. The continuum is shifted to much lower values for both cases, since the surface has a lower albedo than the

clouds, and removing the clouds reduces the net albedo of the disc and subsequently reduces the amount of light reflected by the disc. Figure B.3 in Appendix B shows the spectra for all eight rotational configurations. Note that the continuum of the spectra flips in the absence of clouds and this can be attributed to the interplay between the net albedo of the surface and the distribution of clouds in the atmosphere.
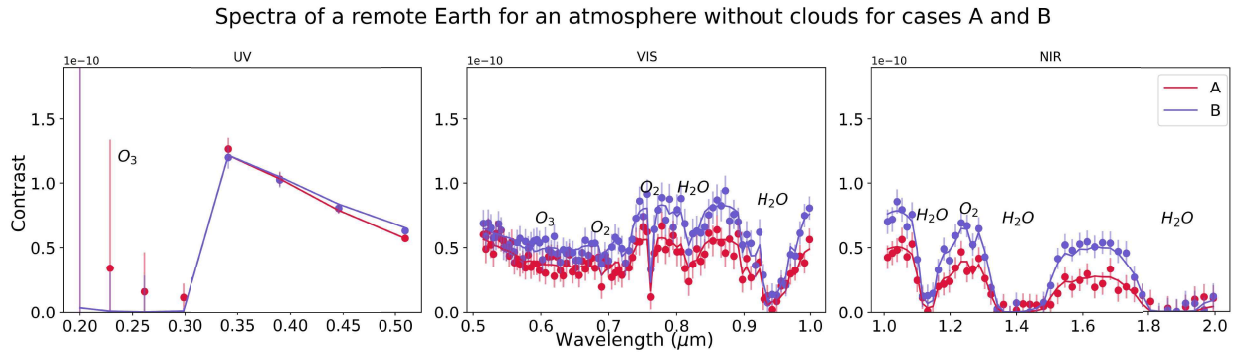
Figure 5.2: Reflectance spectra of the remote earth with a clear atmosphere devoid of any clouds for the two cases A and B.

Figure 5.3 shows the simulated reflectance spectra of a bare exo-Earth without an atmosphere. In the absence of an atmosphere, the differences in the spectra are only due to the different net albedos of the surface. It is evident that in the absence of clouds, disc B has a higher surface albedo than disc A, which also explains why disc B has a higher continuum in figure 5.2. As described in section **no.**, this higher albedo value can be attributed to a higher fraction of landmass cover in disc B as compared to disc A. Figure B.4 in Appendix B depicts the spectra of the bare remote Earth for all eight configurations.
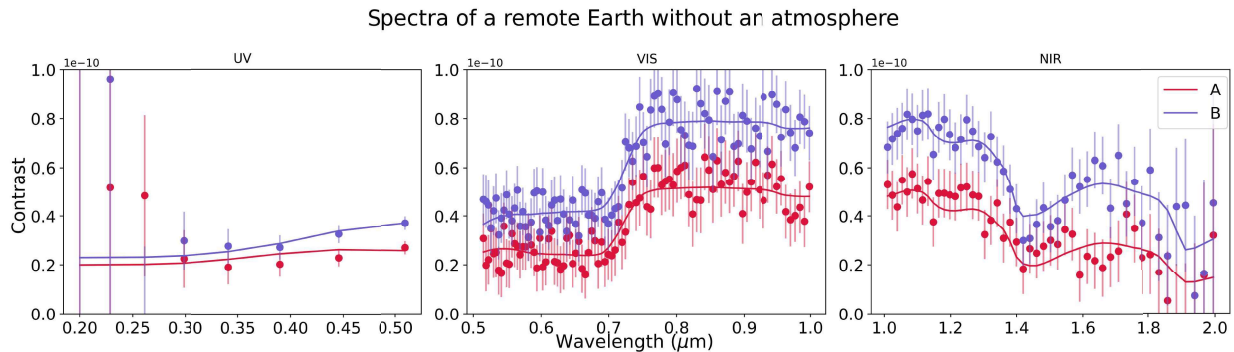
Figure 5.3: Reflectance spectra of a bare remote Earth without an atmosphere for the two cases A and B.

It seems that the presence of clouds has a dramatic effect on the albedo of disc A, significantly increasing the continuum in the reflected light spectrum. Figure 5.4 shows the cloud coverage over the two discs A and B, as derived from the The International Satellite Cloud Climatology Project (ISCCP) data (A.H. Young et al., 2018). The lighter colors represent higher cloud coverage and it is pretty evident that disc A has significantly more cloud coverage than disc B, especially all those white spots over the Pacific Ocean. These clouds are a dominant contributor to the net albedo of the disc and thus increase the reflectivity of the disc, resulting in a higher continuum as seen in figure 5.1.
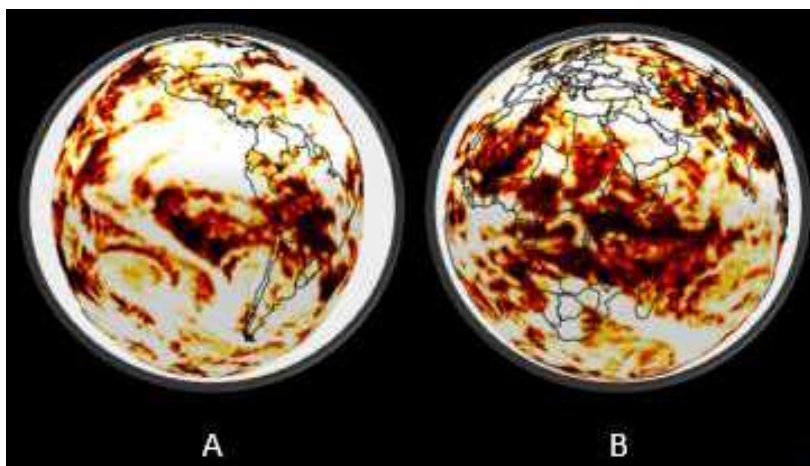
Figure 5.4: Cloud cover over discs A and B as derived using the ISCCP dataset. The lighter colors represent more cloud coverage.

Now just as an interesting exercise, we can further isolate the dominating effect of clouds by considering our remote Earth atmosphere to be composed only of clouds but no gases. Figure 5.5 shows the reflectance spectra of such a planet for discs A and B. Figure B.5 in Appendix B shows a similar comparison for all the eight configurations. An analysis of figures 5.3 and 5.5 helps in quantifying the corresponding effects of the surface and the clouds on the spectrum and explains why the effects of clouds are dominant.
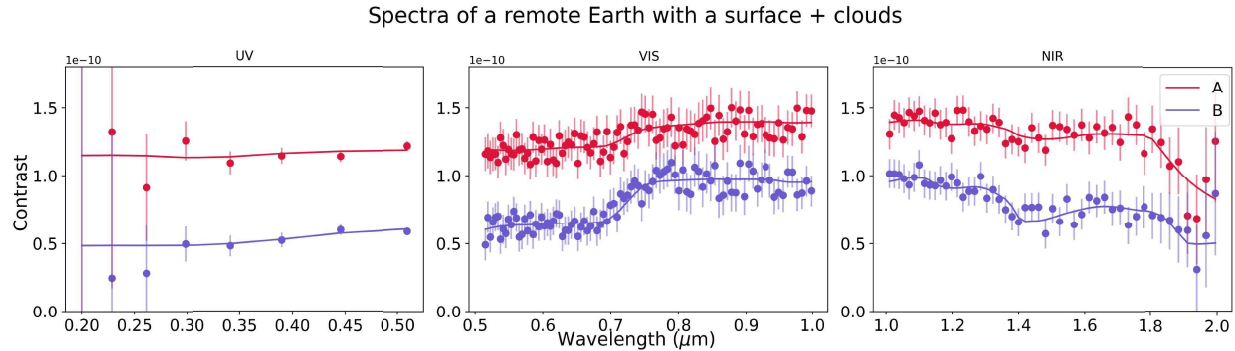
Figure 5.5: Reflectance spectra for a remote Earth atmosphere only made up of clouds and no gases.

Finally, the dominant effect of clouds can also be assessed by looking at the contrast value at one particular wavelength and how it varies with the rotational phase. Figure 5.6a shows that the evolution of the contrast value at 1.6μm with rotational phase roughly matches the evolution of the net albedo (see figure 2.2b) and is anticorrelated to the fraction of ocean cover in the disc. On the other hand, for a cloudy atmosphere, the evolution of the contrast value has no correlation with the surface albedo (see figure 5.6b) and it depends on the amount of cloud cover over the corresponding disc.
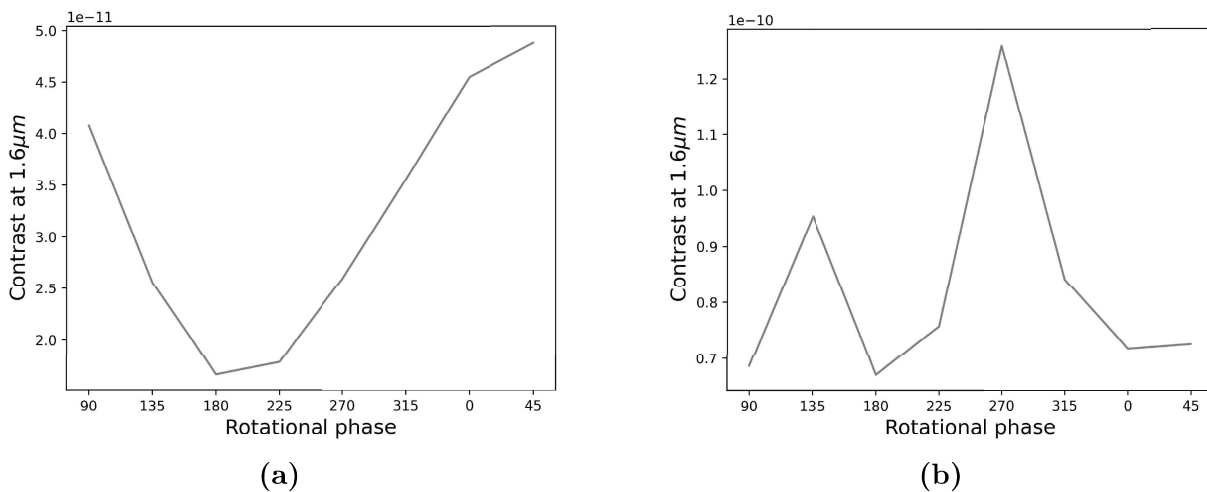
Figure 5.6: Evolution of the contrast value at 1.6μm with rotational phase for a (a) clear atmosphere and a (b) cloudy atmosphere.

Chapter 6

Computing Signal-to-Noise Ratios

The detectability of any gas in the exoplanet's atmosphere is quantified by its Signal-to-Noise Ratio (SNR). As is common throughout physics, an SNR of 5 is considered a gold standard to confirm the detection of any gas. Consider the spectrum of disc A plotted in red as shown previously and the spectrum for the same disc A but with an atmosphere devoid of O_2 plotted in gold, as shown in figure 6.1. Both the spectra match pretty well except in the regions of O_2 absorption in the visible and nir bands and the region of Rayleigh scattering in the uv band. Oxygen's most prominent absorption line at 0.76μm in the visible band is labeled by the arrow, and there is a massive dip in the red curve at that wavelength.
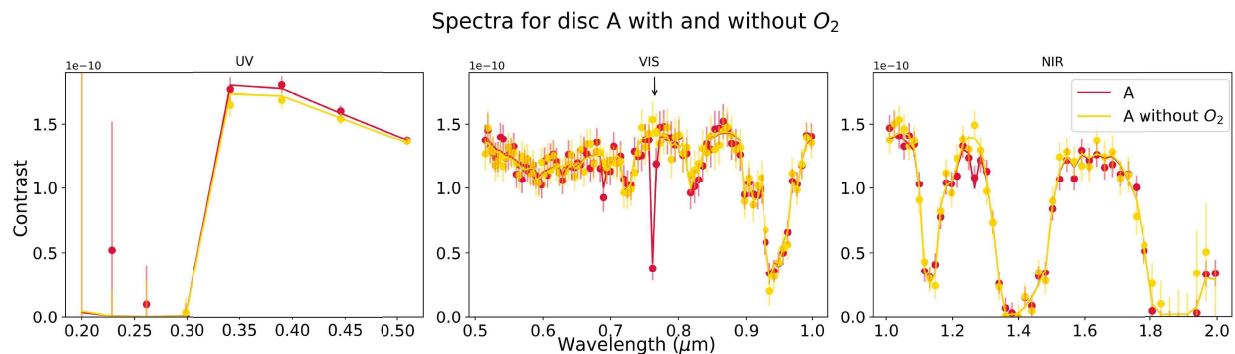
Figure 6.1: Spectrum of disc A for a default atmosphere and an atmosphere without O_2. Oxygen's most prominent absorption line at 0.76μm in the visible band is labeled by the arrow.

The Signal at each wavelength S_i is calculated as

$$S_i = C_O - C_d \tag{6.1}$$

where C_O is the contrast for an atmosphere without O_2, as shown in gold and C_d is the contrast for a default atmosphere, as shown in red. Taking a difference of the two will give spikes at the regions where O_2 shows high absorption. Diving this signal by the noise simulated by PSG gives the Signal-to-Noise Ratio (SNR) at each wavelength. The net SNR across a wavelength band is then computed as

$$\text{net SNR} = \sqrt{\sum_i (\text{SNR})_i^2} \tag{6.2}$$

This procedure to calculate the SNR is well established in literature (Checlair et al., 2021; R. Kopparapu et al., 2021; Lustig-Yaeger et al., 2019). This computation is shown using O_2 but the same principles apply to other gases. Note that the signal is calculated using the theoretical model spectrum shown by the solid lines. The scatter points emulate a real observation and we cannot do this exercise of subtracting a gas from the model to calculate SNRs for a real observation. This issue is discussed further in a later section.

Chapter 7

Impact of clouds on the detectability of atmospheric gases

7.1 Detectability of O_2

As mentioned above, to calculate the SNR values for O_2, we construct a model atmosphere without O_2 and simulate the resulting spectrum. Figure 7.1 shows the simulated reflectance spectra for a cloudy and a clear atmosphere without O_2 for the two cases A and B. The most prominent spectral feature of O_2, its absorption at 0.76 μm is missing in both spectra due to the absence of O_2 in the atmosphere.

Figure 7.2 depicts the SNR values for O_2 in the visible band for a cloudy and clear atmosphere for the two discs A and B. The plot is centered around 0.76 μm, where O_2 shows the highest absorption. Disc A has more cloud coverage, a higher albedo and a higher continuum in the reflected light spectrum. These factors boost the signal for O_2 and thus disc A has a higher SNR than disc B. In the absence of clouds, disc B has a higher net surface albedo which leads to a higher SNR. Comparing the two plots, its evident that clouds boost the SNR for O_2 and thus improve its detectability in the visible band. The inset plots show how the net SNR as well as the SNR at 0.76μm evolves with rotational phase for a cloudy and a clear atmosphere.

Spectra of a remote Earth for a cloudy atmosphere without O_2

(a)

Spectra of a remote Earth for a clear atmosphere without O_2

(b)
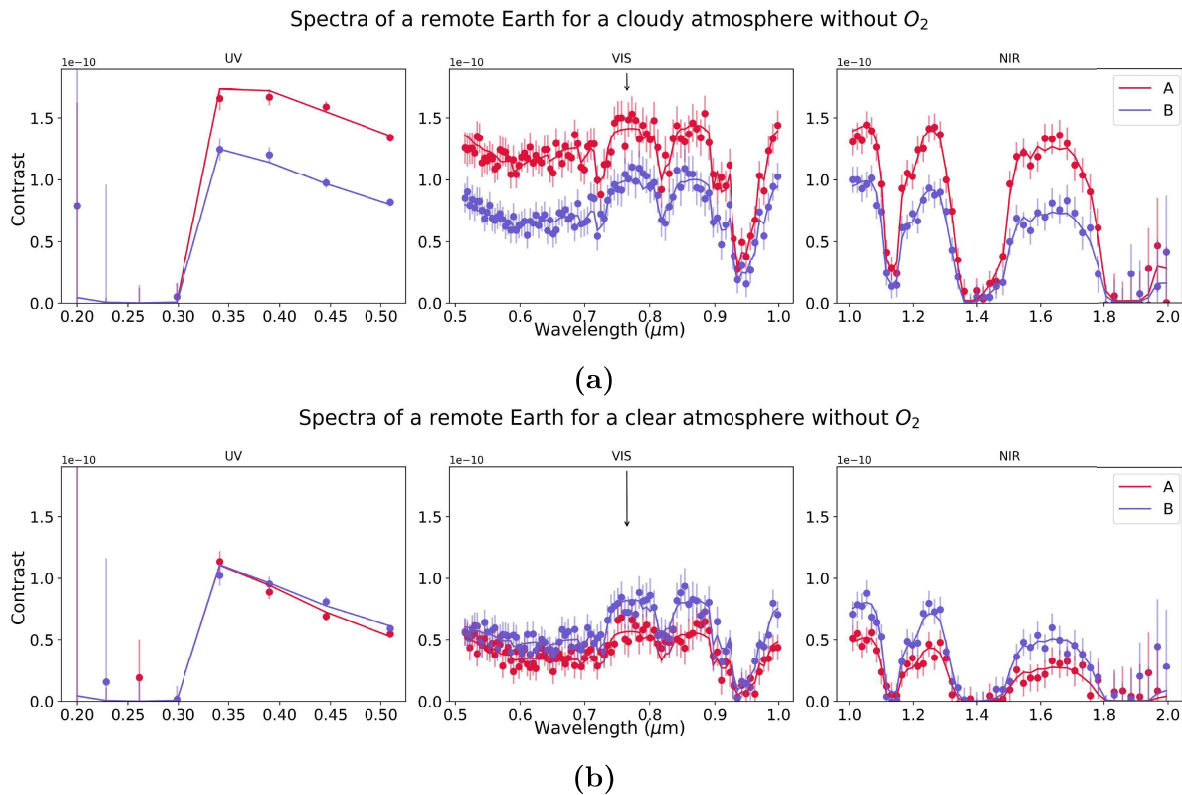
Figure 7.1: Reflectance spectra for a (a) cloudy atmosphere and (b) clear atmosphere without O_2 for the two cases A and B. The arrow depicts the missing O_2 absorption line at 0.76μm in the visible band.

In the absence of clouds, the SNRs seem to follow the trend of the net albedo of the surface (see figure 2.2b), while in the presence of clouds, there is no correlation between the SNR and the net albedo of the surface, as in this case, the distribution of clouds is the dominating factor affecting the albedo of the planet and subsequently the SNRs.

However, these results only make sense if there is sufficient oxygen present above the cloud layer. Due to the high albedo of the clouds, it is difficult to probe the atmosphere below the cloud layer, and if a large amount of gas is present below the cloud layer, the presence of clouds will in fact reduce the detectability of that particular gas. Thus, to explain the results obtained above, we digress a bit here to compute theoretical estimates of the SNR to get an intuitive understanding of how clouds affect the SNR. In the following sections, we (i) calculate the mass of O_2 in an atmospheric column to get a sense of how much O_2 is present above the cloud layer, (ii) compute the SNRs for a cloudy and a clear atmosphere using a simple radiative transfer model. Finally, we use the results from both of these sections to try

to explain the effect of clouds on SNRs of O_2.
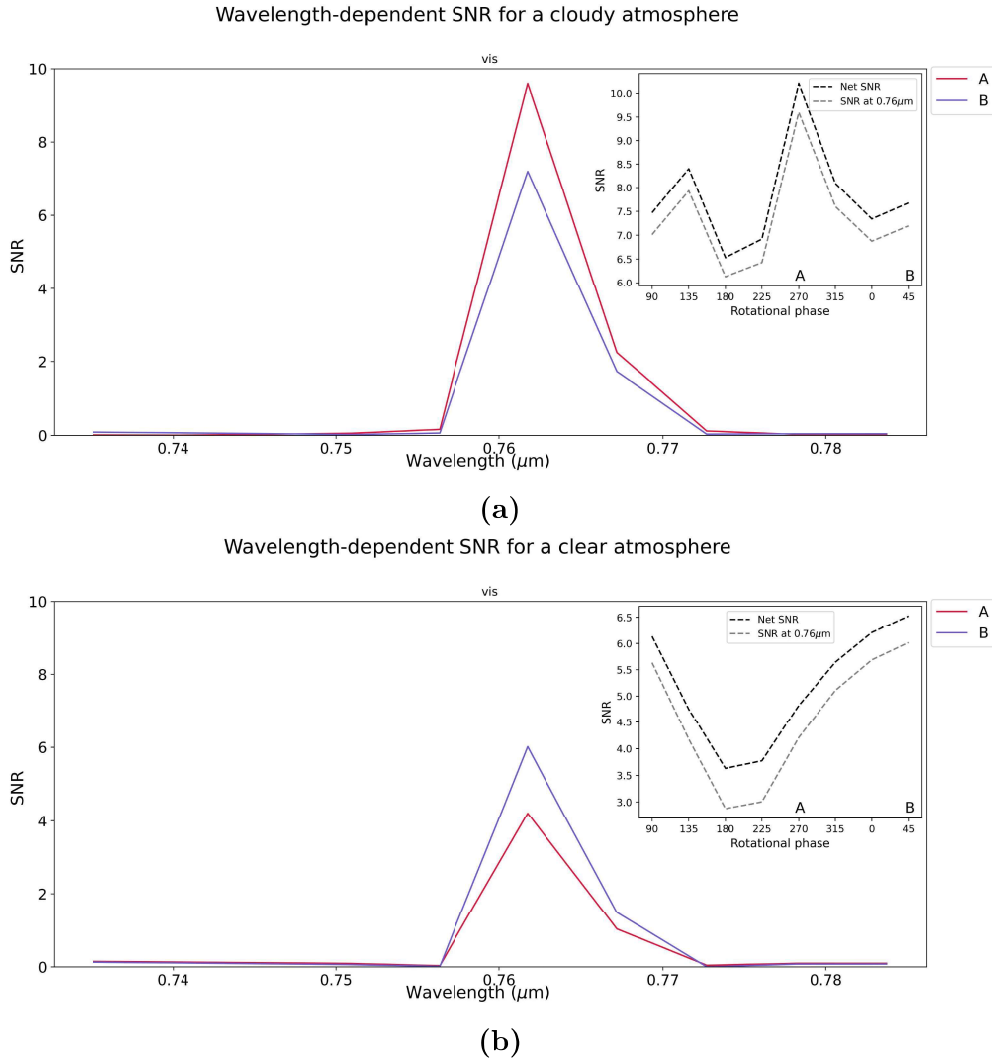
Figure 7.2: The wavelength-dependent SNR values that quantify the detectability of O_2 in the visible band for a (a) cloudy atmosphere and (b) clear atmosphere for the two discs A and B. The plot is centered around 0.76 μm, where O_2 shows the highest absorption. The insets show how the net SNR as well as the SNR at 0.76 μm evolves with the rotational phase.

Calculating the mass of O_2 in an atmospheric column : O_2 is a well-mixed gas with a mixing ratio of ~ 0.21 throughout the atmosphere. Assuming the atmosphere to be in hydrostatic equilibrium with a constant temperature profile, we estimate the mass of the O_2 column between two altitudes h1 and h2. Using the hydrostatic equation and the ideal gas equation,

$$dP = -\rho g dz \quad ; \quad dP = \frac{RT}{m_a} d\rho$$

where m_a is the molar mass of the atmosphere. Equating the two,

$$\frac{d\rho}{\rho} = -\frac{m_a g}{RT} dz$$

Integrating the equation from the surface to some height h,

$$\rho = \rho_s e^{-\frac{m_a g h}{RT}}$$

where ρ_s is the surface density. Again using the ideal gas equation,

$$\rho = \frac{m_a P_s}{RT} e^{-\frac{m_a g h}{RT}}$$

where P_s is the surface pressure. The mole density is given by

$$n = \frac{\rho}{m_a} = \frac{P_s}{RT} e^{-\frac{m_a g h}{RT}}$$

Since O_2 is a well-mixed gas, the mole density of O_2, $n_O = 0.21n$. The number of moles, N in a column between two heights h_1 and h_2 is

$$N = \int_{h_1}^{h_2} n_O A \, dh$$

where A is the area of the column. The mass of O_2 in the column is

$$M = N m_{O_2} = m_{O_2} \int_{h_1}^{h_2} n_O A \, dh$$

Integrating this equation yields,

$$M = 0.21 \frac{m_{O_2}}{m_a} \frac{P_s A}{g} \left(e^{-\frac{m_a g h_1}{RT}} - e^{-\frac{m_a g h_2}{RT}} \right) \tag{7.1}$$

Theoretical estimates of the SNR for a cloudy and clear atmosphere : We theoretically estimate the SNR values for a clear atmosphere and an atmosphere with a single layer of clouds using a simple radiative transfer model.
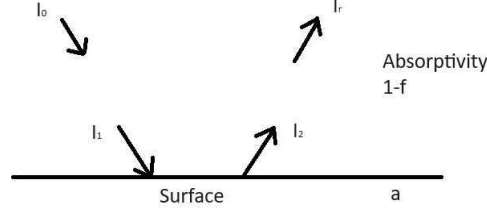
Figure 7.3: A schematic of the radiative transfer for a clear atmosphere.

Consider a clear atmosphere over a surface with albedo a. Consider a well-mixed gas with an absorptivity of 1-f or a transmissivity of f. Light of intensity I_0 is incident at the top of the atmosphere. As it passes through the atmosphere, a fraction $(1 - f)I_0$ is absorbed by the gas, and the intensity of light reaching the surface is

$$I_1 = fI_0$$

Since the surface has an albedo a, the intensity of light reflected from the surface is

$$I_2 = afI_0$$

As this reflected light passes through the atmosphere, a fraction of the light is again absorbed by the gas, and the intensity of light reaching the top of the atmosphere is

$$I_r = af^2I_0$$

In the absence of the gas, the intensity of reflected light at the top of the atmosphere would have been

$$I_r = aI_0$$

Thus, the signal can be calculated as

$$S_{clear} = aI_0 - af^2I_0 = aI_0(1 - f^2) \tag{7.2}$$

Figure 7.4: A schematic of the radiative transfer for an atmosphere with a single cloud layer.

Adding just a single cloud layer can significantly complicate this radiative transfer. Consider a single optically thin cloud layer with an albedo $A > a$. Since our gas is present throughout the atmosphere, a fraction F of the total gas mass lies below the cloud layer and subsequently a fraction 1-F lies above the cloud layer. We assume that the amount of light absorbed by the gas above and below the cloud layer is proportional to the total gas mass in these regions. Like before, assume light of intensity I_0 is incident at the top of the atmosphere. As it passes through the portion of the atmosphere above the cloud layer, the amount of light absorbed by the fraction of gas is

$$I_a = (1 - f)(1 - F)I_0$$

Thus the intensity of light reaching the top of the cloud layer is

$$I_1 = I_0 - I_a = (f + F - fF)I_0$$

The intensity of light reflected by the cloud layer is

$$I_2 = A(f + F - fF)I_0$$

As this light passes through the atmosphere over the cloud layer, a fraction of it is absorbed by the gas and the intensity of light reaching the top of the atmosphere is

$$I_{r1} = A(f + F - fF)^2 I_0$$

The intensity of light transmitted by the optically thin cloud layer is

$$I_3 = (1 - A)(f + F - fF)I_0$$

As this light passes through the atmosphere below the cloud layer, it is again absorbed by the gas and the amount of light reaching the surface is

$$I_4 = I_3(1 - F + fF)$$

The amount of light reflected by the surface is

$$I_5 = aI_3(1 - F + fF)$$

As this light passes through the atmosphere below the cloud layer, it gets attenuated due to absorption, and the intensity of light reaching the bottom of the cloud layer is

$$I_6 = aI_3(1 - F + fF)^2$$

Assuming the cloud is optically thin,

$$I_7 = I_6$$

A fraction of this light is absorbed by the gas present above the cloud layer and the intensity of light reaching the top of the atmosphere is

$$I_{r2} = I_0(1 - A)a(1 - F + fF)^2(f + F - fF)^2$$

The total intensity of reflected light at the top of the atmosphere is

$$I_r = I_{r1} + I_{r2} = A(f + F - fF)^2 I_0 + I_0(1 - A)a(1 - F + fF)^2(f + F - fF)^2$$

In the absence of the gas, the intensity of reflected light at the top of the atmosphere would have been

$$I_r = I_0 A + I_0 a(1 - A)$$

Thus, the signal can be calculated as

$$S_{cloud} = I_0 A[1 - (f + F - fF)^2] + I_0 a(1 - A)[1 - (1 - F + fF)^2(f + F - fF)^2] \qquad (7.3)$$

There are a few caveats with this computation - (i) we have assumed that the cloud bottom is optically thin and transmits all the incident light, and (ii) by doing so, we have also neglected the greenhouse effect of clouds. But even this simple estimate provides a quantitative understanding of how clouds affect the SNR. Let's consider a few cases to compare the two signals for the clear and cloudy atmosphere.

1. If the gas is mostly present above the cloud layer (for eg, O_3), $F \approx 0$. Then,

$$S_{cloud} = I_0 A(1 - f^2) + I_0 a(1 - A)(1 - f^2) = I_0 a(1 - f^2)[\frac{A}{a} + (1 - A)] \qquad (7.4)$$

   Since $A > a$, $S_{cloud} > S_{clear}$. Since the gas is present above the cloud layer, the clouds increase the reflectivity and boost the signal, making it easier to detect the gas.

2. If the gas is present below the cloud layer, (for eg, H_2O), $F \approx 1$. Then,

$$S_{cloud} = I_0 a(1 - f^2)(1 - A) < S_{clear} \qquad (7.5)$$

   Since the gas is present below the cloud layer, the high albedo of the clouds makes it difficult to probe the atmosphere below the cloud layer, thus making it harder to detect the gas.

3. If the gas is equally distributed above and below the cloud layer (for eg a well-mixed gas like O_2), $F \approx 0.5$. In this case,

$$S_{cloud} = I_0 \{ \frac{A}{a} [1 - (\frac{f}{2} + \frac{1}{2})^2] + (1 - A)[1 - (\frac{f}{2} + \frac{1}{2})^4] \} \qquad (7.6)$$

   Depending on the exact values of A, a, and f, this signal is either lower or higher than S_{clear}.

The results provided above show that the SNR values for a well-mixed gas depend on the albedo of the clouds, the albedo of the surface, the absorptivity of the gas, and finally on the amount of gas present above and below the cloud layer. However, the simple analysis presented above is for a single cloud layer. In reality, this analysis is complicated by the fact that Earth is not covered by a single optically thin cloud layer but has patches of clouds of different sizes and optical depths. Nevertheless, we can come up with a rough estimate of the signal by analyzing the effect of clouds present at different altitudes.

Assume that the average albedo of the surface, a ≈ 0.3[1] and the transmissivity of O_2 at its most prominent absorption line at 0.76μm is 0.4 (see figure B.1 in Appendix A). We consider a single layer of cloud at three different altitudes in the atmosphere. Using eq. 7.1, we estimate the amount of O_2 present above and below the cloud layer. While calculating the amount of O_2 present above the cloud layer, we assume that the atmosphere extends uptil 100km. We insert this value of F along into eq. 7.3 to compute the signal. Table 7.1 compares the signals for the cloud layers present at three different altitudes in the atmosphere.

Cloud-type	Average cloud top height (km)	Average albedo	F	S_{clear}	S_{cloud}
Cumulus (low-level)	1.1	0.75	0.125	$0.25I_0$	$0.64I_0$
Alto-cumulus (mid-level)	4.5	0.7	0.4	$0.25I_0$	$0.57I_0$
Cirrostratus (high-level)	9.5	0.35	0.68	$0.25I_0$	$0.27I_0$

Table 7.1: A comparison of the signals for a clear and cloudy atmosphere with a single layer of cloud present at different altitudes.

It is evident that for a well-mixed gas like O_2, $S_{cloud} > S_{clear}$ for all the three cases. This analysis presents a simple computation to explain why clouds tend to increase the detectability of O_2. We have presented a simple radiative transfer model consisting of only one cloud layer but in reality, the radiative transfer in the Earth's atmosphere is extremely complicated as the vertical cloud distribution is a combination of different types of clouds at varying altitudes. However, we can still, in principle calculate the signal values by considering the effect of each cloud layer separately. These results also explain the trends seen in the inset plots in figure 7.2. From eq. 7.2, we can see that the signal is proportional to the albedo of the surface in the absence of clouds. Thus, in the absence of clouds, the trend in the SNRs matches the trend in the net albedo of the surface as the planet rotates. On the other hand, in the presence of clouds, the signal depends on a variety of factors and the trend in SNR

---

[1] https://earthobservatory.nasa.gov/images/84499/measuring-earths-albedo

shows no correlation with the albedo of the surface.

To quantify the effect of individual cloud layers, we came up with a simplified model where our remote Earth is completely covered by a single cloud layer. We assume that this cloud is composed of a molecule X which is not present in the atmosphere. In doing so, we simply assume that the cloud composition and opacity are independent of the atmospheric composition and temperature profile. We vary the altitude and thickness of this cloud layer and compute the SNRs in each case. Figure 7.5 shows the SNR values in the visible band for an atmosphere with a surface cloud layer of varying thickness. The SNRs increase with increasing thickness as the reflectivity of the cloud layer increases with thickness. Even though increasing the thickness leads to a slightly lower fraction of O_2 above the cloud layer, this is compensated by the higher reflectivity of a thicker cloud. This is because a large fraction of O_2 is still present above the cloud layer. Note that by covering the entire globe with a single cloud layer, the net albedo of the disc is dominated by the surface, as the cloud layer contributes equally to all portions of the disc. Since disc B has a higher surface albedo, it shows higher SNRs in this case. Also, as the cloud thickness increases, the contribution of the surface starts reducing as it becomes more and more difficult to probe the surface lying below the cloud layer. Thus, the disparity in the SNRs starts reducing as the cloud thickness is increased.

However, for high-level clouds, present at an altitude of ∼13 km, we observe an opposite trend, the SNRs decrease with increasing thickness. This is because O_2 starts becoming scarce high up in the atmosphere, and as we increase the cloud thickness it becomes more difficult to probe the atmosphere below which is where almost all of the O_2 lies. Thus in this case, the fraction of O_2 becomes the controlling factor and the increase in albedo with cloud thickness is not sufficient to compensate for the decreasing fraction of O_2 above the cloud layer. This is evident from figure 7.6 which shows that the SNRs reduce for increasing cloud thickness for high-level clouds.

We did a similar analysis for cloud layers at altitudes 2km (low-level clouds) and 7.5 km (mid-level clouds). For low-level clouds, the SNRs increase with thickness as there is still sufficient oxygen above the cloud layer. For mid-level clouds, the two competing factors contribute equally and the SNRs remain roughly constant with increasing cloud thickness. Figure 7.7 concisely shows these results for disc A regarding how the SNRs at $0.76\mu m$ vary for cloud layers with varying cloud thicknesses and altitudes. The SNRs are color-coded and

the size of each dot is proportional to the cloud thickness. The SNRs decrease with altitude as the fraction of O_2 above the cloud layer starts decreasing. Note that there is one caveat with this analysis. We have assumed that the clouds at different altitudes have the same optical thickness, which in reality, is not true. As the water vapor distribution varies with altitude, the optical thickness of clouds at different altitudes becomes different. Clouds are typically optically thin at high altitudes and thick at low altitudes. If we do this analysis in a physically consistent manner, we would have to make the clouds optically thinner at higher altitudes. In that case, we wouldn't expect a substantial decrease in SNR with cloud altitude since the clouds become optically thinner with altitude, it gets easier to probe the atmosphere below.

7.2 Detectability of H_2O

We follow a similar analysis for other gases like H_2O. Figure 7.8 compares the spectrum of disc A for a default atmosphere and an atmosphere without H_2O. Again, the two spectra match except in the shaded regions where water vapor shows high absorption in the visible and near-infrared. For this case as well, we follow the same procedure to compute the SNRs from the theoretical model spectra. Similarly, figure 7.9 shows the simulated reflected light spectra for a cloudy and a clear atmosphere without H_2O for the two cases A and B. The shaded regions depict the regions of absorption by H_2O.

Since, H_2O shows high absorption both in the visible and near-infrared, we present our SNR plots for both these wavelength bands. Figure 7.10 depicts the SNRs for H_2O in the visible band for a cloudy and a clear atmosphere for the two discs A and B. As before, since disc A has more cloud coverage, it has a higher albedo and thus a higher SNR than disc B. In the absence of clouds, disc B has a higher surface albedo which leads to a higher SNR. Note that the water in clouds is either present in liquid or solid phase and these phases of water have different absorption signals than the signal of water vapor, which is H_2O in the gas phase. Water vapor has prominent absorption bands ranging from the visible band to the infrared, but clouds absorb mostly in the mid-infrared and the far-infrared (which is why they are such an important contributor to the greenhouse effect). Thus, an increase in SNR in the presence of clouds is not due to the presence of more water in the atmosphere stored in clouds but rather due to an increase in the albedo of the disc in the presence of clouds. Figure 7.11 shows a similar plot, depicting the SNRs for H_2O in the near-infrared band for a cloudy and a clear atmosphere for the two discs A and B. In this case, we cannot do a similar

quantitative estimation of the SNR for a clear and cloudy atmosphere because, unlike oxygen, H_2O is not a well-mixed gas. Its mixing ratio varies with altitude and thus computing the mass of H_2O in an atmospheric column becomes much more complex.

(a)

(b)

(c)
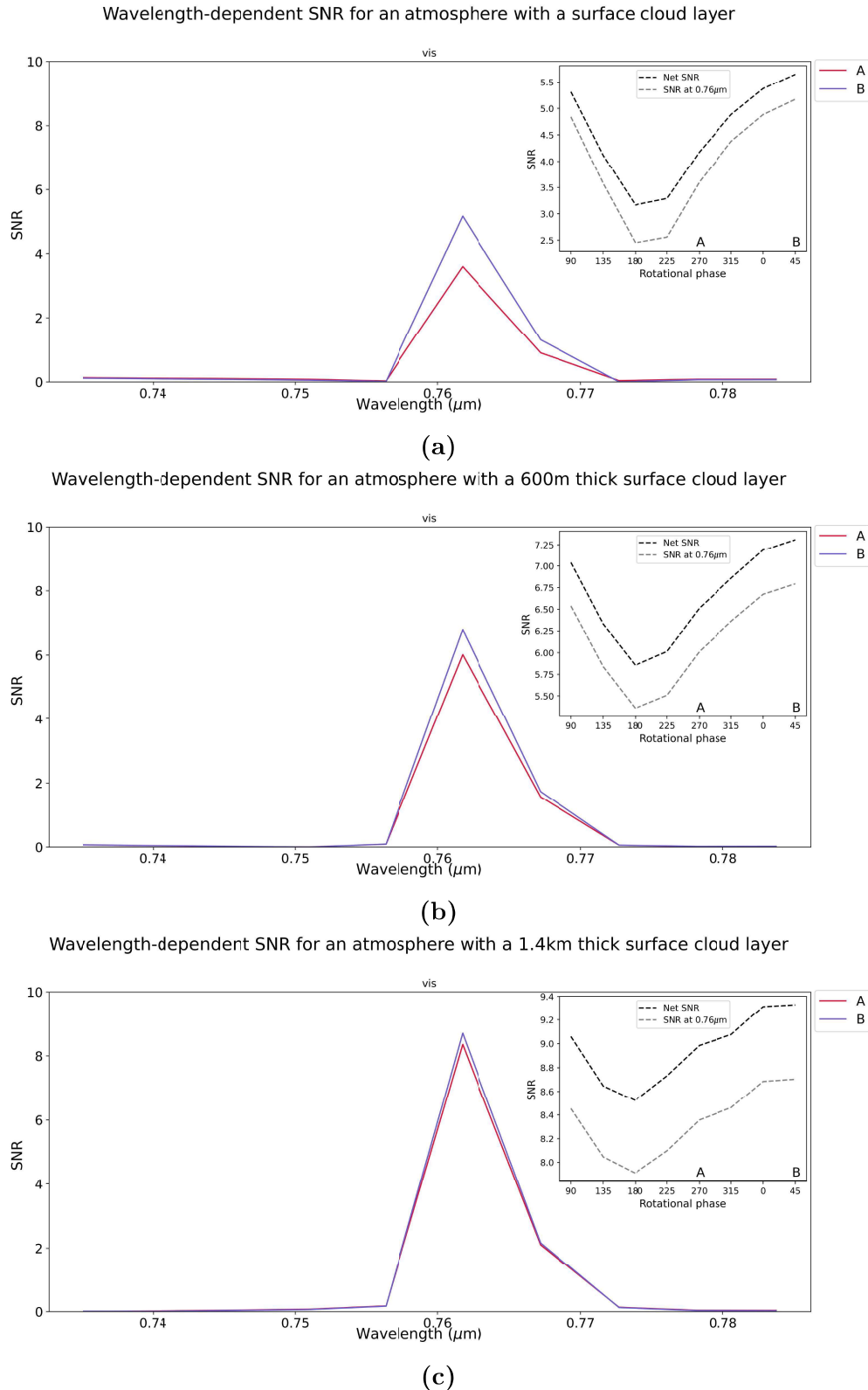
Figure 7.5: The wavelength-dependent SNR values of O_2 centered around 0.76μm in the visible band for an atmosphere with a surface cloud layer of thickness (a) ~ 0m, (b) 600 m, and (c) 1.4 km. The insets show how the net SNR as well as the SNR at 0.76 μm evolves with the rotational phase.

(a)

(b)
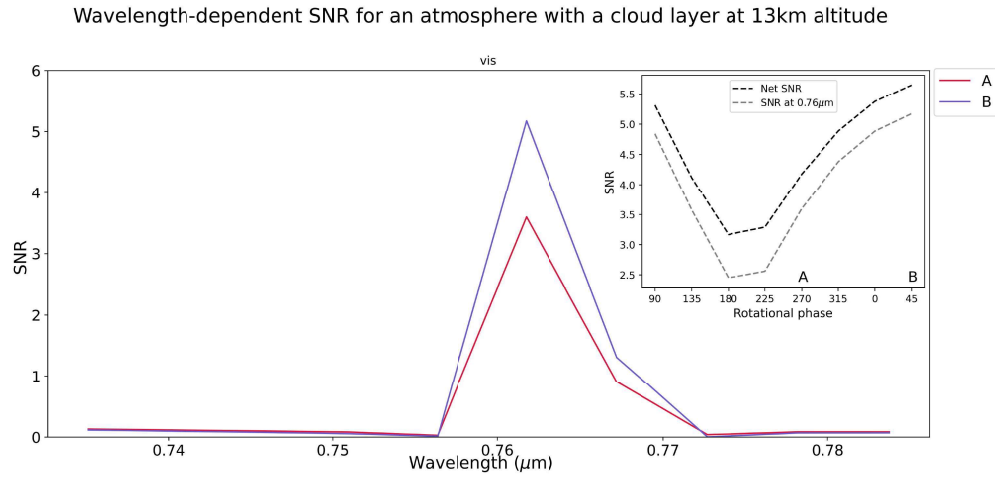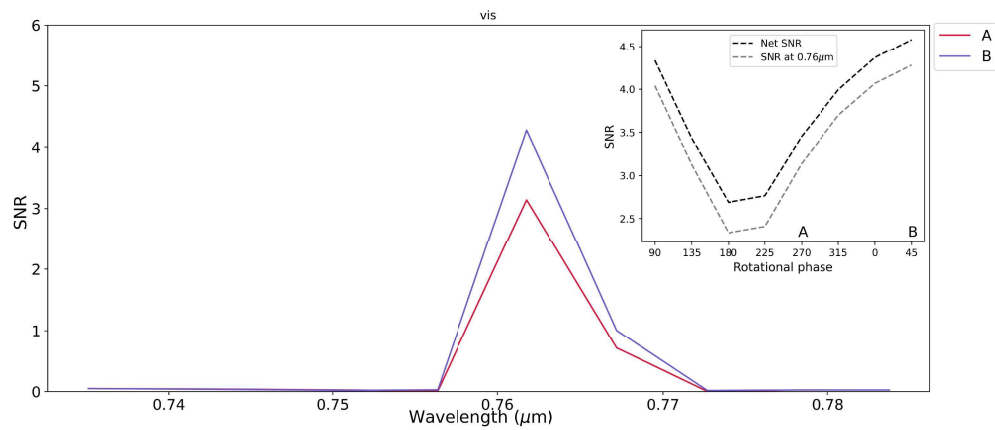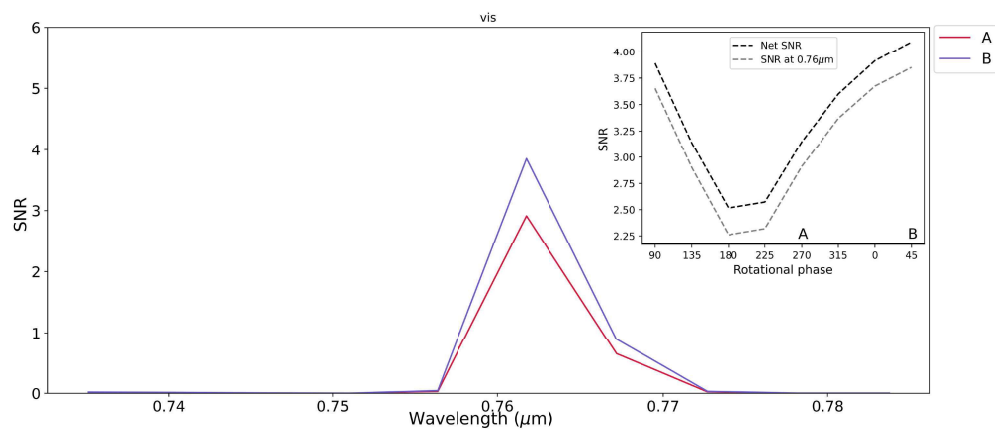
(c)

Figure 7.6: The wavelength-dependent SNR values of O_2 centered around $0.76\mu m$ in the visible band for an atmosphere with a cloud layer at ~13km with thickness (a) ~ 0m, (b) 1 km, and (c) 2 km. The insets show how the net SNR as well as the SNR at 0.76 μm evolves with the rotational phase.
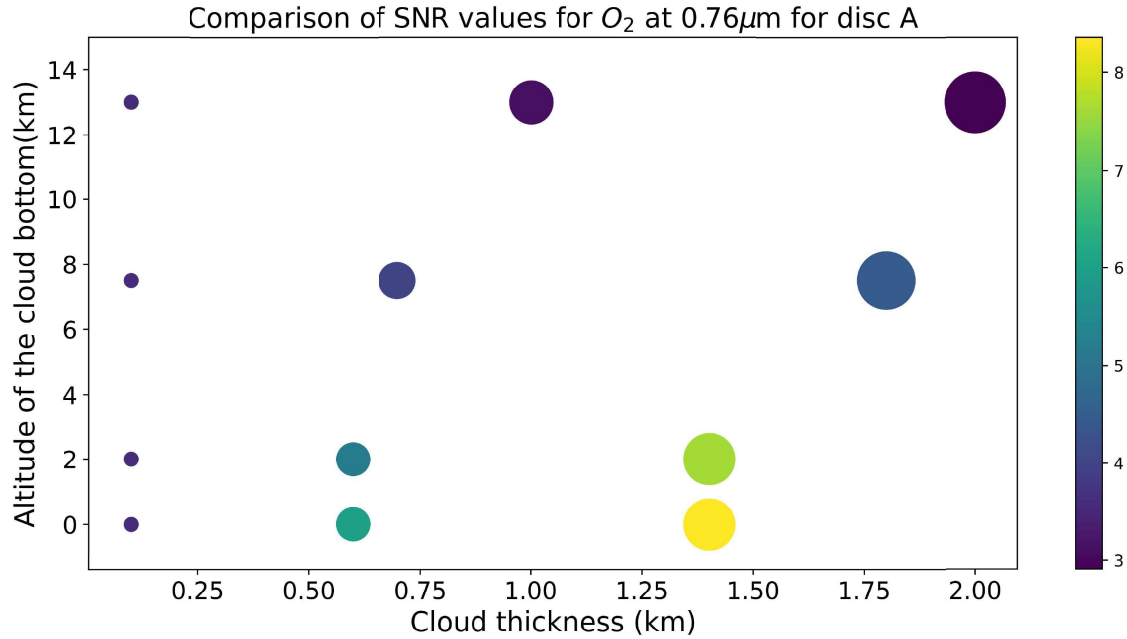
Figure 7.7: A comparison of the SNRs for O_2 at $0.76\mu m$, its most prominent absorption feature in the visible band, for cloud layers of varying altitudes and thicknesses. The colors represent the SNRs value at $0.76\mu m$ and the size of each circle is proportional to the cloud thickness.
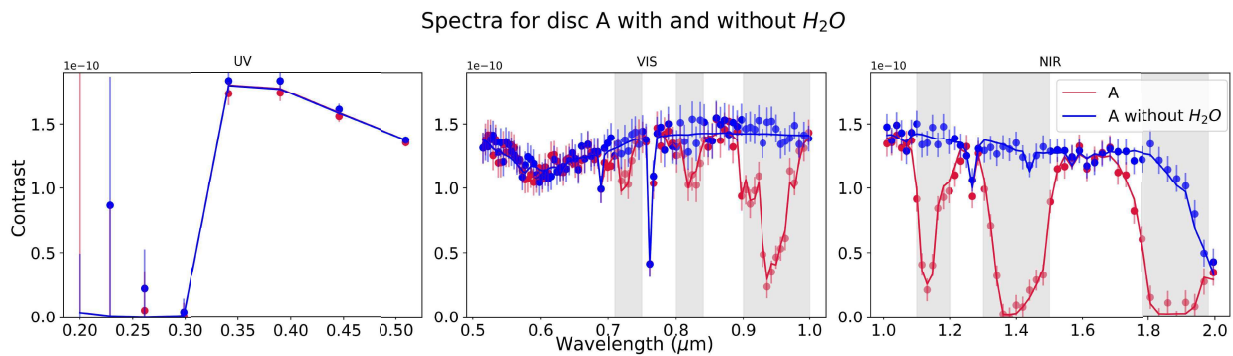
Figure 7.8: Spectrum of disc A for a default atmosphere and an atmosphere without H_2O. Water vapor mainly absorbs in multiple bands across the visible and near-infrared and these absorption bands are shaded in the plot.

To quantify the effect of clouds, we perform a similar analysis where we compute the SNRs of H_2O in the visible and near-infrared band for atmospheres with cloud layers of varying thickness at different altitudes. Figure 7.12 shows how the net SNRs for H_2O in the visible band vary for cloud layers with varying cloud thicknesses and altitudes.

Figure 7.9: Reflectance spectra for a (a) cloudy atmosphere and (b) clear atmosphere without H_2O for the two cases A and B. The shaded regions depict the absorption bands of H_2O in the visible and near-infrared.

The SNRs are color-coded and the size of each dot is proportional to the cloud thickness. As before, we see that the SNRs increase with cloud thickness for surface clouds and decrease with cloud thickness for high-level clouds, due to reasons mentioned above. Looking at figure 2.1b, H_2O is not a well-mixed gas and its mixing ratio exponentially decreases with height uptil 0.1 bar after which it remains roughly constant. So a majority of the water vapor is present at low altitudes in the atmosphere, below the altitudes of mid-level clouds. The trend in SNR shifts to low altitudes, even for mid-level clouds, the SNRs reduce with cloud thickness as the increasing reflectivity is not sufficient to compensate for the difficulty in probing the atmosphere below. For low-level clouds, these two effects contribute equally and the SNRs remain roughly constant with increasing thickness. Figure 7.13 shows a similar plot depicting the net SNRs of H_2O in the near-infrared band. Since H_2O has a higher absorptivity in the near-infrared, the net SNRs are higher. This high absorptivity also ensures that even for mid-level clouds, the SNRs increase with cloud thickness.

Wavelength-dependent SNR for a cloudy atmosphere

(a)

Wavelength-dependent SNR for a clear atmosphere

(b)

Figure 7.10: The wavelength-dependent SNR values that quantify the detectability of H_2O in the visible band for a (a) cloudy atmosphere and (b) clear atmosphere for the two discs A and B. The insets show how the net SNR evolves with the rotational phase.

(a)

(b)
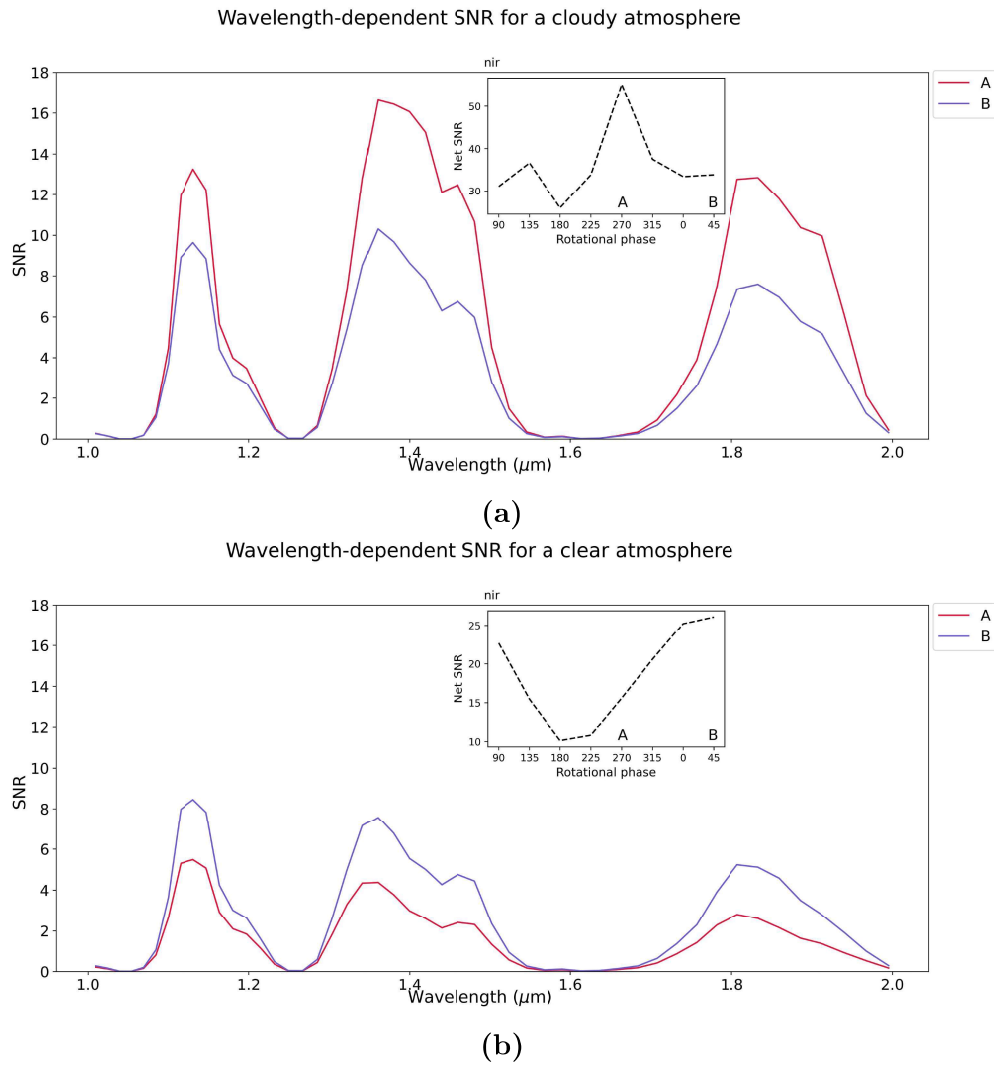
Figure 7.11: The wavelength-dependent SNR values that quantify the detectability of H_2O in the near-infrared band for a (a) cloudy atmosphere and (b) clear atmosphere for the two discs A and B. The insets show how the net SNR evolves with the rotational phase.

Figure 7.12: A comparison of the net SNRs for H_2O in the visible band for cloud layers of varying altitude and thicknesses. The colors represent the SNRs and the size of each circle is proportional to the cloud thickness.
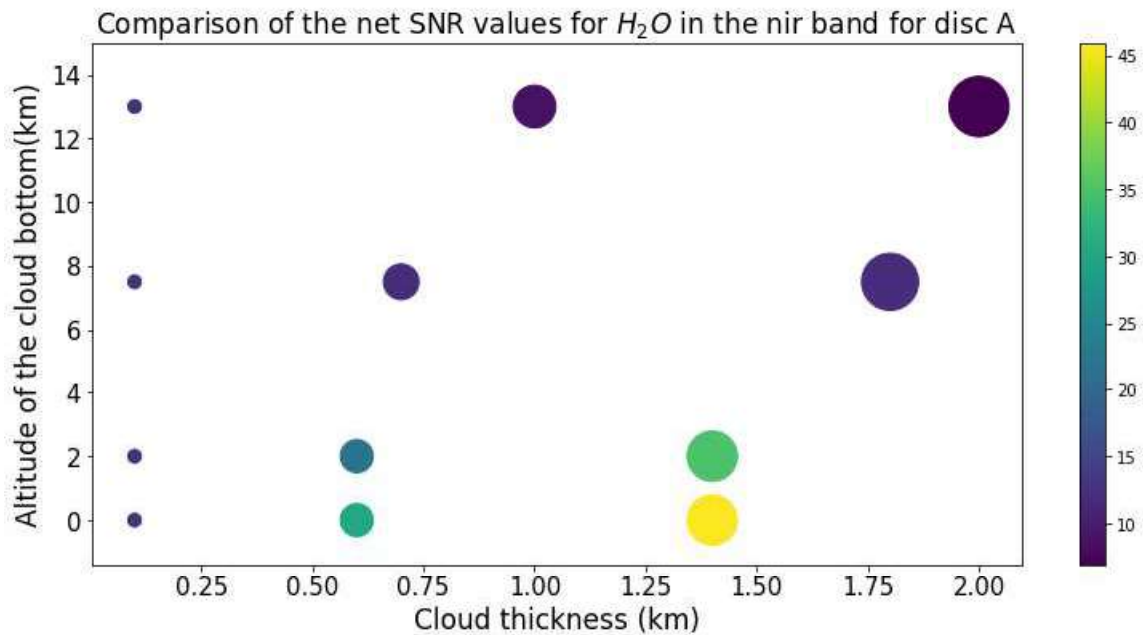
Figure 7.13: A comparison of the net SNRs for H_2O in the near-infrared band for cloud layers of varying altitude and thicknesses. The colors represent the SNRs and the size of each circle is proportional to the cloud thickness.

7.3   Detectability of O_3

Similarly, figure 7.14 compares the spectrum of disc A for a default atmosphere and an atmosphere without O_3. The two spectra match except in the shaded regions where ozone shows absorption in the uv and visible. Figure 7.15 shows the simulated reflectance spectra for a cloudy atmosphere and a clear atmosphere respectively without O_3 for the two cases A and B. The shaded areas depict the missing absorption bands in the uv and visible, where O_3 has absorption bands.
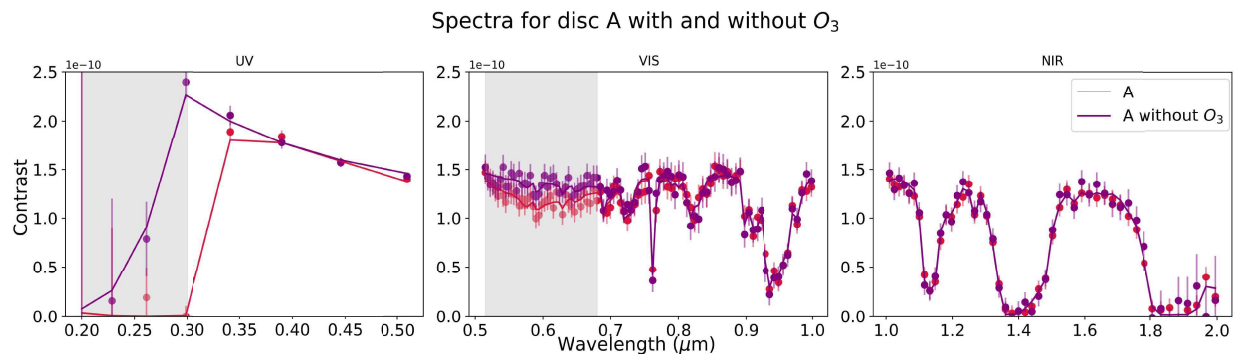
Figure 7.14: Spectrum of disc A for a default atmosphere and an atmosphere without O_3. Ozone shows prominent absorption in the uv band with a low absorption band in the visible. These absorption bands are shaded in the plot.

Since O_3 shows prominent absorption in the uv, we present our SNR plots only for the uv band. Figure 7.16 shows the SNRs for O_3 in the uv band for a cloudy and a clear atmosphere for the two discs A and B. The presence of clouds again enhances the SNRs and improves the detectability of O_3 in the uv band. In the absence of clouds, the SNRs for both the discs are almost equal and even the inset shows that the net SNRs are roughly constant with rotational phase. This can be attributed to two reasons - (a) the net albedos of the discs corresponding to different rotational phases are roughly similar in the uv band (see figure B.4 which shows the simulated reflectance spectra for a bare exo-Earth without an atmosphere), which is where O_3 has the highest absorptivity, and (b) Ozone is abundant high up in the atmosphere, far away from the surface (see figure 2.1b which shows that ozone is about 5 magnitudes less abundant than water vapor near the surface). Thus, the light reaching this ozone layer has already been affected by other processes like Rayleigh scattering, collision-induced absorption, and absorption by O_2 (at 0.23 μm). Thus the reflectivity of the surface has a negligible effect on the detectability of O_3 and it is the distribution of clouds that dominates.
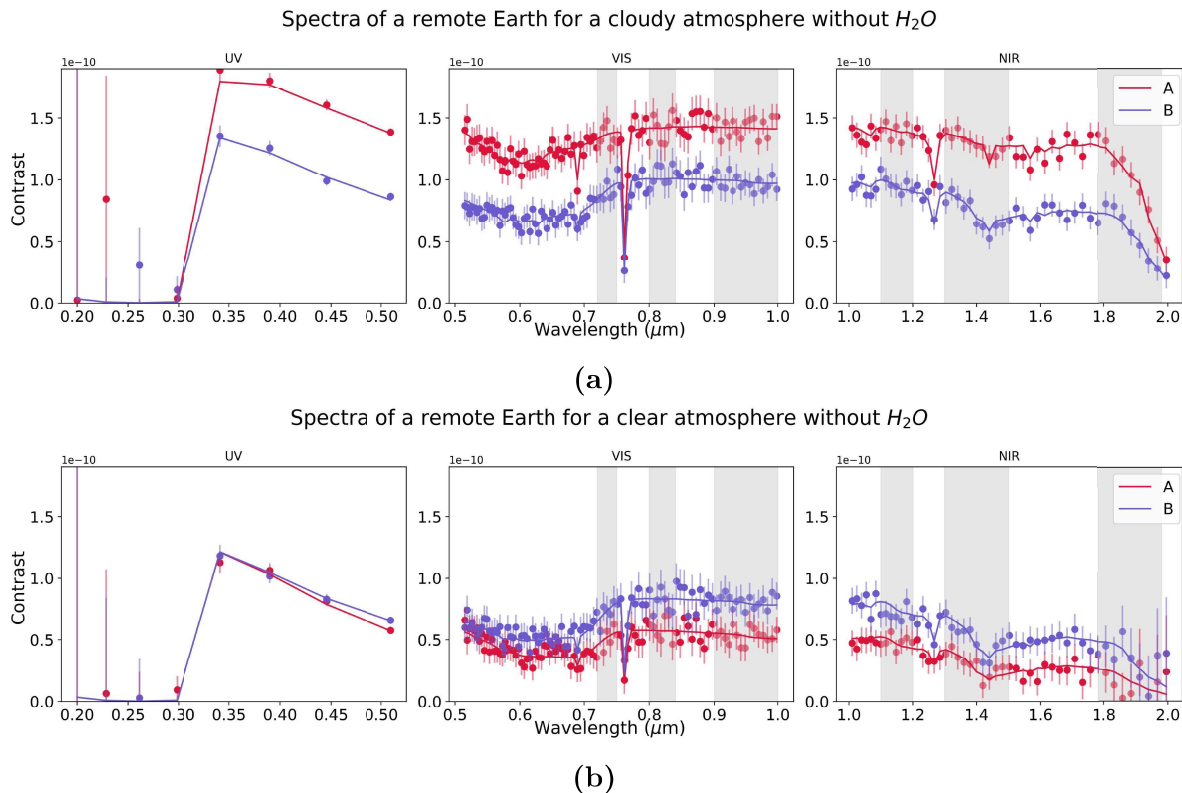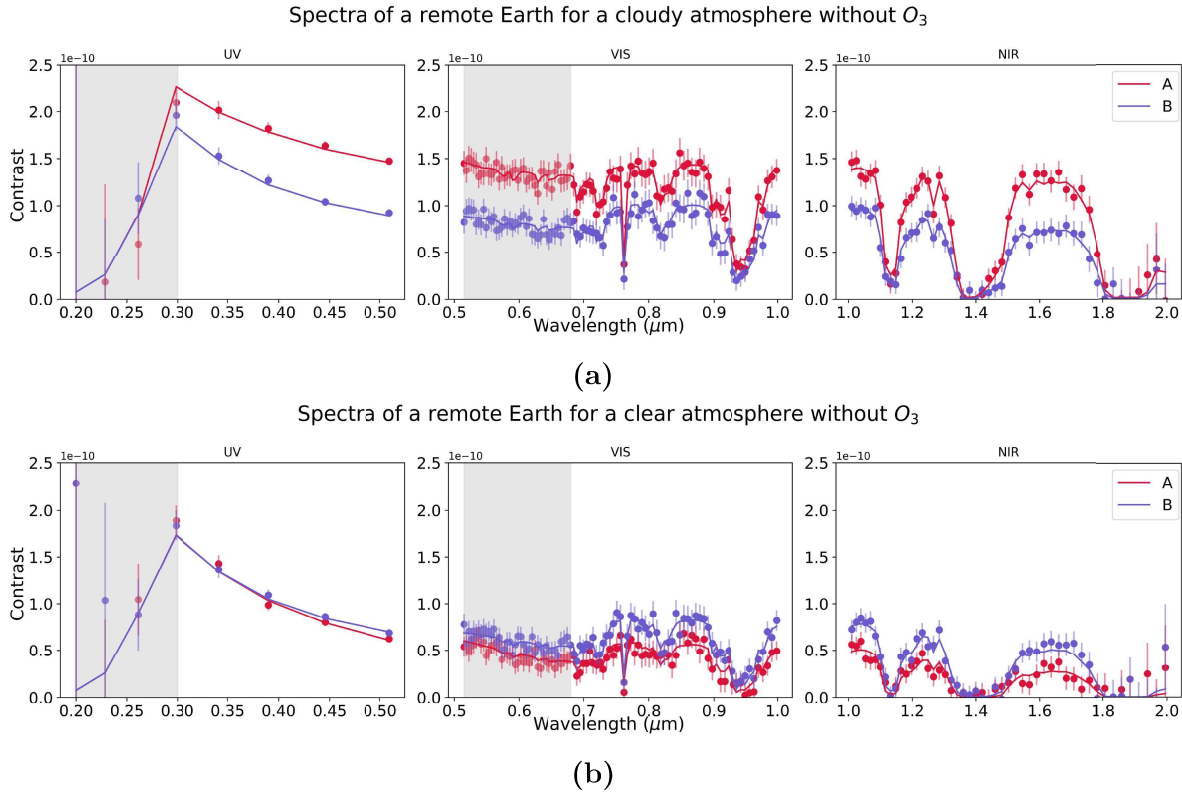
Figure 7.15: Reflectance spectra for a (a) cloudy atmosphere and (b) clear atmosphere without O_3 for the two cases A and B. The shaded areas depict the missing absorption bands in the UV and visible.

To again quantify the effect of clouds, we compute the SNRs for different atmospheres with a single cloud layer of varying altitude and thickness, as shown in figure 7.17. The SNR trend is shifted to higher altitudes in this case. A majority of ozone is present at high altitudes where it forms by photodissociation of O_2. Thus for surface, low-level, and mid-level clouds, the SNRs increase with cloud thickness as there is sufficient ozone above the cloud layer and the reflectivity of the clouds is the dominant factor. Only for high-level clouds, the two competing factors contribute equally, and the SNRs remain roughly constant with increasing thickness.

(a)

(b)
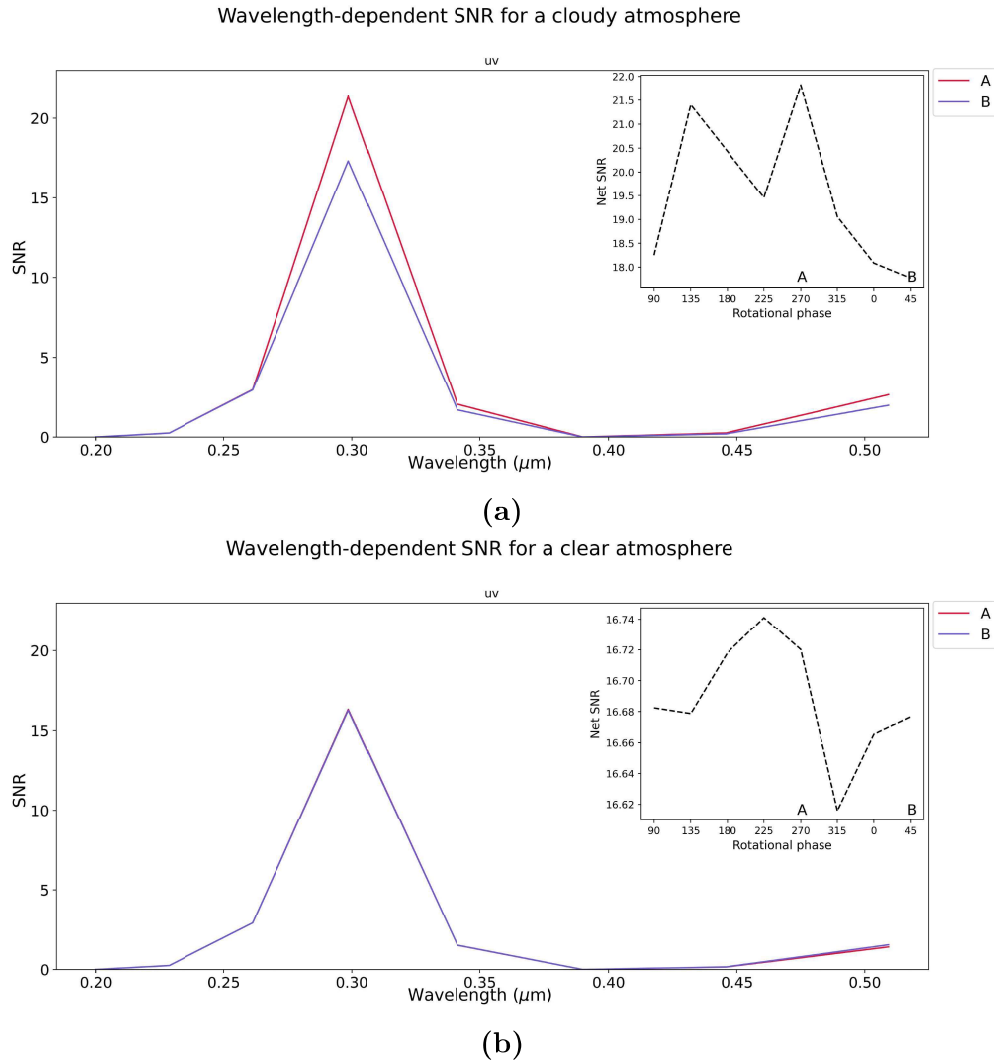
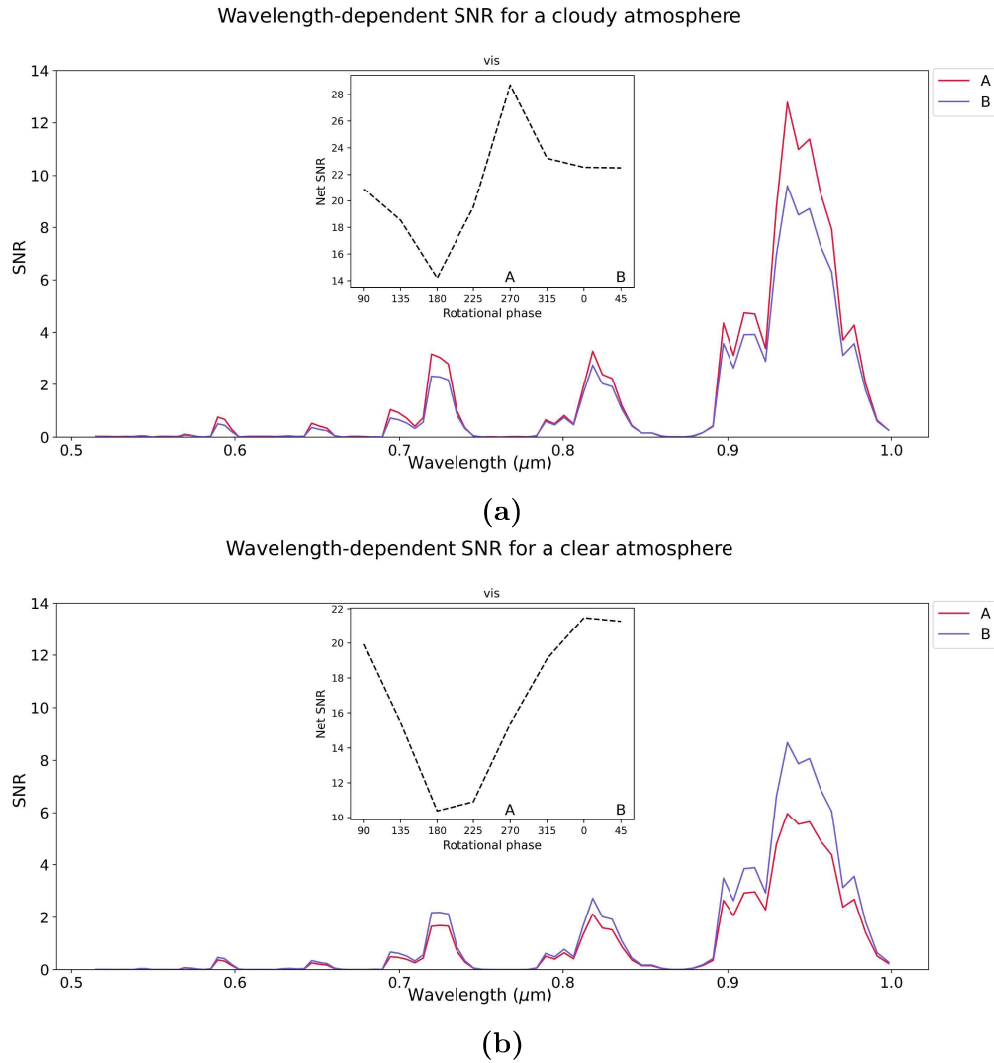**Figure 7.16:** The wavelength-dependent SNRs that quantify the detectability of O_3 in the uv band for a (a) cloudy and (b) clear atmosphere. The insets depict how the net SNRs evolve with the rotational phase.
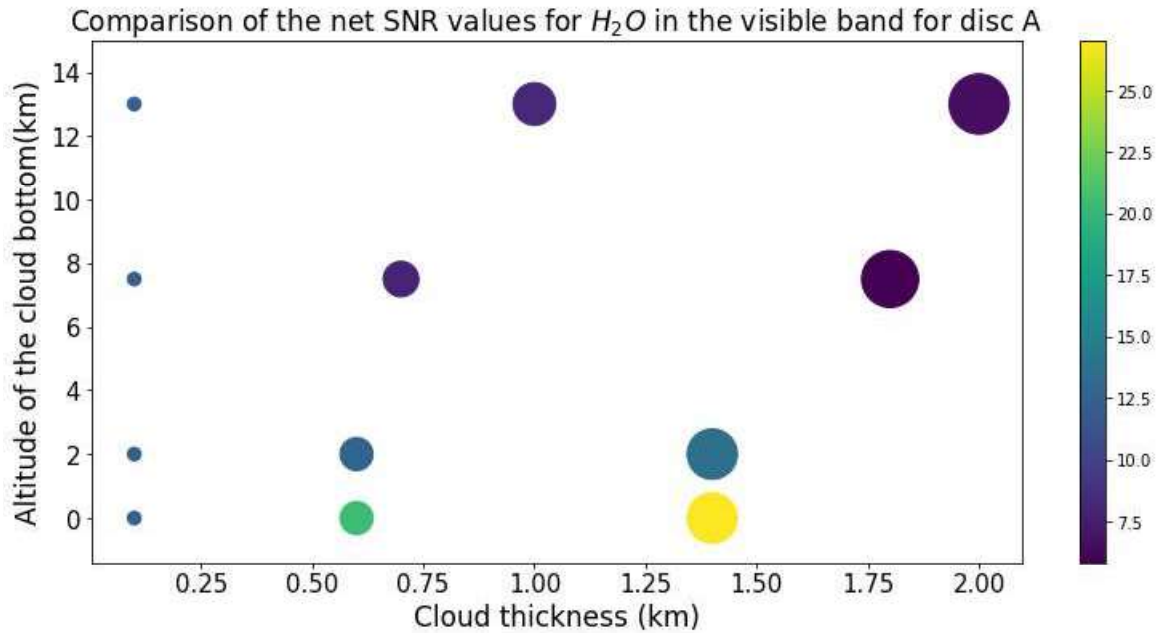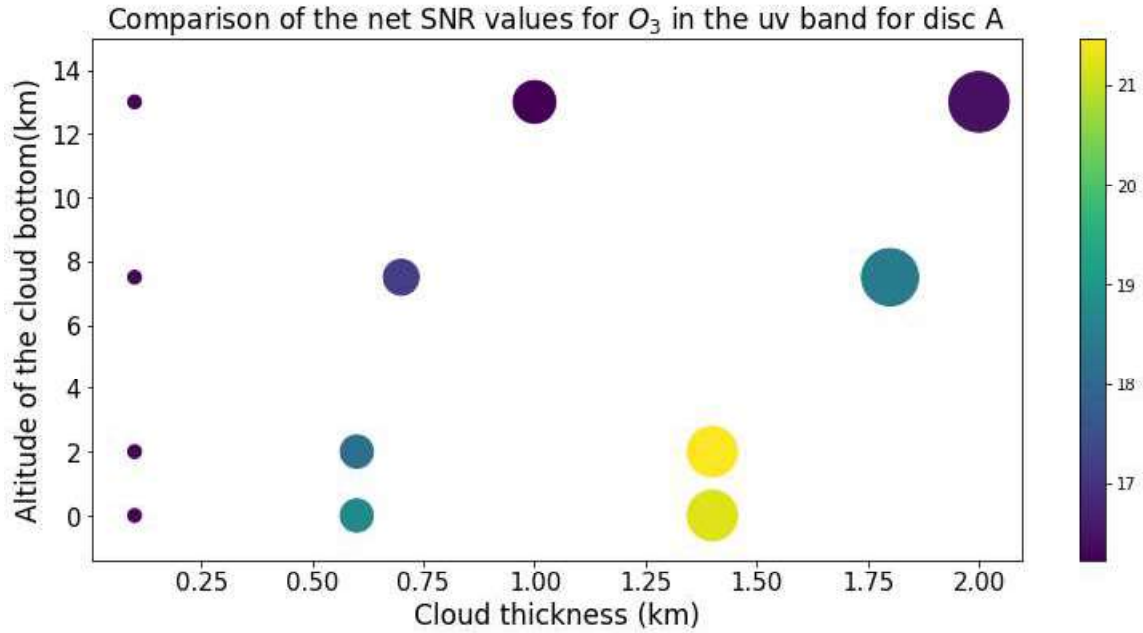
Figure 7.17: A comparison of the net SNR values for O_3 in the uv band for cloud layers of varying altitudes and thicknesses. The colors represent the SNRs and the size of each circle is proportional to the cloud thickness.

7.4 Comparison of the SNRs for all gases

Figure 7.18 concisely summarizes all the results presented in the sections above. The y-axis shows the rotational phase of the disc and the x-axis denotes the three gases, their corresponding wavelength bands in which they show absorption, and whether the atmosphere is cloudy or clear. The net SNRs are color-coded. For all three gases, SNRs are higher in the presence of clouds than without, for reasons explained in the previous sections. Amongst all the gases, the water vapor absorption band in the near-infrared has the highest detectability, followed by H_2O in the visible band and O_3 in the uv having roughly similar SNRs and finally O_2 in the visible. O_2 is the only gas that has a narrow absorption line, the rest of the gases all have wide absorption bands which is why they have such high net SNRs.

Now usually, instruments do not cover an entire wavelength band in one observation. The entire wavelength band is divided into bandpasses and not all of them are active. Given this observational constraint, the detection of O_2 becomes easier as its narrow absorption line lies within a single bandpass. Wider absorption bands for H_2O and O_3 may lie in multiple

bandpasses and thus multiple observations are needed to cover the entire absorption signal.
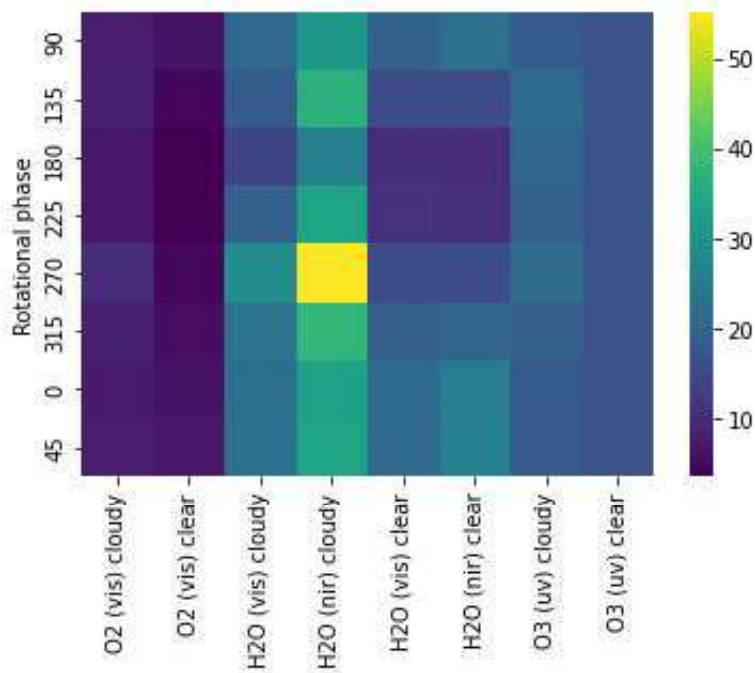
Figure 7.18: A comparison of the net SNRs for all the three gases, O_2, H_2O and O_3 in the corresponding wavelength bands as shown in the bracket and for a clear and a cloudy atmosphere. The rotational phase of the disc is plotted along the y-axis.

Moreover, we have simulated all our results with an exposure time of 3 hours assuming that the instrument will simultaneously observe in all 3 wavelength bands. This might not be the case as the instrument specifications for HWO concepts are still under consideration. This means that all our results should be taken with a pinch of salt, as these are obtained in the most ideal scenarios possible. When we go out and actually try to observe and detect atmospheric constituents, we should always expect to do worse than what our simulations and models suggest.

Figure 7.19 shows a comparison of the net SNRs for all the three gases, O_3 (in the uv band), H_2O (in the near-infrared band) and O_2 (in the visible band) for different atmospheres with a cloud layer of varying altitude and thickness. The wavelength bands are chosen such that the corresponding gas shows the maximum absorptivity in that band. For the sake of clarity, there is no color bar to denote the SNRs here, instead the size of each circle is proportional to the SNR. For atmospheres with surface and low-level clouds, water vapor

has the highest detectability as it has multiple absorption bands in the near-infrared. But for atmospheres with mid and high-level clouds, ozone is more detectable as the amount of water vapor starts reducing at higher altitudes while ozone is mainly present at high altitudes. For all cases, O_2 has the lowest SNRs because it only has one narrow absorption line in the visible where it shows prominent absorption.
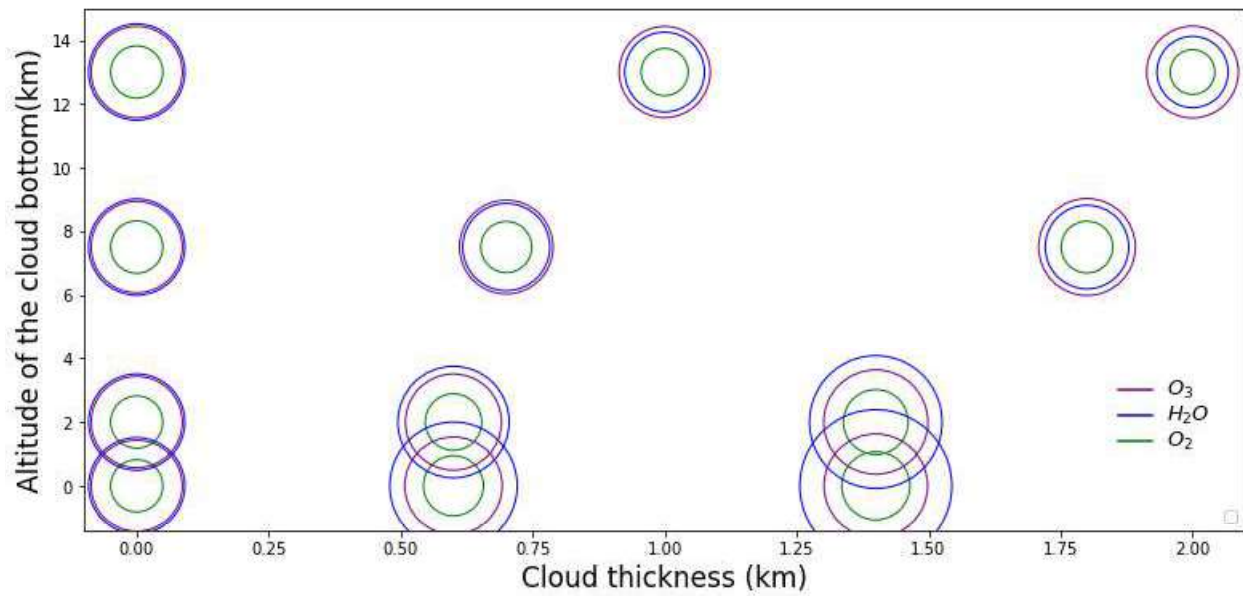
Figure 7.19: A comparison of the net SNRs for all the three gases, O_3 (in the uv band), H_2O (in the near-infrared band) and O_2 (in the visible band). The size of each circle is proportional to the SNR value.

Chapter 8

Comparing observations at different orbital phases

8.1 A Note on Phases

There are two phase-related quantities which describe the planet-star-observer system, (i) the orbital phase which denotes the position of the planet in its orbit, and (ii) the rotational phase which denotes the central longitude of the disc facing the observer. Figure 8.1 depicts a planet with a circular orbit around its host star. The orbital phases label the corresponding position of the planet in its orbit. Figure 4.2 depicts the rotational phases for a planet at orbital phase 270. Note that the rotational and orbital phases are not entirely independent of each other.

Consider the planet at two different orbital phases, 270 and 300 as shown in figure 8.2. At both these positions, the solar longitude which is the central longitude of the disc facing the Sun is l. The observer is sufficiently far away from the star-planet system. Thus, given the inherent geometry, the central longitude of the disc facing the observer i.e. the rotational phase is $l + 90$ and $l + 60$ respectively for the two cases. This places a constraint on the solar longitude-rotational phase pair of values at a given orbital phase.
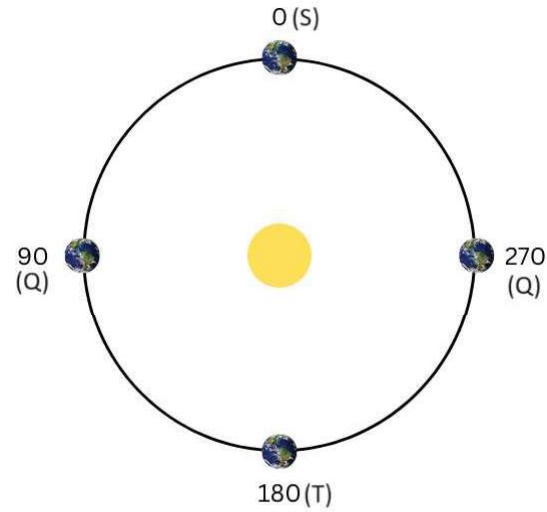
Figure 8.1: Circular orbit of a planet with each position labeled by the corresponding orbital phase value. The observer is assumed to be situated towards the bottom of the page. The letters in the bracket describe the orbital position - (T) Transit, (Q) Quadrature, and (S) Secondary eclipse.

(a)

(b)
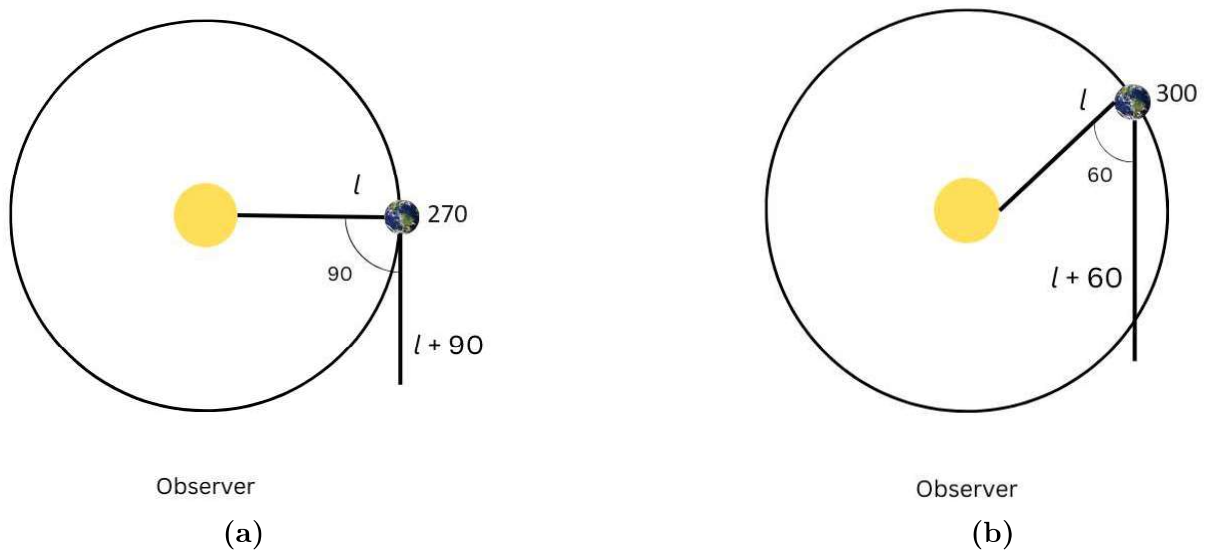
Figure 8.2: The relation between the orbital phase and the rotational phase for a planet at two different orbital positions.

8.2 A comparison between reflectance spectra

As shown in figure 8.1, the orbital phase denotes the position of the planet in its orbit around the host star with respect to an observer. Consider our remote Earth system with an edge-on orbit which means that as the planet goes around the star, it appears to move back and forth across a straight line in the sky.
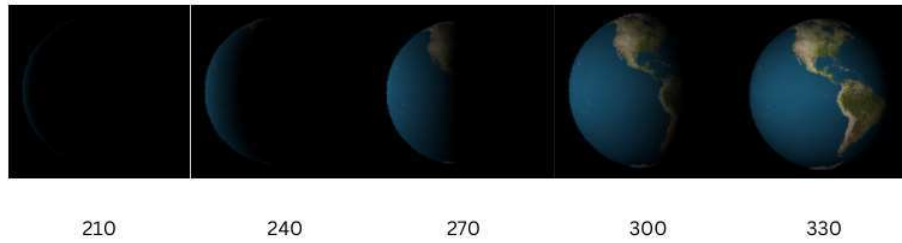
Figure 8.3: Illuminated portion of the disc at different orbital phases for a rotational phase = 270.
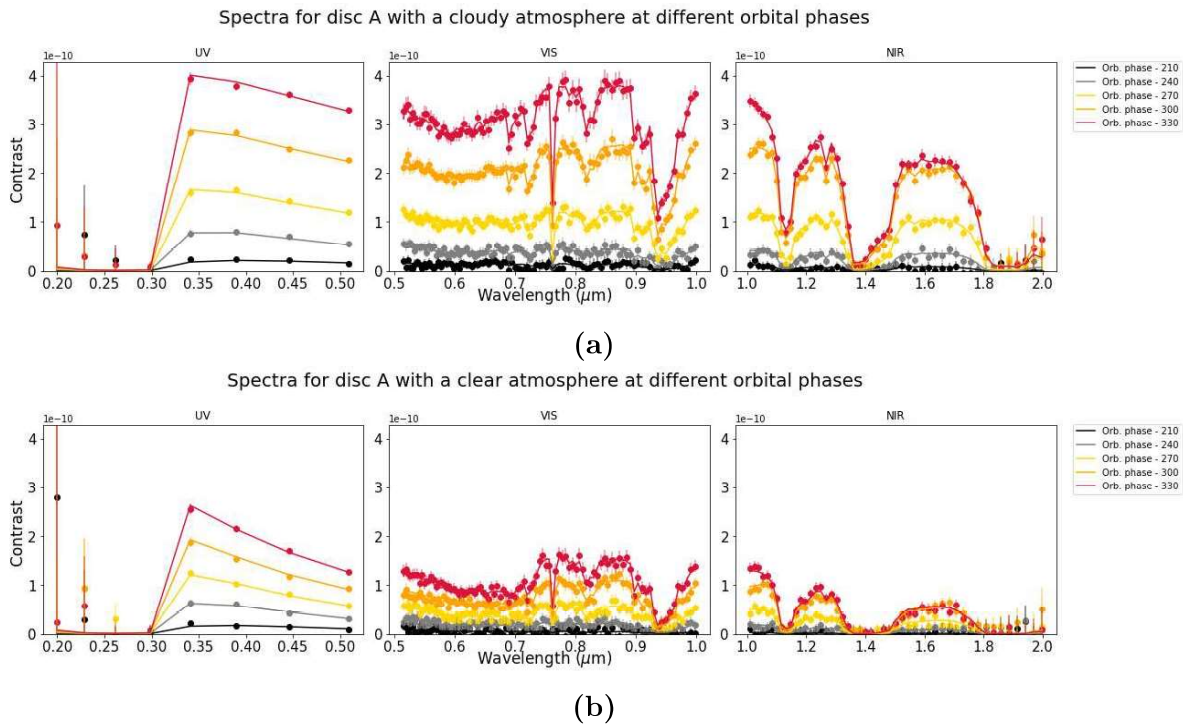
Figure 8.4: The reflectance spectra for a (a) cloudy atmosphere and (b) clear atmosphere for disc A. Each color labels a different orbital phase.

Figure 8.3 shows the illuminated portion of disc A (with rotational phase = 270) at different orbital phases. As the planet moves from its transit position (in front of the star) to its secondary eclipse position (behind the star), the fraction of the disc which is illuminated increases, and thus the amount of light reflected by the disc also increases. Figure 8.4 shows the reflectance spectra for disc A with a cloudy and clear atmosphere. With the increase in the illuminated portion of the disc with the orbital phase, the contrast throughout all three wavelength bands increases. Figure 8.5 shows the reflectance spectra for disc A with a cloudy atmosphere devoid of O_2, H_2O or O_3. Same as before, the contrast values increase with the orbital phase.

8.3   Comparing SNRs of atmospheric constituents

Figures 8.6, 8.7 and 8.8 depict the SNRs for disc A with a cloudy and a clear atmosphere for (a) O_2 in the visible band centered around 0.76μm, (b) H_2O in the near-infrared band and (c) O_3 in the uv band.

Figure 8.9 shows a comparison between the net SNRs of O_2 in the visible band, H_2O in the visible and near-infrared band and O_3 in the uv band for disc A with a cloudy and clear atmosphere. The net SNRs increase with the orbital phase for all gases as the fraction of the illuminated disc increases. Moreover, the enhancing effect of clouds is again evident at all orbital phases. In the presence of clouds, H_2O shows the highest detectability in the nir band followed by O_3 in the uv band at almost all orbital phases. The net SNRs of O_2 are relatively lower because it only has one prominent absorption line at $\sim 0.76\mu$m in the visible band which contributes to the net SNR. Figure 8.10 concisely depicts a comparison of the SNRs for all three gases.

The main takeaway from this section is that the SNRs are highly dependent on the position of the target planet in its orbit as it will determine the fraction of the illuminated disc w.r.t the observer and subsequently, the signal. It is beneficial if the planet is observed at a higher orbital phase when it is close to its host star on the sky plane as this position leads to the highest SNRs. However, it is possible that at higher orbital phases, the planet goes inside the inner working angle of the coronagraph and hence cannot be observed. Hence, there is an optimal orbital phase for practical observations at which all the gases give high SNRs. As anticipated, clouds enhance these SNRs at all orbital phases and improve the detectability of all the gases considered above.

(a)

(b)

(c)
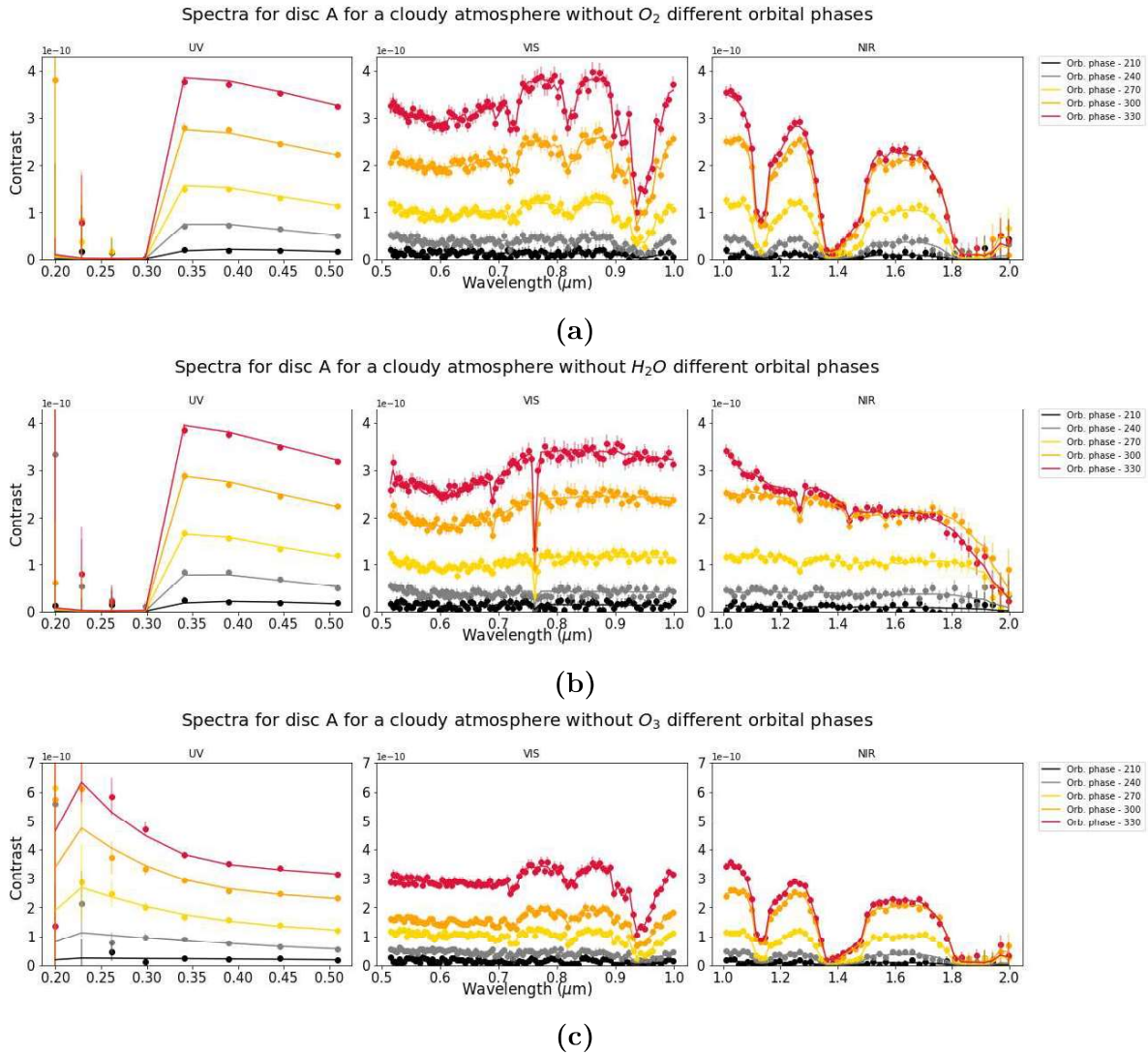
Figure 8.5: The reflectance spectra for disc A with a cloudy atmosphere devoid of (a) O_2, H_2O and (c) O_3. Each color labels a different orbital phase.

SNRs for O_2 at different orbital phases for disc A with a cloudy atmosphere

(a)

SNRs for O_2 at different orbital phases for disc A with a clear atmosphere

(b)
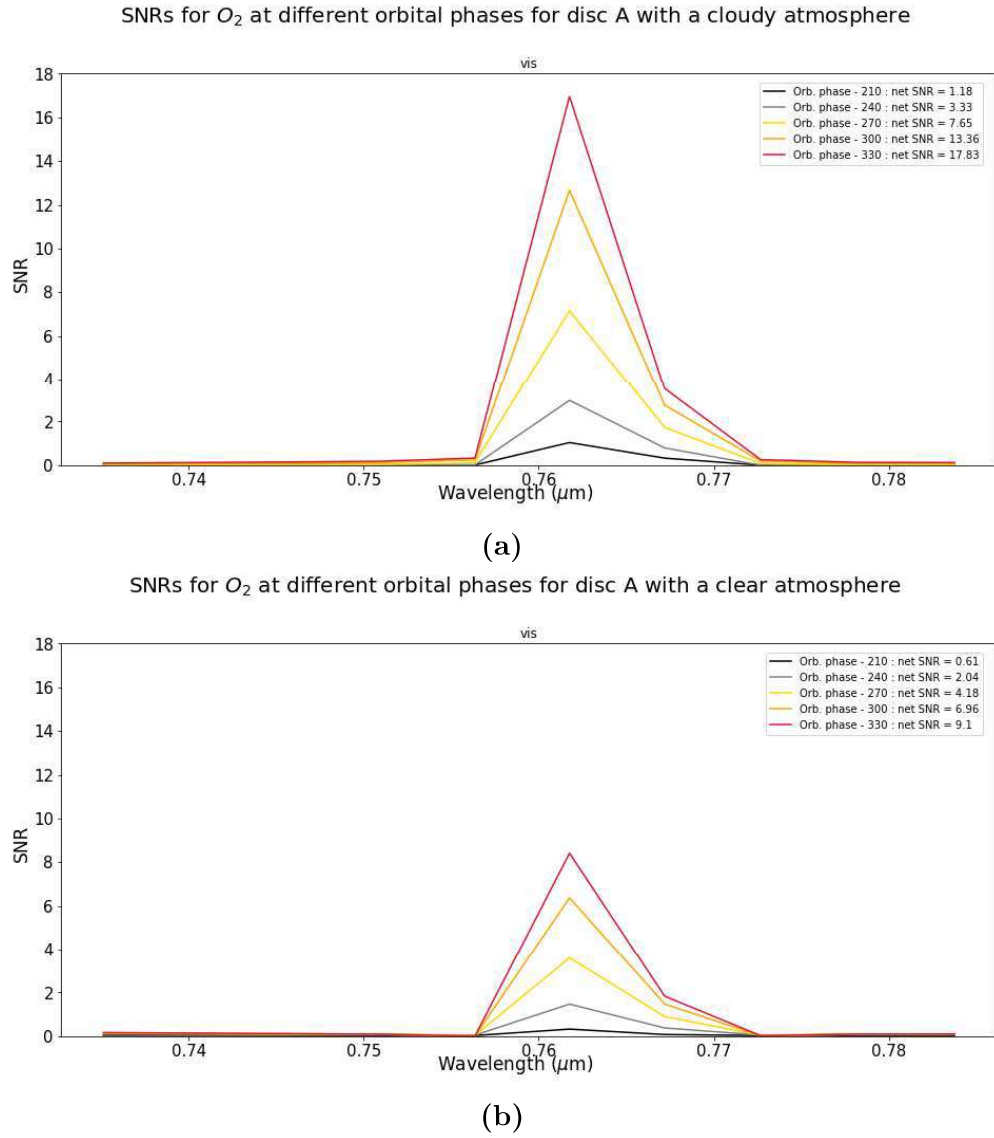
Figure 8.6: The SNRs that quantify the detectability of O_2 in the visible band for a (a) cloudy and (b) clear atmosphere for disc A. The plot is centered around 0.76μm where O_2 shows its most prominent absorption line. The net SNR value at each orbital phase is given in the legend.

SNRs for H_2O at different orbital phases for disc A with a cloudy atmosphere

(a)

SNRs for H_2O at different orbital phases for disc A with a clear atmosphere

(b)
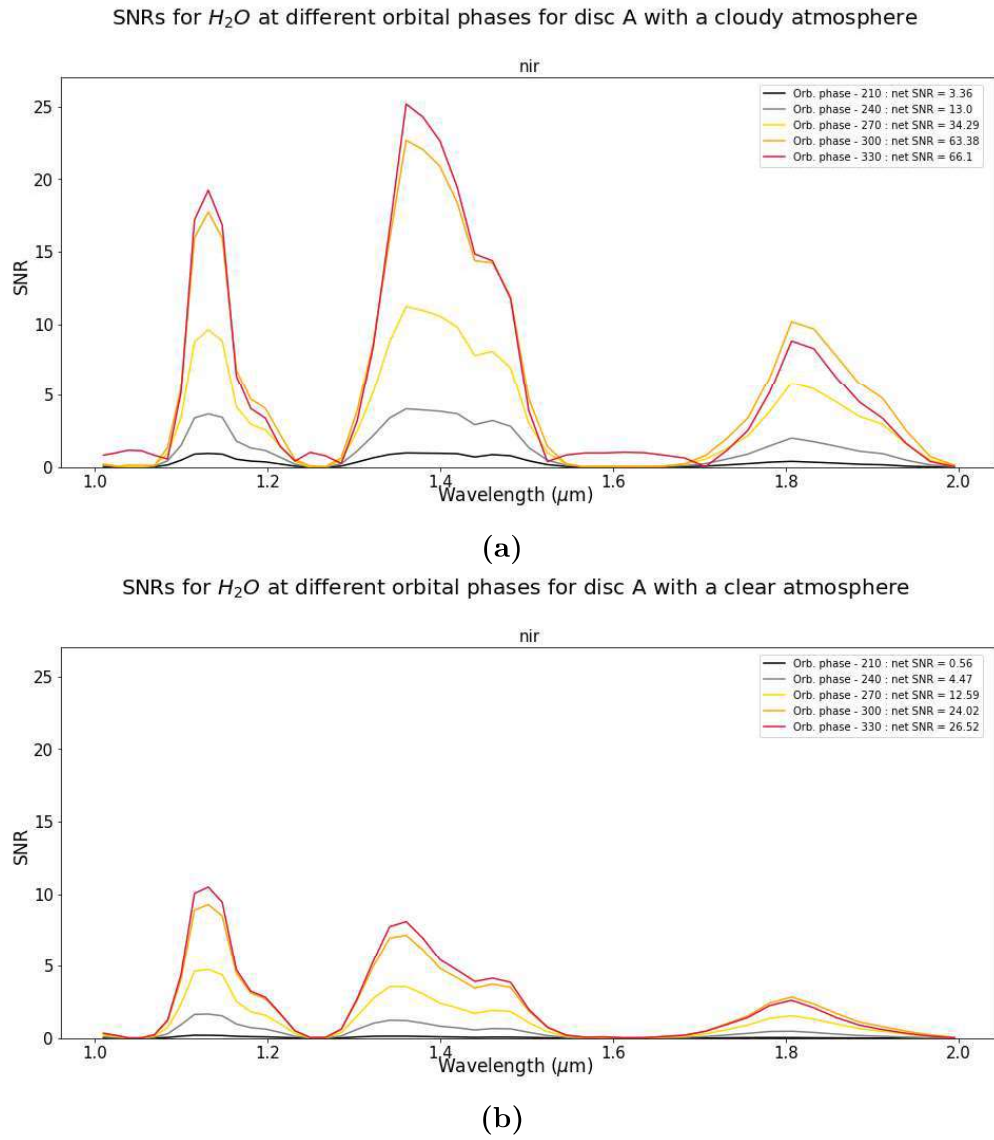
Figure 8.7: The SNRs that quantify the detectability of H_2O in the near-infrared band for a (a) cloudy and a (b) clear atmosphere for disc A. The net SNR value at each orbital phase is given in the legend.

SNRs for O_3 at different orbital phases for disc A with a cloudy atmosphere

(a)

SNRs for O_3 at different orbital phases for disc A with a clear atmosphere

(b)
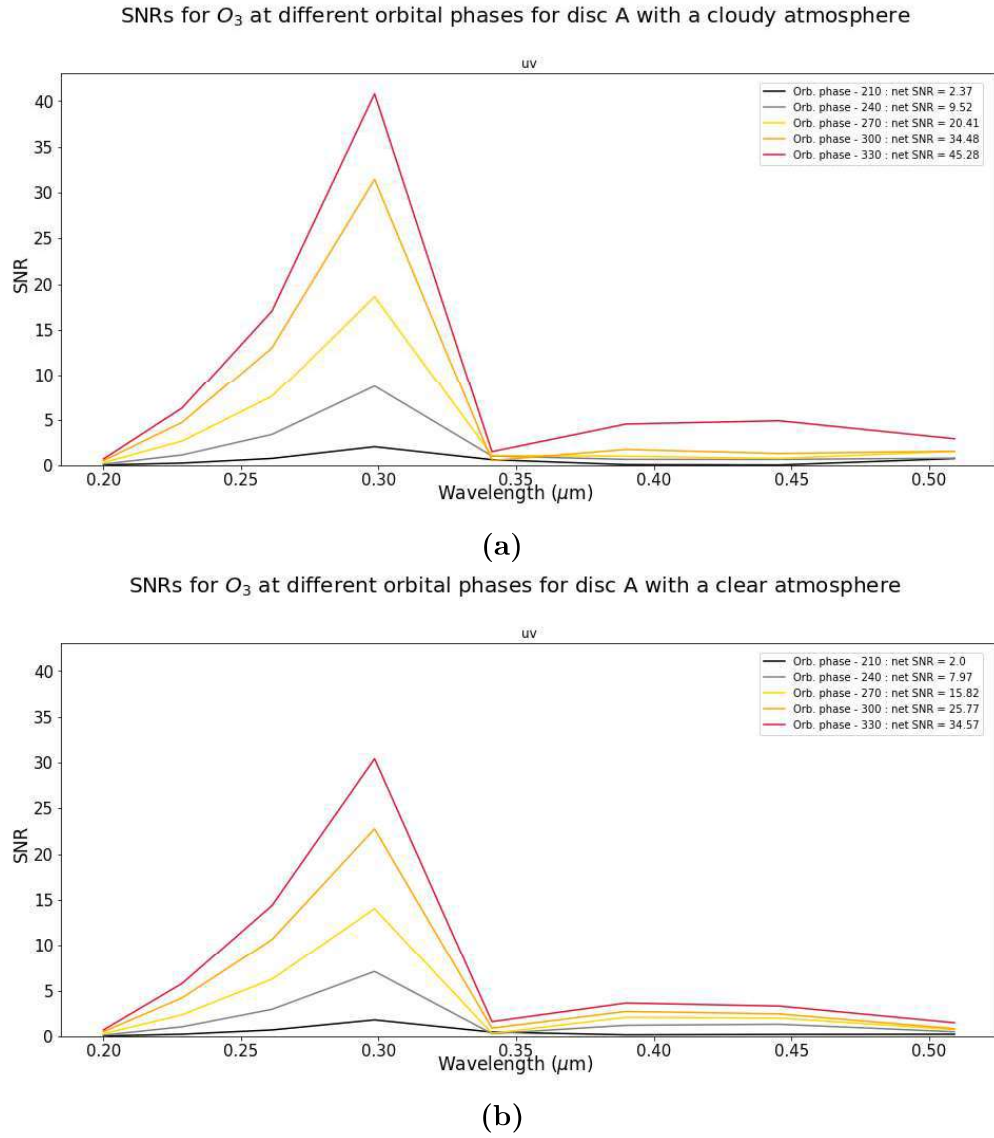
Figure 8.8: The SNRs that quantify the detectability of O_3 in the uv band for a (a) cloudy and (b) clear atmosphere for disc A. The net SNR value at each orbital phase is given in the legend.

(a)   (b)
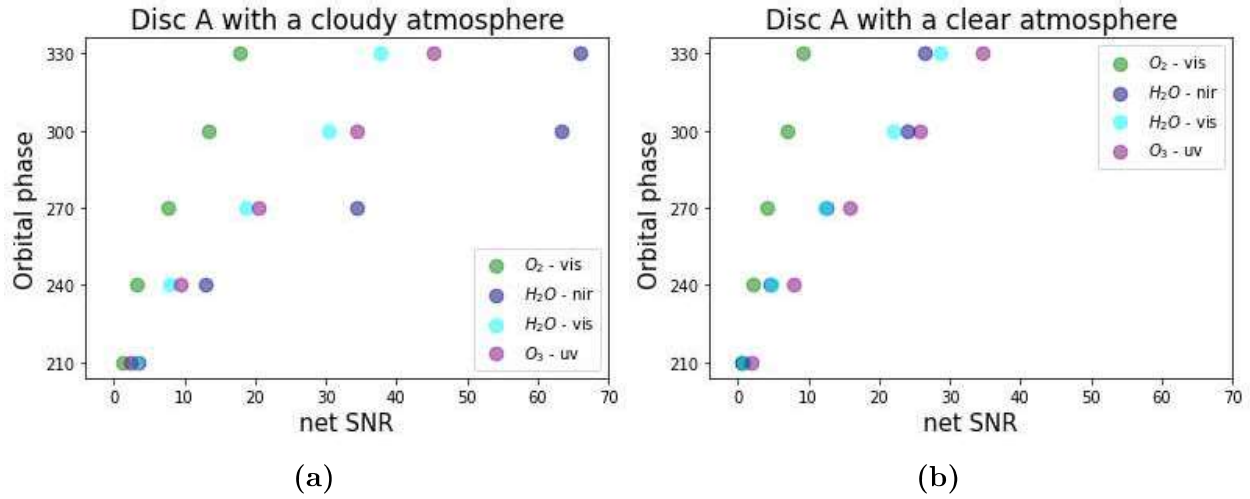
Figure 8.9: A comparison of the net SNRs of O_2 in the visible band, H_2O in the visible and near-infrared band and O_3 in the uv band for disc A with a (a) cloudy and (b) clear atmosphere.
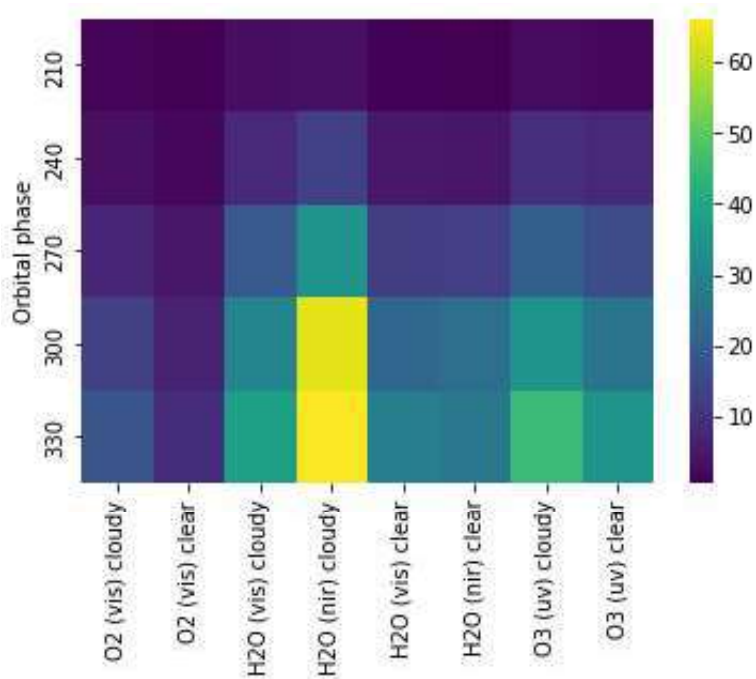
Figure 8.10: A comparison of the net SNRs for all the three gases, O_2, H_2O and O_3 in the corresponding wavelength bands as shown in the bracket for disc A with a clear and a cloudy atmosphere. The orbital phase of the disc is plotted along the y-axis.

Chapter 9

Impact of naturally varying cloud cover on the characterization of the remote Earth atmosphere

We have seen previously that clouds have a significant impact on the characterization of the atmosphere of our remote Earth. They (i) increase the albedo of the planet and lead to a higher continuum in the reflected light spectrum and (ii) enhance the SNRs of atmospheric constituents and thus improve their detectability. However, until now we have only compared cases where clouds are either explicitly present or absent in the atmosphere. In this section, we compare the effects of varying cloud coverage on the spectrum as well as on the detectability of gases.

9.1   Variation in cloud abundance from the ISCCP data

Since we are using atmospheric data from Earth as the basis of our remote Earth model, we go through this data to identify trends regarding variation in cloud coverage. We use two datasets for this purpose, the ISSCP dataset and data from the MERRA-2 model. The ISSCP dataset gives the fraction of cloud cover over a 2d grid while data from the MERRA-2 model gives the cloud mass fraction over a 3d grid. Since these two datasets use different proxies for identifying and quantifying cloud over, it is difficult to correlate the two, as explained in a later section as well.

The ISCCP data is more intuitive since it is projected on a 2d grid, and it can be simply interpreted as how cloudy a planet would look if observed from outer space. Let's look at some of the trends in cloud coverage as derived from the ISSCP data. Figure 9.1a shows how the cloud cover varies across a day for the three days given in the legend. The y-axis depicts a global spatial average of the ISCCP data over a 2d grid, and this value can be interpreted as the fraction of the Earth's disc that is covered with clouds. In addition to the total cloud cover being different, the diurnal trend is also dissimilar for these three days. Figure 9.1b depicts the evolution of the cloud cover over a month for the three months of May, June, and July in the year 2000. Similarly figure 9.2a shows how the cloud cover varies over a year for the four years mentioned in the label. Figure 9.2b depicts a boxplot of the trend in cloud cover across 1984-1993. The months with a lot of outliers like May, June, and November show significant variation in cloud cover over the span of 10 years while months like August or September show little variation.

| (a) | (b) |
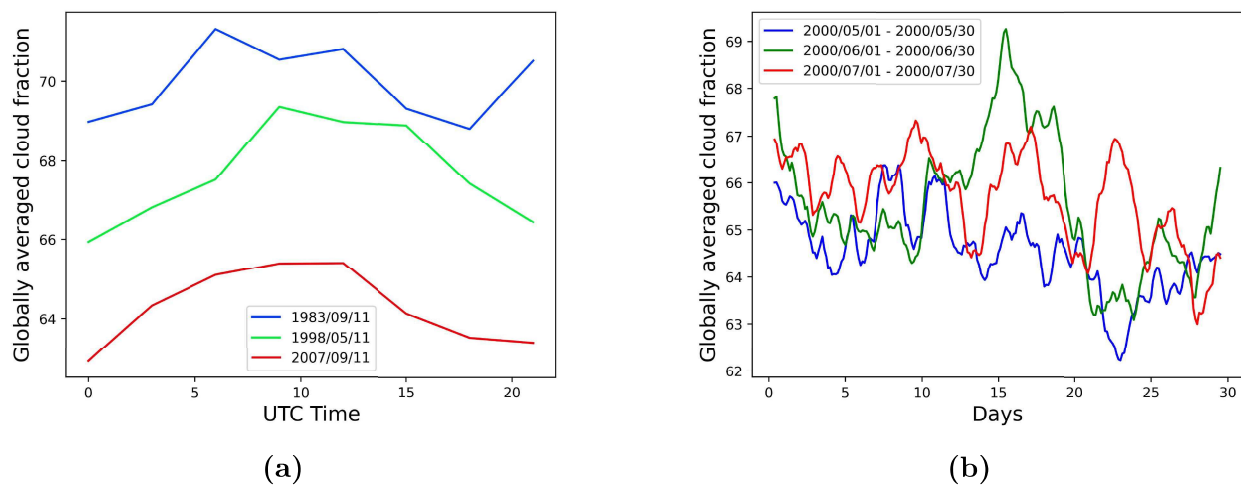
Figure 9.1: Evolution of the globally averaged cloud fraction over (a) a day for the three days given in the legend (format:yy/mm/dd) (b) a month for three months May, June, and July in the year 2000. The monthly variation corresponds to a rolling average and thus all the diurnal variations are averaged out.

9.2   Variation in cloud abundance from the MERRA-2 data

Even though we can identify trends in cloud cover using the ISCCP data, our remote Earth model atmosphere is constructed using the MERRA-2 data. Thus, we tried to correlate

the data obtained from these two different datasets, but we came to the conclusion that no such correlation is possible because these two datasets use completely different proxies for identifying and quantifying cloud cover. ISCCP classifies individual pixels as clear or cloudy based on the intensity detected by each pixel (Rossow and Schiffer, 1999) while the MERRA-2 model computes the cloud mass fraction on a 3d grid. Thus, even though the ISCCP data is more intuitive, we cannot correlate it with the MERRA-2 data, and going forward, we only use the MERRA-2 data to compute variations in cloud cover.

(a)

(b)
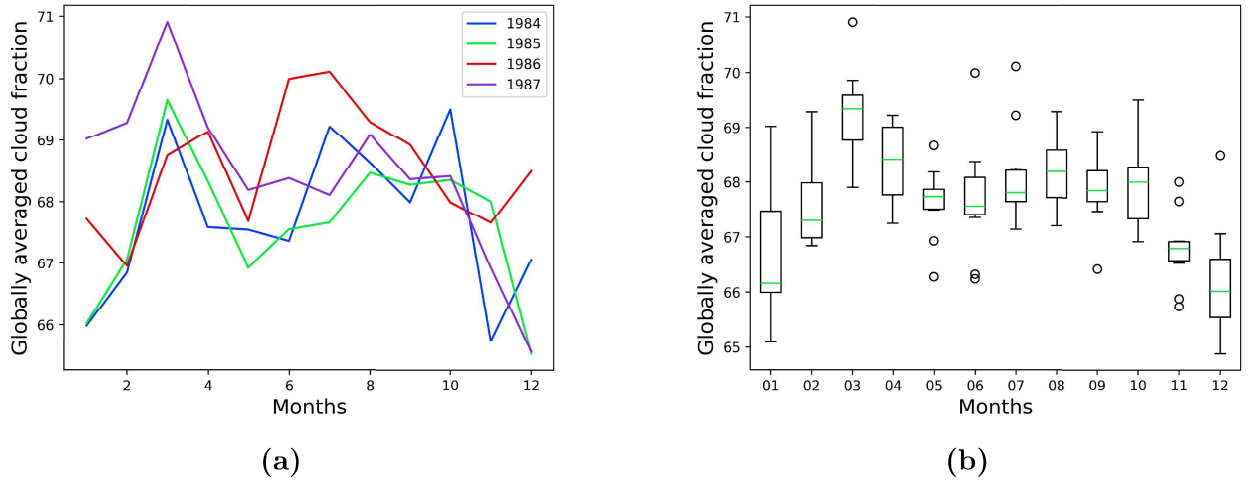
Figure 9.2: (a) Evolution of the globally averaged cloud fraction over a year for the four years given in the legend. Each data point corresponds to a monthly average. (b) A boxplot depicting the trend in the evolution of cloud cover over the years 1984-1993. There are 10 data points for each month which correspond to the monthly average for that month across the 10 years. The box extends from the first (Q1) to the third quartile (Q3), the whiskers extend from Q1 - 1.5IQR to Q3 + 1.5IQR[1], and the dots are the outliers.

The MERRA-2 model gives the cloud mass fraction (in kg/kg) over a 3d grid and using this we compute the total mass of clouds (in kg) over all gridded columns. First, we compute the liquid water path (in kg/m^2) for one column as

$$\mathrm{LWP} = \int_{\mathrm{P_s}}^{0} \mathrm{M_c} \, \frac{\mathrm{dP}}{\mathrm{g}} \qquad (9.1)$$

where $\mathrm{P_s}$ is the surface pressure, $\mathrm{M_c}$ is the cloud mass fraction in a layer and g is the

---

[1]IQR: Inter-quartile range = Q3-Q1

acceleration due to gravity. The area of a grid centered around latitude λ and longitude ϕ is

$$A = r^2 cos(\lambda) d\lambda d\phi \tag{9.2}$$

where r is the radius of the Earth. The product of the liquid water path and the area of the column gives the total mass of clouds (in kg) in that column. Taking a spatial average of this cloud mass over all the grids gives the globally averaged cloud mass content, and we use this quantity as our proxy for cloud cover. Given this proxy, we go through the MERRA-2 data spanning 16 years from 1984-2000 and try to identify the periods when the Earth was the most or the least cloudy. Figure 9.3a shows how the globally averaged cloud amount evolves across this 16-year span. From this, we identify the most and the least cloudy months and the variation of the cloud amount across these is shown in figure 9.3b. These turn out to be July of 1999 and February of 1987 respectively. To digress a bit here, 1987 and 1999 correspond to strong El Nino and La Nina events respectively (https://ggweather.com/enso/oni.htm), and there have been many studies analyzing the effects of ENSO events on cloud coverage (Radley et al., 2014; Sahu et al., 2022; Yang et al., 2016). Subsequently, we identify the most cloudy day from July 1999 and the least cloudy day from February 1987 - 7th of July and 15th of February. At the end of this exercise, we have the days on which the Earth was the most and the least cloudy throughout this 16-year span, and now we can construct our remote Earth model using MERRA-2 atmospheric data from these two days.

(a)   (b)
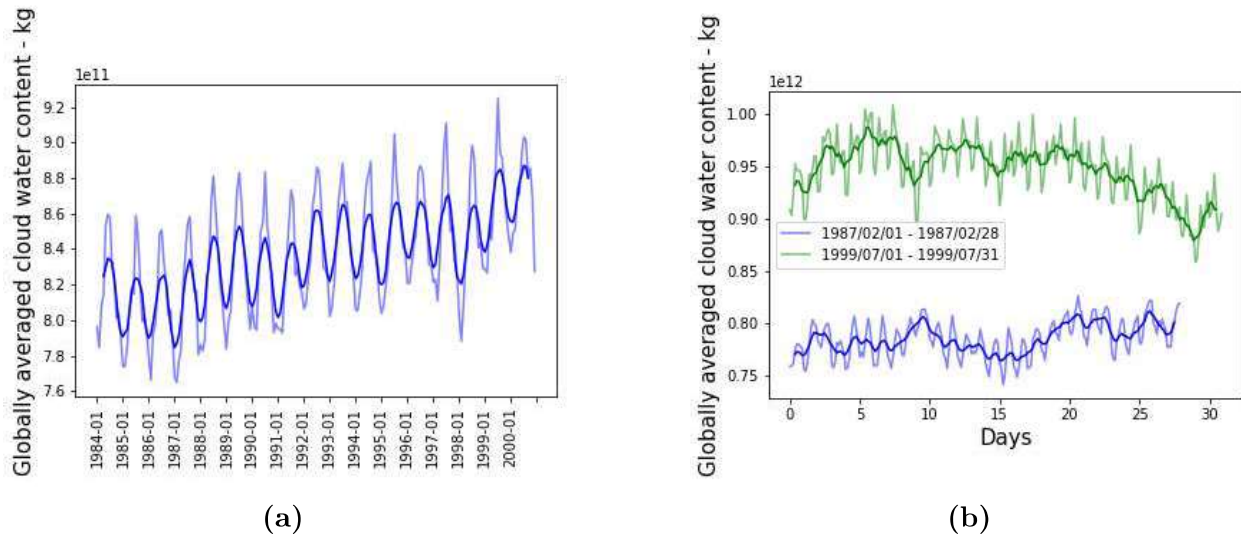
Figure 9.3: (a) Evolution of the globally averaged cloud amount across 16 years. The dark line corresponds to the rolling average. (b) Variation in cloud cover across the most and the least cloudy months across the 16-year span.

9.3   Impacts of high/low cloud cover on the spectrum

Now that we have identified the two days when the Earth was the most and least cloudy we can compare how the amount of cloud coverage impacts the spectrum and the detectability of gases. Figure 9.4 compares the spectra of discs A and B for atmospheres with high and low cloud coverage. The continuum in the reflected light spectrum will depend upon the amount of clouds and how they are distributed over that disc. For disc A, the continuum is significantly higher for an atmosphere with high cloud coverage while for disc B, the continuum for the two cases is similar. Figure B.6 shows the reflectance spectra of a rotating remote Earth for an atmosphere with high/low cloud coverage for all the eight configurations.
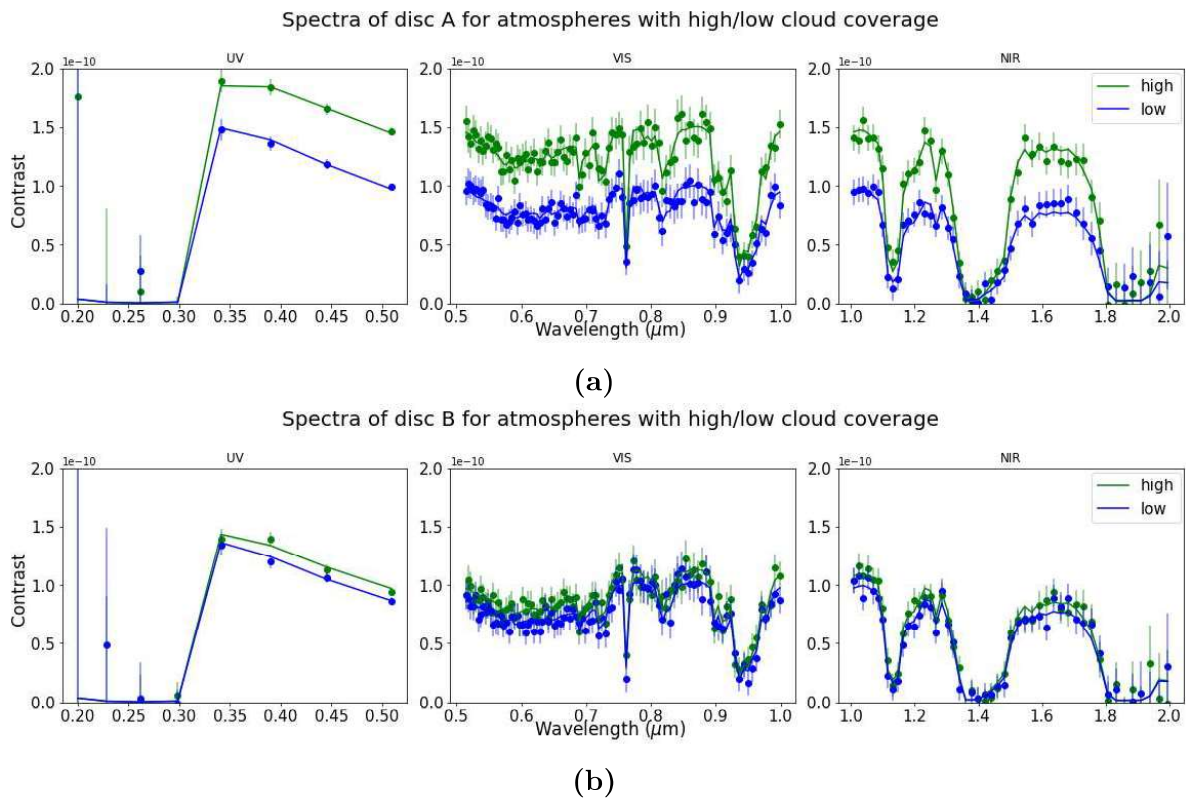
Figure 9.4: Comparison of spectra for (a) disc A and (b) disc B for atmosphere with high and low cloud coverage.

9.4   Impacts of high/low cloud coverage on the SNRs

Let's consider the effect of cloud coverage on the detectability of gases. Since the amount of clouds has a significant effect on the spectra of disc A, we restrict our analysis to disc A. Figure 9.5 compares the SNRs for (a) O_2 in the visible band centered around $0.76\mu m$, (b) H_2O in the near-infrared band and (c) O_3 in the uv band for atmospheres with high/low cloud coverage. It is evident that the SNRs are enhanced when the cloud coverage is high. The insets show how the net SNRs evolve with rotational phase. Figure B.7 in Appendix B compares the wavelength-dependent SNRs for atmospheres with high, low, and no cloud coverage for disc A, and figure 9.6 shows the net SNRs for all the three gases at all rotational phases. As expected, the atmosphere with high cloud coverage shows the highest SNRs followed by the atmosphere with low cloud coverage and then the clear atmosphere.

The main takeaway from this section is that the amount of cloud cover in the planet's atmosphere can also significantly impact the detectability of important atmospheric constituents. This means that any abundance of a gas inferred from the planet's spectrum is an apparent abundance, in the sense that it varies with the amount of cloud cover over the disc. Thus, there seems to be a degeneracy between the true abundance of a molecule (defined in terms of the mixing ratio) and the amount of cloud cover. For example, a planet with a high abundance of let's say O_2 but low cloud cover might give the same SNR as a planet with low abundance of O_2 but high cloud cover. This is a slightly worrying prospect because this degeneracy means that interpreting the true abundance of any molecule from an observed spectrum is difficult. To remove this degeneracy, the observed spectrum should be compared with various retrieval models which is a computationally expensive task.

(a)

(b)

(c)
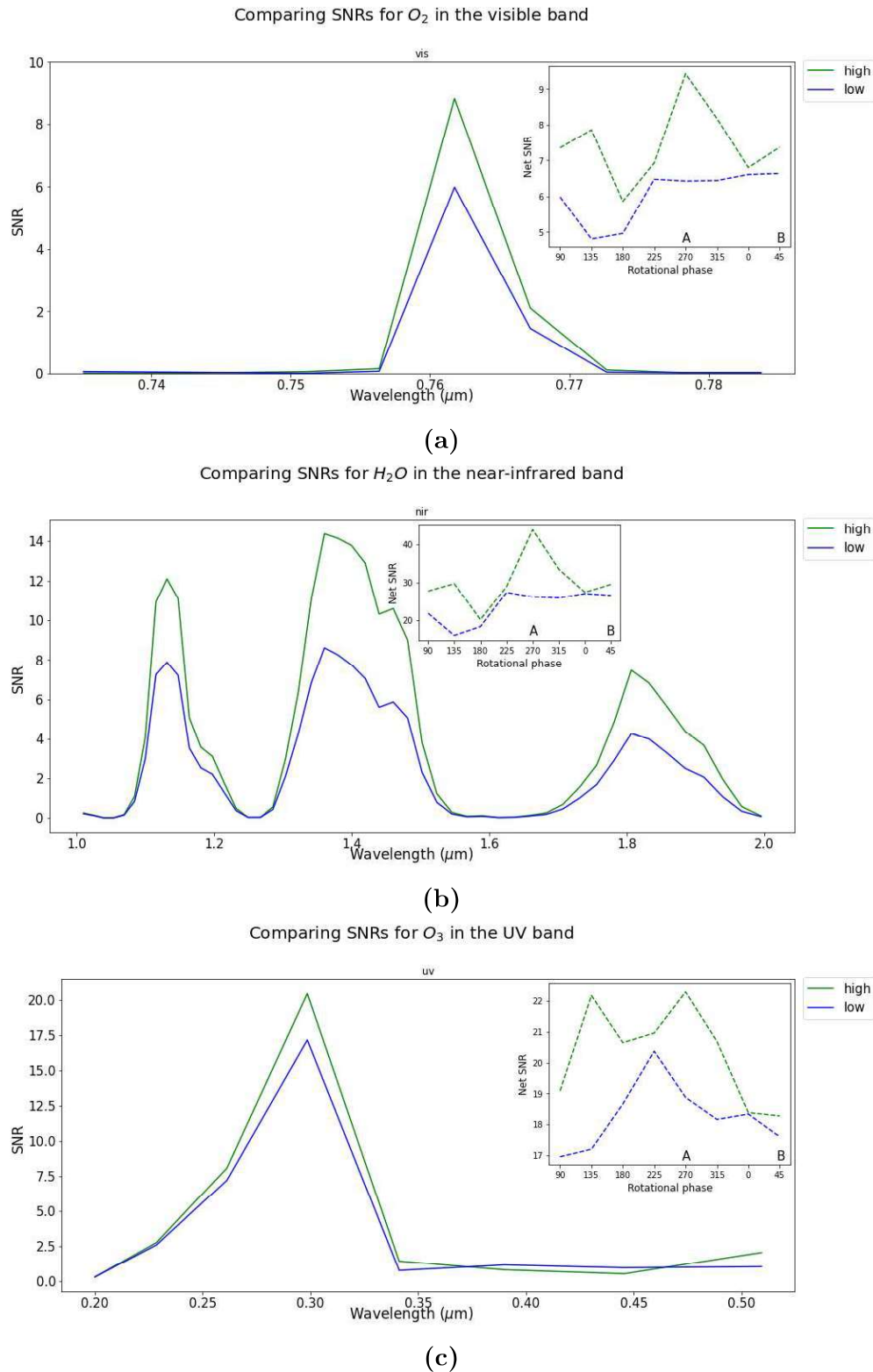
Figure 9.5: The wavelength-dependent SNRs for (a) O_2 in the visible band centered around 0.76μm, (b) H_2O in the near-infrared band and (c) O_3 in the uv band for atmospheres with high/low cloud coverage. The insets show how the net SNRs evolve with rotational phase.
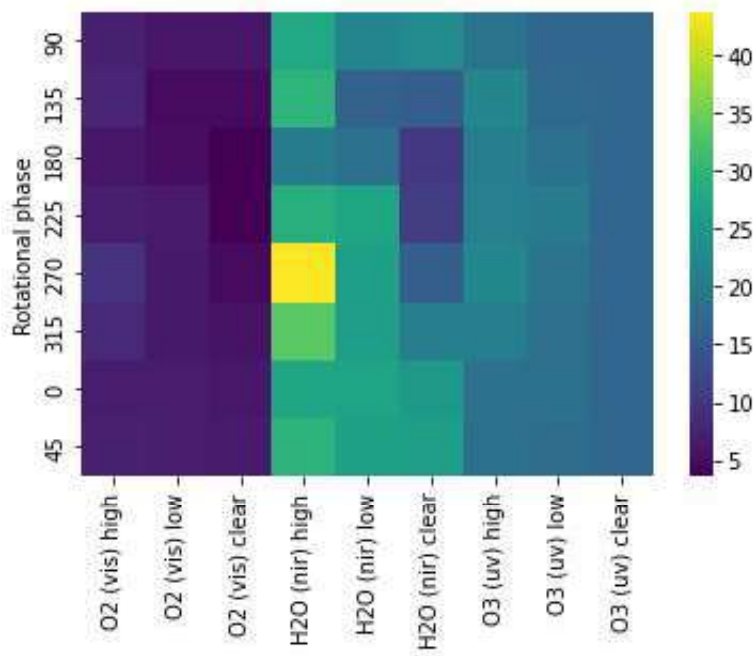
Figure 9.6: A comparison of the net SNRs for all the three gases, O_2, H_2O and O_3 in the corresponding wavelength bands as shown in the bracket and for atmospheres with high, low and no cloud coverage. The rotational phase of the disc is plotted along the y-axis.

Chapter 10

Leading up to the Habitable Worlds Observatory (HWO)

All our observations so far have been simulated using the LUVOIR-A mission concept, which is a direct-imaging space observatory concept. It has a 15m wide mirror (for reference JWST has a 6.5m wide mirror) and a coronagraph to block out light from the host star. However, it is very unlikely that a mission with such a big mirror size will ever get funded, and we have to turn to more practical mission concepts like the LUVOIR-B (8m), Habex/SS (4m) or the Habitable Worlds Observatory (6m). Before we evaluate the performance of these mission concepts, let's take a look at their instrumental properties.

10.1   Comparing different mission concept parameters

Table 10.1 describes all the relevant instrumental parameters for all the four mission concepts. The main difference between all four of these is the primary mirror size which determines the collecting area of the instrument.

Parameter	LUVOIR-A	LUVOIR-B	Habex/SS	HWO
Diameter	15m	8m	4m	6m
Spectral range	UV: 0.2 - 0.515 μm VIS: 0.515 - 1 μm NIR: 1 - 2 μm	UV: 0.2 - 0.515 μm VIS: 0.515 - 1 μm NIR: 1 - 2 μm	UV: 0.2 - 0.45μm VIS: 0.45 - 0.975μm NIR: 0.975 - 1.8μm	UV: 0.2 - 0.515 μm VIS: 0.515 - 1 μm NIR: 1 - 2 μm
Resolution	UV: 7 RP VIS: 140 RP NIR: 70 RP	UV: 7 RP VIS: 140 RP NIR: 70 RP	UV: 7 RP VIS: 140 RP NIR: 40 RP	UV: 7 RP VIS: 140 RP NIR: 70 RP
Exozodi level[a]	4.5	4.5	4.5	4.5
Contrast	1×10^{-10}	1×10^{-10}	1×10^{-10}	1×10^{-10}
IWA	4 λ/D	3.5 λ/D	UV: 39 mas VIS: 58 mas NIR: 104 mas	3.5 λ/D
Read noise	UV: 0 VIS: 0 NIR: 2.5	UV: 0 VIS: 0 NIR: 2.5	UV: 0.008 VIS: 0.008 NIR: 0.32	UV: 0 VIS: 0 NIR: 2.5
Dark noise	UV: 3×10^{-5} VIS: 3×10^{-5} NIR: 0.002	UV: 3×10^{-5} VIS: 3×10^{-5} NIR: 0.002	UV: 3×10^{-5} VIS: 3×10^{-5} NIR: 0.005	UV: 3×10^{-5} VIS: 3×10^{-5} NIR: 0.002

Table 10.1: The parameters that describe the instrumental configuration for the four mission concepts, LUVOIR A/B, Habex, and HWO. Parameter values adapted from Checlair et al., 2021.

Figure 10.1 shows the planetary and optical throughputs for all the mission concepts. The throughputs for HWO are assumed to be the same as LUVOIR-B.

(a) **(b)**
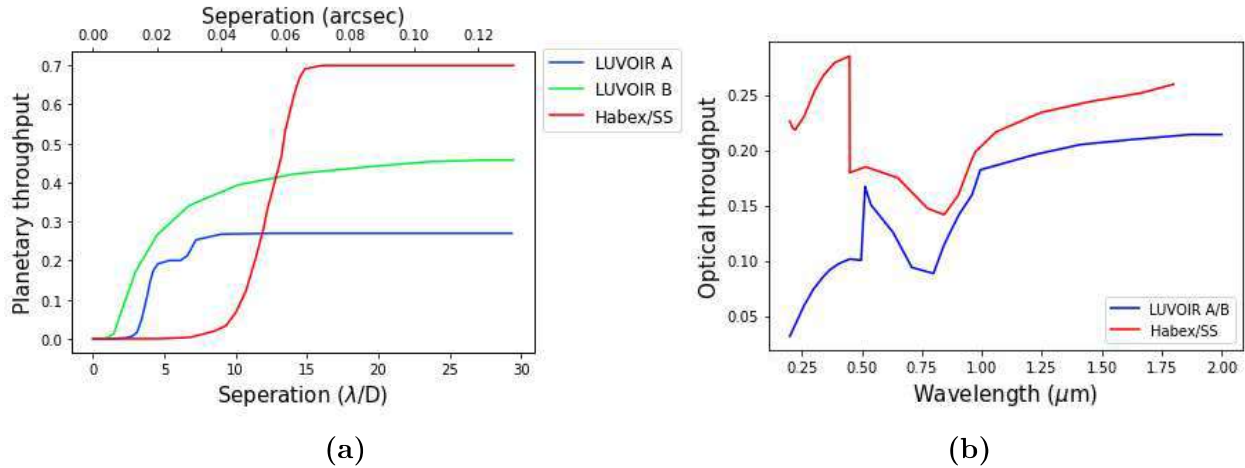
Figure 10.1: The (a) planetary throughput as a function of separation and the (b) optical throughput as a function of wavelength for the different mission concepts.

10.2 Comparing spectra simulated with different mission concepts

Consider the same two discs A and B for a remote Earth on the most cloudy day. Figure 10.2 shows the reflectance spectra for discs A and B for an atmosphere with high cloud coverage simulated using (a) LUVOIR A (15m), (b) LUVOIR B (8m), (c) HWO (6m) and (d) Habex/SS (4m). It is evident that as the mirror size and hence the collecting area reduces, the scatter in the noise increases. Thus it becomes difficult to distinguish between different rotational phases of the planet. Animations of the spectra of a rotating remote Earth as simulated using all the mission concepts can be seen here.

Let's compare how all these mission concepts perform when trying to detect atmospheric constituents. Since our target is the same, the main instrumental factors affecting the SNRs are the collecting area of the mirror, the planetary and optical throughput and detector noises like the read noise and dark noise. Figure 10.3 shows how the SNRs for all three gases compare when the planet is observed with the four mission concepts. LUVOIR-A gives the highest SNRs for all three gases since it has the biggest mirror size. However, the SNRs do not simply scale with the mirror size. Habex with the smallest mirror size (4m) gives higher

SNRs than HWO (6m) for H_2O in the near-infrared band and higher SNRs than HWO and LUVOIR-B (8m) for O_3 in the uv band. This can be attributed to a variety of factors - (i) Habex has the highest planetary and stellar throughput out of all the mission concepts and (ii) it has a much lower read noise component in the nir. Figure B.8 in Appendix B shows a similar plot comparing the SNRs for disc A with an atmosphere with low cloud coverage.

Considering an atmosphere with high cloud coverage, only LUVOIR-A has the capability to give individual SNRs > 5 for O_2 and H_2O with an exposure time of 3 hours. Thus, only LUVOIR-A can provide a confirmed detection of these gases in 3 hours, the rest of the mission concepts will need a longer exposure time to go beyond the golden standard of SNR=5. Since O_3 has such a strong absorption signal in the uv band, all these mission concepts give SNRs > 5 and all of them can provide a confirmed detection of O_3 with an exposure time of 3 hours.

Moving on, let's compare the evolution of the net SNRs with rotational phase for atmospheres with high and low cloud coverage as observed with the four mission concepts. Figures 10.4, 10.5 and 10.6 show this comparison for O_2, H_2O and O_3 respectively. It seems that the trend in the SNRs remains the same, only the values are scaled for the different mission concepts. For detecting O_2 and H_2O, LUVOIR-A outperforms all the other instruments by a huge margin while for detecting O_3, Habes/SS is similarly capable. Figure 10.7 shows a concise comparison of the net SNRs of all the three gases for atmospheres with low and high cloud coverage as observed with different mission concepts.
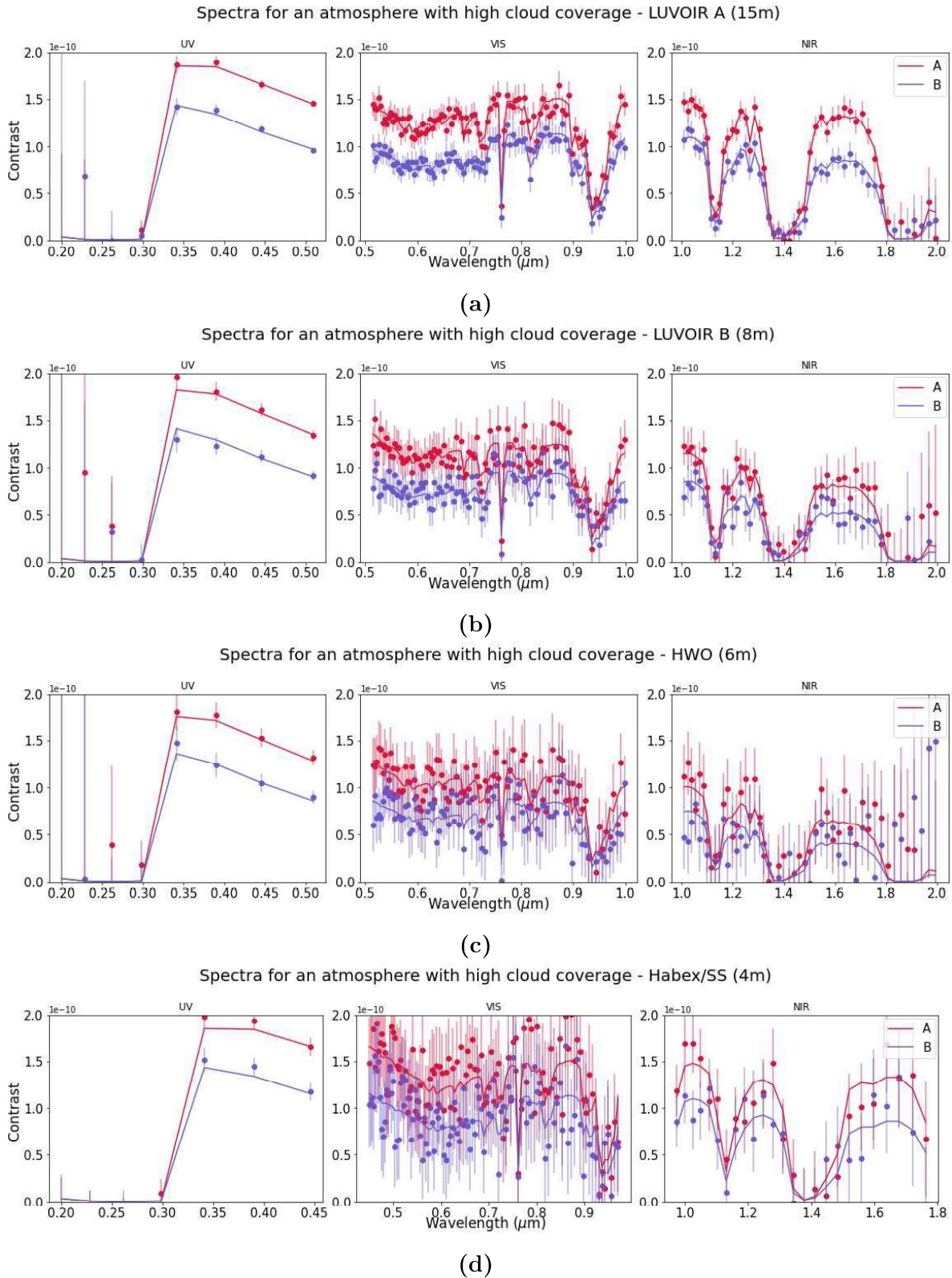
Figure 10.2: Reflectance spectra for discs A and B for an atmosphere with high cloud coverage simulated using (a) LUVOIR A (15m), (b) LUVOIR B (8m), (c) HWO (6m) and (d) Habex/SS (4m).

Comparing SNRs for O_2 in the visible band for disc A

(a)

Comparing SNRs for H_2O in the near-infrared band for disc A

(b)

Comparing SNRs for O_3 in the uv band for disc A

(c)
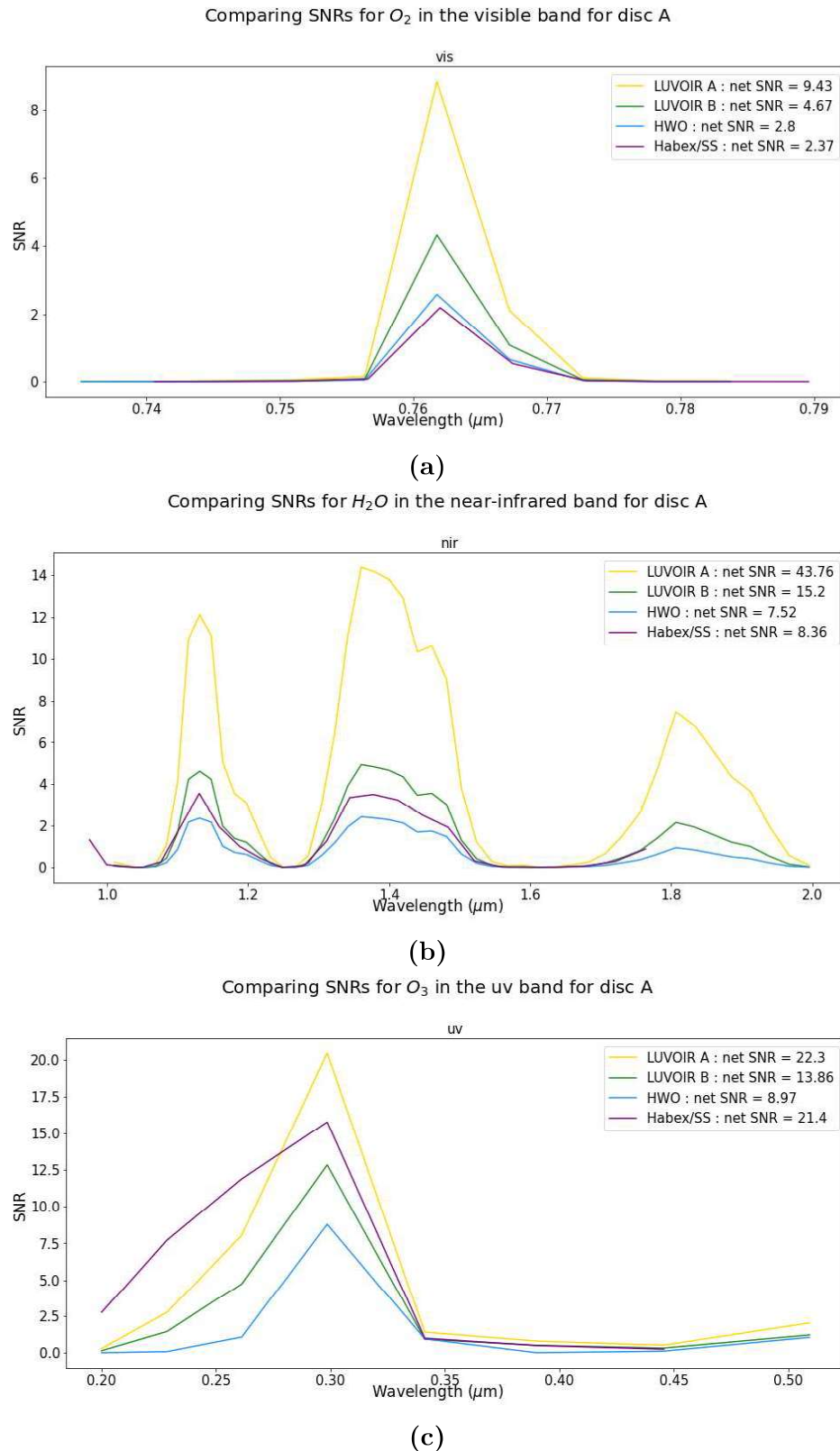
Figure 10.3: The wavelength-dependent SNRs for (a) O_2 in the visible band centered around 0.76μm, (b) H_2O in the near-infrared band and (c) O_3 in the uv band for disc A with an atmosphere with high cloud coverage. The net SNRs for the entire wavelength band are given in the legend.
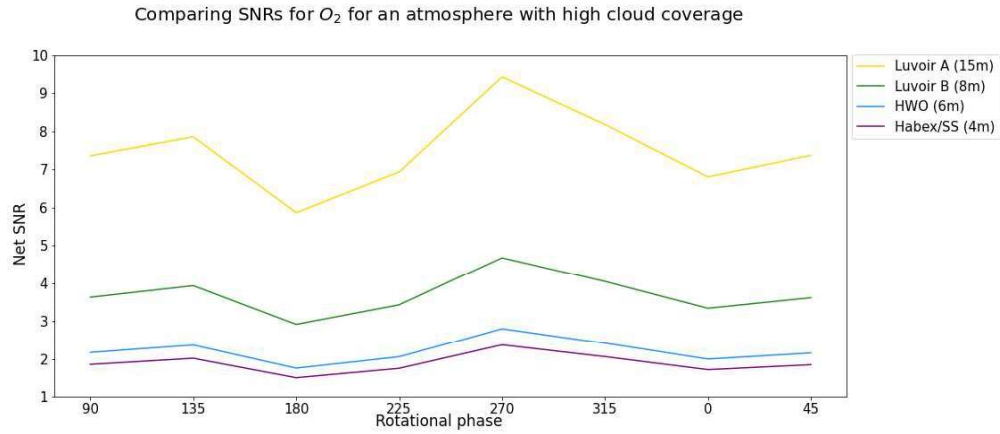
(a)
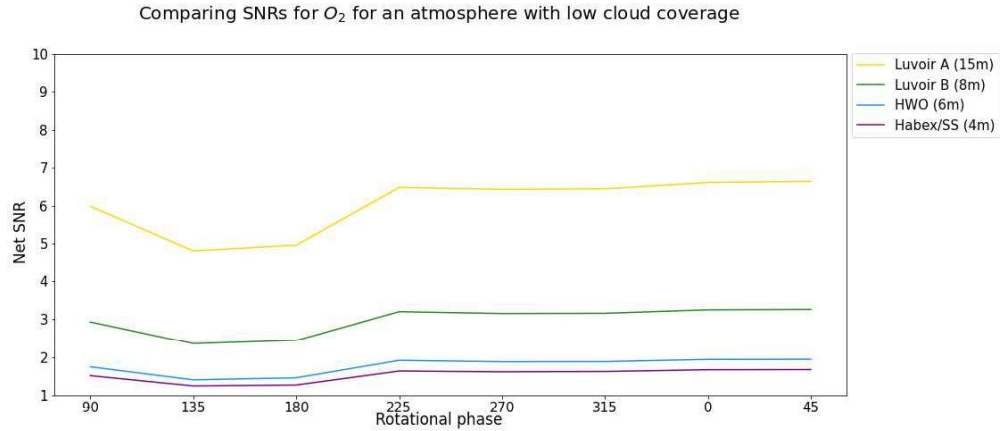
(b)

Figure 10.4: Evolution of the net SNRs with rotational phase for O_2 in the visible band with an atmosphere with (a) high and (b) low cloud coverage as observed by different mission concepts.
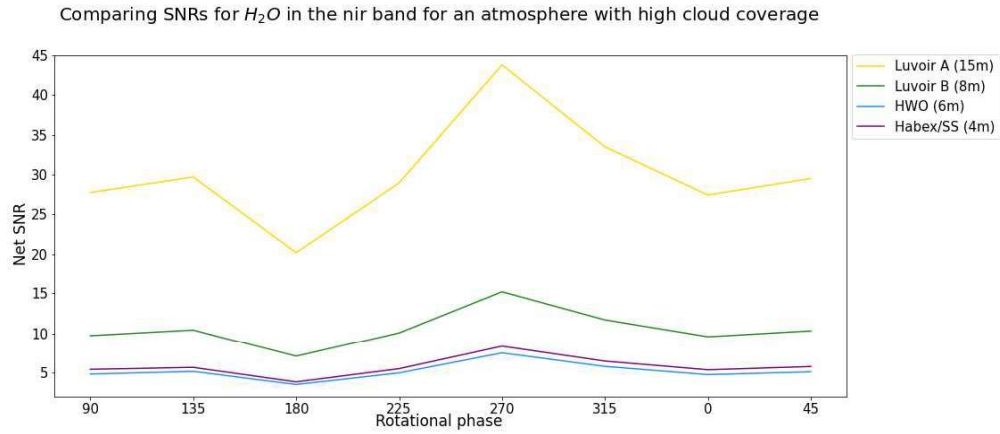
(a)
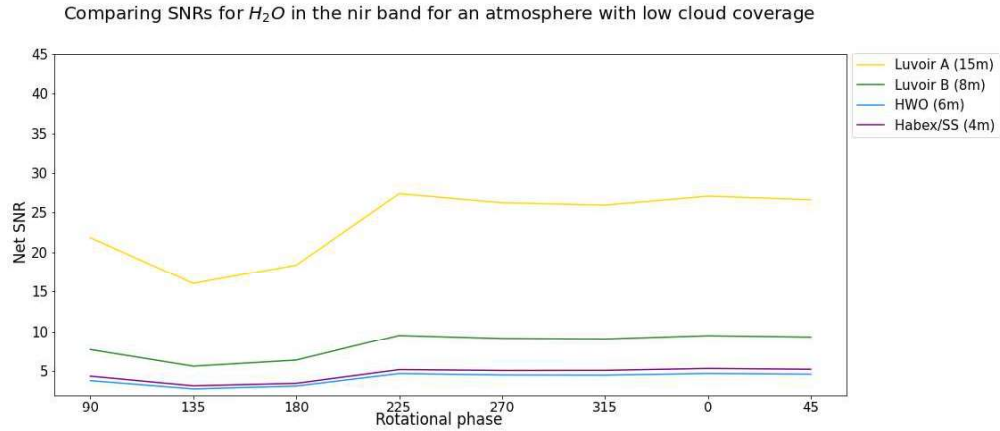
(b)

Figure 10.5: Evolution of the net SNRs with rotational phase for H_2O in the nir band with an atmosphere with (a) high and (b) low cloud coverage as observed by different mission concepts.
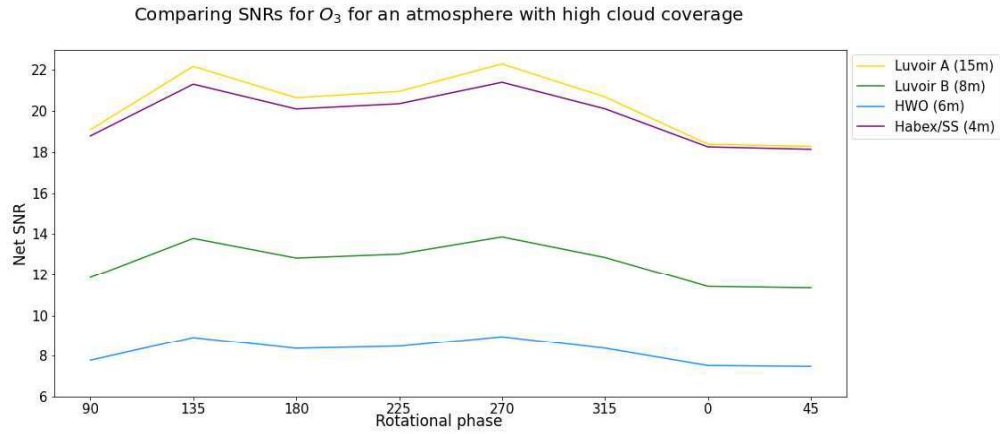
(a)
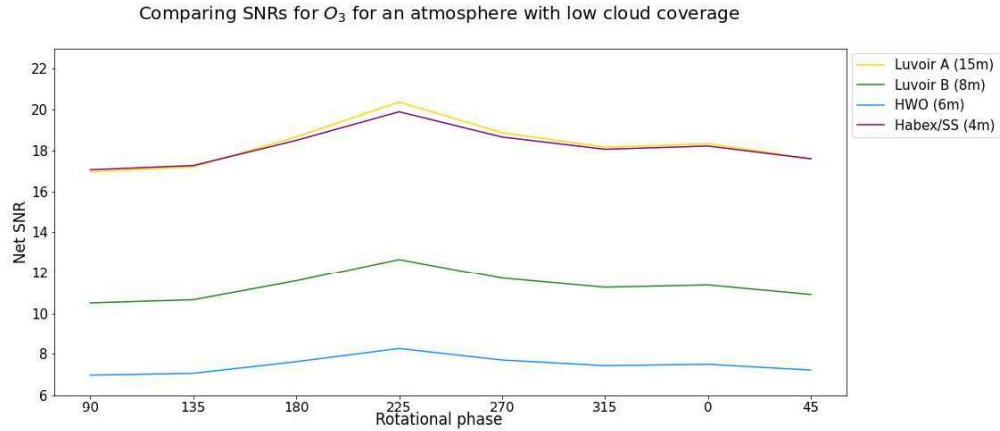
(b)

Figure 10.6: Evolution of the net SNRs with rotational phase for O_3 in the uv band with an atmosphere with (a) high and (b) low cloud coverage as observed by different mission concepts.
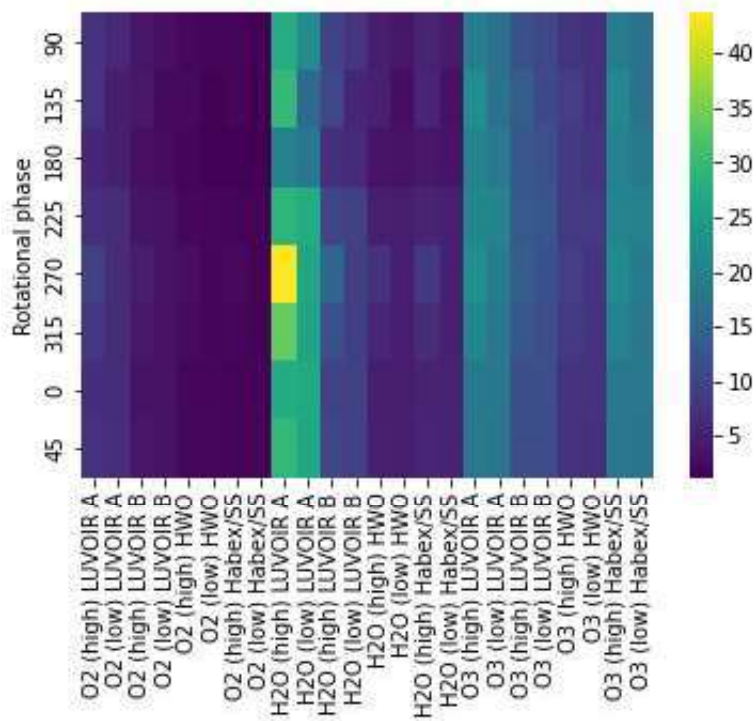
Figure 10.7: A comparison of the net SNRs for all the three gases, O_2 in the visible, H_2O in the nir and O_3 in the uv for atmospheres with high and low cloud coverage (as shown in the bracket) and for different mission concepts. The rotational phase of the disc is plotted along the y-axis.

Part IV

Discussion

Chapter 11

Summary and conclusions

To briefly summarize this work, we investigate the impact of clouds on the characterization of a remote Earth atmosphere. Specifically, we study how clouds impact the planet's spectrum and how they affect the detectability of atmospheric constituents including important bio-markers like O_2, H_2O and O_3. To construct our remote Earth, we use empirical data from the MODIS database which gives us the ground maps, and from the MERRA-2 database which gives us atmospheric coverage. We utilize the Planetary Spectrum Generator to simulate observations of this remote Earth and generate model spectra for various observational and instrumental configurations. From these model spectra, we compute Signal-to-Noise Ratios to quantify the detectability of atmospheric constituents.

Our results show that clouds are a very important component of a planet's atmosphere and they exert a significant impact on the spectrum as well as on the detectability of atmospheric constituents. Clouds significantly increase the albedo of the disc and enhance the continuum in the reflected light spectrum. Moreover, as the planet rotates and different portions of the disc face the observer, the distribution of clouds in the atmosphere at different rotational phases is the dominant factor that causes a variation in the model spectra. Through a simple radiative transfer model, we show that the SNRs are dependent on four factors - (i) the albedo of the cloud layer, (ii) the albedo of the surface, (iii) the absorptivity of the considered and gas and most importantly, (iv) the fraction of gas present above or below the cloud layer. All three bio-markers have significant abundances above the cloud layer, and thus the presence of clouds increases the albedo of the disc and subsequently, the SNR. Thus, clouds

significantly improve the detectability of these gases this shows that it is very important to consider the effect of clouds in retrieval models. Comparing all three gases, we find that it is easiest to detect the signature of H_2O in the near-infrared band, followed by O_3 in the uv and O_2 in the visible, assuming that the instrument has a full bandpass across the entire wavelength band. We also quantify the effects of aerosols of varying thicknesses present at different altitudes in the atmosphere on the detectability of O_2, H_2O and O_3. Considering O_2, we find that the SNRs increase with thickness for surface and low-level clouds, decrease with thickness for high-level clouds and remain roughly constant for mid-level clouds. This trend is shifted to lower altitudes for H_2O and to higher altitudes for O_3. Again, comparing all three gases, it is easier to detect H_2O in the presence of surface and low-level clouds while it is easier to detect O_3 in the presence of mid and high-level clouds.

A comparison of the observations at different orbital phases shows that the reflected light continuum increases as the planet moves closer to the star on the sky plane. This increases the strength of the absorption signal and in turn, the SNRs, thus making it easier to detect atmospheric constituents at higher orbital phases. There is a trade-off for making observations at high phases, if the planet is too close to the star, it vanishes inside the inner working angle of the coronagraph and cannot be characterized. We make all our observations assuming the planet is at quadrature where it is at the maximum angular separation from the star, and thus well outside the inner working angle.

We consider the impact of naturally varying cloud coverage on the characterization of the remote Earth atmosphere. We identify the most and the least cloudy days across a 16-year period from the MERRA-2 data, and construct our remote Earth atmosphere using empirical cloud coverage data from these days. As expected, higher cloud coverage increases the continuum in the reflected light spectrum and enhances the SNRs of important biomarkers. However, this means that any abundance of a gas inferred from the planet's spectrum is an apparent abundance since it varies with the amount of cloud cover. Thus, there is a degeneracy between the true abundance of a molecule and the amount of cloud cover, and removing this degeneracy seems to be a computationally expensive task as it involves running multiple retrieval models with different abundance values and cloud covers.

Finally, we evaluate the performance of four mission concepts, LUVOIR A/B, HWO, and Habex/SS in their ability to detect important biomarkers for atmospheres with high and low cloud coverage. As the mirror size of the instrument reduces, the collecting area decreases,

and thus the simulated noise increases. LUVOIR-A gives the highest SNRs for all three gases since it has the biggest mirror size. However, the SNRs do not simply scale with the mirror size and are dependent on other factors like the planetary and optical throughput. Considering an atmosphere with high cloud coverage, only LUVOIR-A has the capability to give individual SNRs > 5 for O2 and H2O with an exposure time of 3 hours. Thus, only LUVOIR-A can provide a confirmed detection of these gases in 3 hours, the rest of the mission concepts will need a longer exposure time to go beyond the golden standard of SNR=5. Since O3 has such a strong absorption signal in the uv band, all these mission concepts give SNRs > 5 and all of them can provide a confirmed detection of O3 with an exposure time of 3 hours. As outlined in the next section, we need to do a comparative analysis of the exposure times required to achieve an SNR of 5. These results stand as an important science pre-cursor for the HWO mission and will be vital in determining the instrumental and design parameters for the optimum performance of the mission.

Chapter 12

Future prospects

With the advent of the Habitable Worlds Observatory mission in the next decade or so, there are a lot of future prospects for research on the characterization of exoplanets and their atmospheres. Specifically considering this work, there is still a lot to be done to fully understand the effects of clouds on the characterization of exoplanet atmospheres and also to identify effective proxies for identifying the presence of clouds from spectra. We will discuss a few avenues which we are going to pursue in the future.

As shown in chapter 7, clouds of varying thickness present at different altitudes have significant impacts on the detectability of atmospheric constituents. However, we assumed these clouds to be composed of some molecule X independent of any gas present in the atmosphere. Even though this gives us a good theoretical estimate, it presents an unphysical scenario as the composition of the cloud layer cannot be independent of the atmospheric composition and temperature profile. Thus, we plan to model cloud layers in a physically consistent manner such that - (i) they are composed of water vapor and hence are not independent of the atmospheric composition and (ii) the optical thickness of each cloud layer will depend on the amount of water vapor present at that altitude which in turn is defined by the atmospheric temperature profile. Once, we construct these cloud layers, we will do a similar exercise of comparing the SNRs for different molecules.

All our observations have been made with an exposure time of 3 hours, So all the SNRs presented above are achieved with an exposure time of 3 hours. We show that for this

exposure time, only LUVOIR-A has the capability to give SNRs > 5 for O_2 and H_2O while all mission concepts can achieve SNRs > 5 for O_3 for an atmosphere with high cloud coverage. SNR = 5 is considered to be a gold standard for confirmed detection of a gas. In the future, we plan to run simulations at different exposure times and do a comparative analysis between the mission concepts of the exposure times required to achieve SNRs > 5. This analysis will inform observational strategies and design concepts for the HWO mission.

Finally, we want to highlight an important caveat in this work and how we hope to address it in the future. As mentioned before, all our SNRs have been calculated from the theoretical model spectrum. In this method, we subtract the gas from our model, take a difference of the spectra to get the signal, and divide it by the noise to compute the SNR. We cannot do this exercise to compute SNRs from an observed spectrum, since for an observation, we cannot artificially subtract the gas and in a few cases, we might not even know where the continuum lies. Moreover, as shown in 10.2, a real observation will have significant scatter just due to inherent noise from different sources. To compute SNRs from an observation, we run the observed spectrum through a retrieval framework which compares it to a best-fit model spectrum. This exercise can be used to estimate the abundance of different gases from the spectrum and subsequently calculate the SNRs. Due to the significant scatter in an observed spectrum, the SNRs obtained using this method will be lower than those obtained from the theoretical model spectrum. This means that all our SNRs presented above should be treated as optimistic best-case scenario estimates. We should always expect to do worse when we make real observations of such planets. We plan to address this issue by comparing the SNRs obtained from the theoretical model spectrum to the SNRs obtained from retrieval methods. This will help us understand how close the theoretical SNRs are to the SNRs which might be obtained from real observations and eventually prepare us to optimize the science yields of the HWO mission.

Appendix A

The MERRA-2 dataset

The Modern-Era Retrospective analysis for Research and Applications, Version 2 (MERRA-2) is a reanalysis dataset package that assimilates data collected from a variety of satellites orbiting Earth. The raw data collected by different satellites is processed by the Goddard Earth Observing System Model, Version 5 (GOES 5) which assimilates the data in a physically consistent manner and also converts the raw data into meteorologically relevant variables. The MERRA-2 dataset has several data components, each corresponding to different temporal resolutions, vertical layers, and atmospheric variables. Specifically, we use the M2I3VASM component which is a 3-dimensional data collection with a temporal resolution of 3 hours which means that satellite data is collected and assimilated every 3 hours resulting in 8 observations on a given day. The data is divided into 72 vertical model layers and the pressures corresponding to each layer are given in figure A.1.

The data is provided on a 0.625° longitude × 0.5° latitude horizontal grid. Thus there are M = 576 points in the longitude direction and N = 361 points in the latitude direction. The longitude λ and latitude ϕ can be determined from these grid points as follows:-

$$\lambda_i = -180 + (\Delta\lambda)(i-1) \ ; \ i = 1, M$$

$$\phi_i = -90 + (\Delta\phi)(j-1) \ ; \ j = 1, N$$

Level	P(hPa)	Lev	P(hPa)	Lev	P(hPa)	Lev	P(hPa)	Lev	P(hPa)	Lev	P(hPa)
1	0.0100	13	0.6168	25	9.2929	37	78.5123	49	450.000	61	820.000
2	0.0200	14	0.7951	26	11.2769	38	92.3657	50	487.500	62	835.000
3	0.0327	15	1.0194	27	13.6434	39	108.663	51	525.000	63	850.000
4	0.0476	16	1.3005	28	16.4571	40	127.837	52	562.500	64	865.000
5	0.0660	17	1.6508	29	19.7916	41	150.393	53	600.000	65	880.000
6	0.0893	18	2.0850	30	23.7304	42	176.930	54	637.500	66	895.000
7	0.1197	19	2.6202	31	28.3678	43	208.152	55	675.000	67	910.000
8	0.1595	20	3.2764	32	33.8100	44	244.875	56	700.000	68	925.000
9	0.2113	21	4.0766	33	40.1754	45	288.083	57	725.000	69	940.000
10	0.2785	22	5.0468	34	47.6439	46	337.500	58	750.000	70	955.000
11	0.3650	23	6.2168	35	56.3879	47	375.000	59	775.000	71	970.000
12	0.4758	24	7.6198	36	66.6034	48	412.500	60	800.000	72	985.000

Figure A.1: The pressures corresponding to each model layer in the M2I3VASM data component.

The relevant variables which are extracted from the dataset are - (i) atmospheric pressure, (ii) atmospheric temperature, (iii) eastward and northward wind, (iv) mass fraction of ozone and water vapor, and (v) mass fraction of liquid water and water-ice clouds. The mass fractions of ozone and water vapor define the vertical abundance profiles of the respective gases and the mass fractions of clouds provide a proxy for the abundance of clouds in different vertical layers throughout the atmosphere.

Appendix B

Supplementary figures
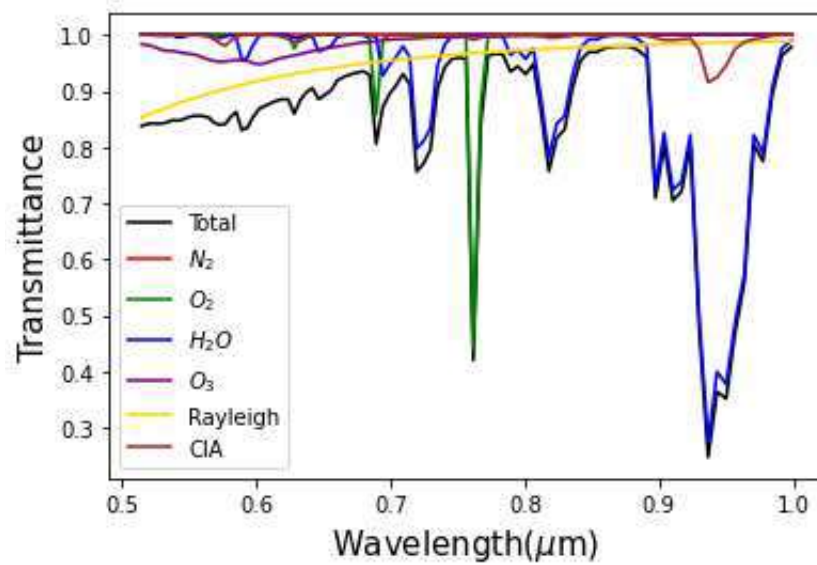
Figure B.1: Atmospheric transmittance of the dominant absorbers in the visible band, as computed by PSG.
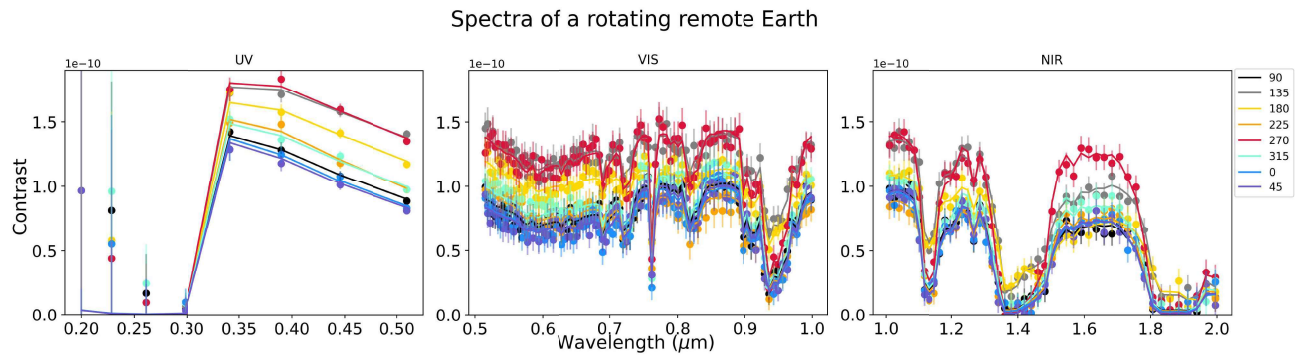
Figure B.2: Spectra of a rotating remote Earth as simulated with the LUVOIR-A mission concept. The different spectra are color-coded by the rotational phases. This plot is similar to figure 4.3 in section 3.1 with the dots and scatter included, which correspond to a real observation. There is still some disparity amongst the scatter which implies that the variation in the spectrum as a planet rotates might be detected, given there are no additional noise sources.
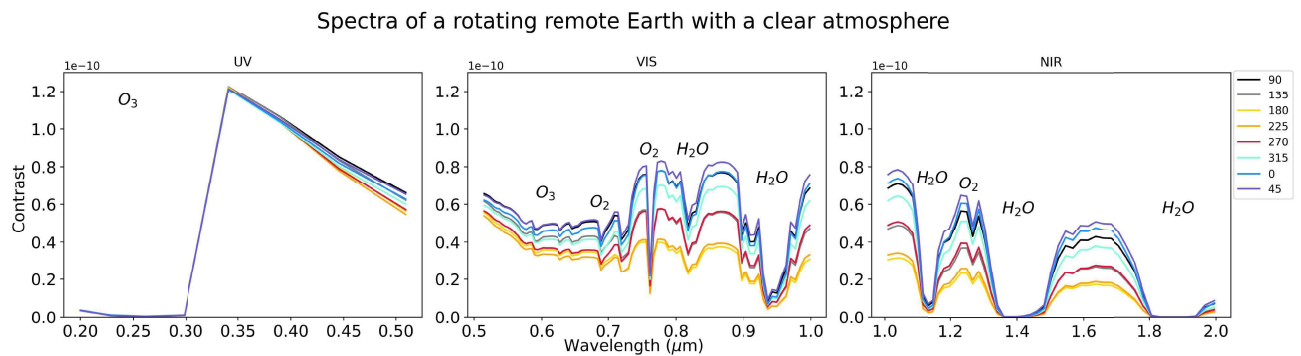
Figure B.3: Spectra of a rotating remote Earth for a clear atmosphere devoid of any clouds for all the eight configurations.
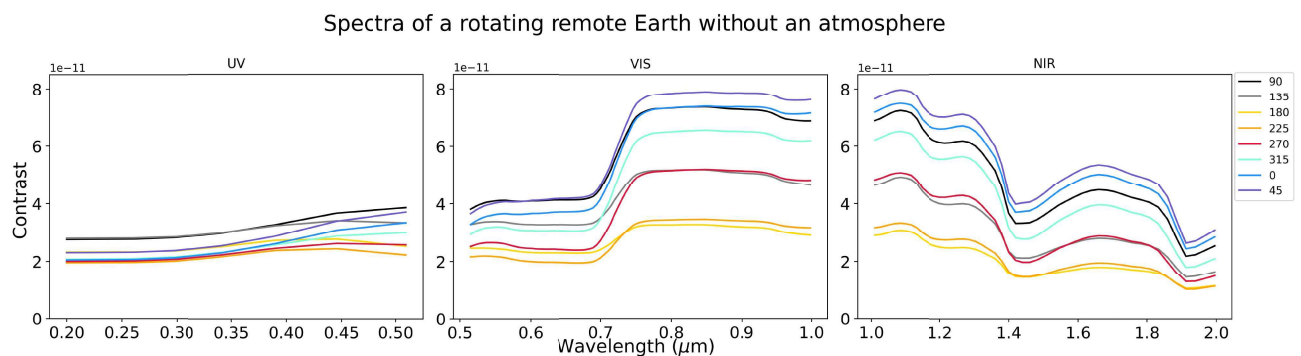
Figure B.4: Spectra of a rotating bare remote Earth without an atmosphere for all the eight configurations.
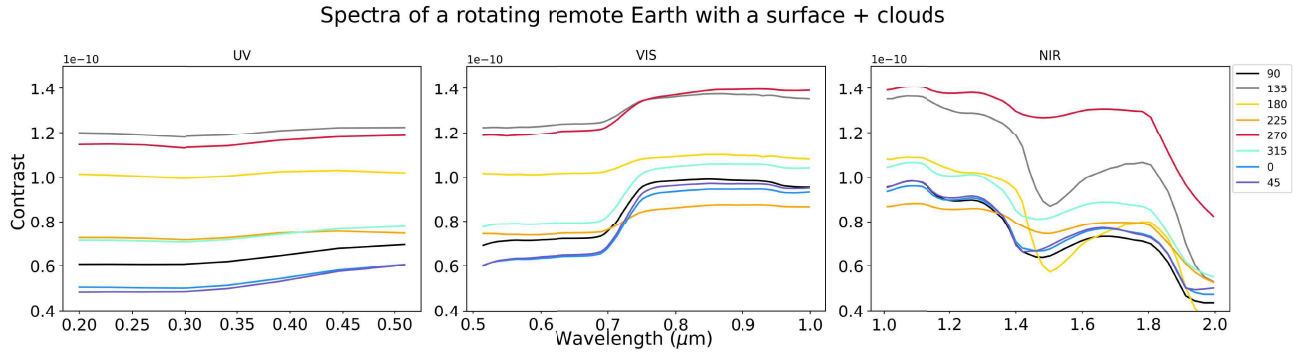
Figure B.5: Spectra of a rotating remote Earth with an atmosphere made up of just clouds and no gases for all the eight configurations.

(a)

(b)
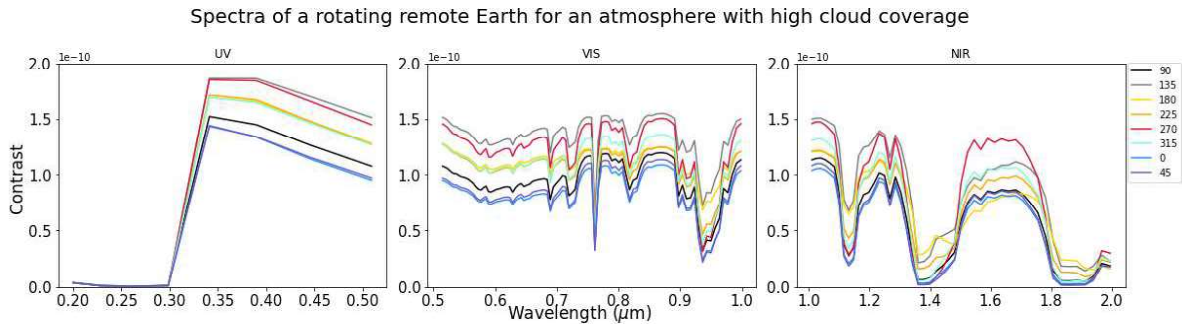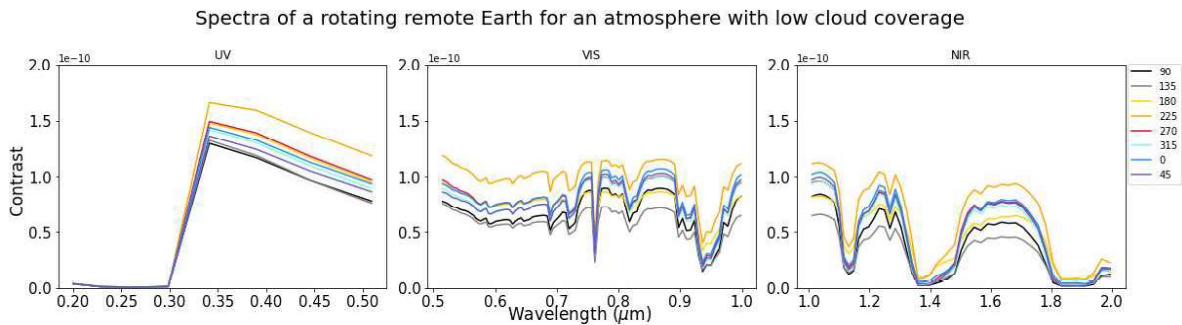
Figure B.6: Refletance spectra of a rotating remote Earth for atmosphere with (a) high and (b) low cloud coverage.

(a)

(b)

(c)
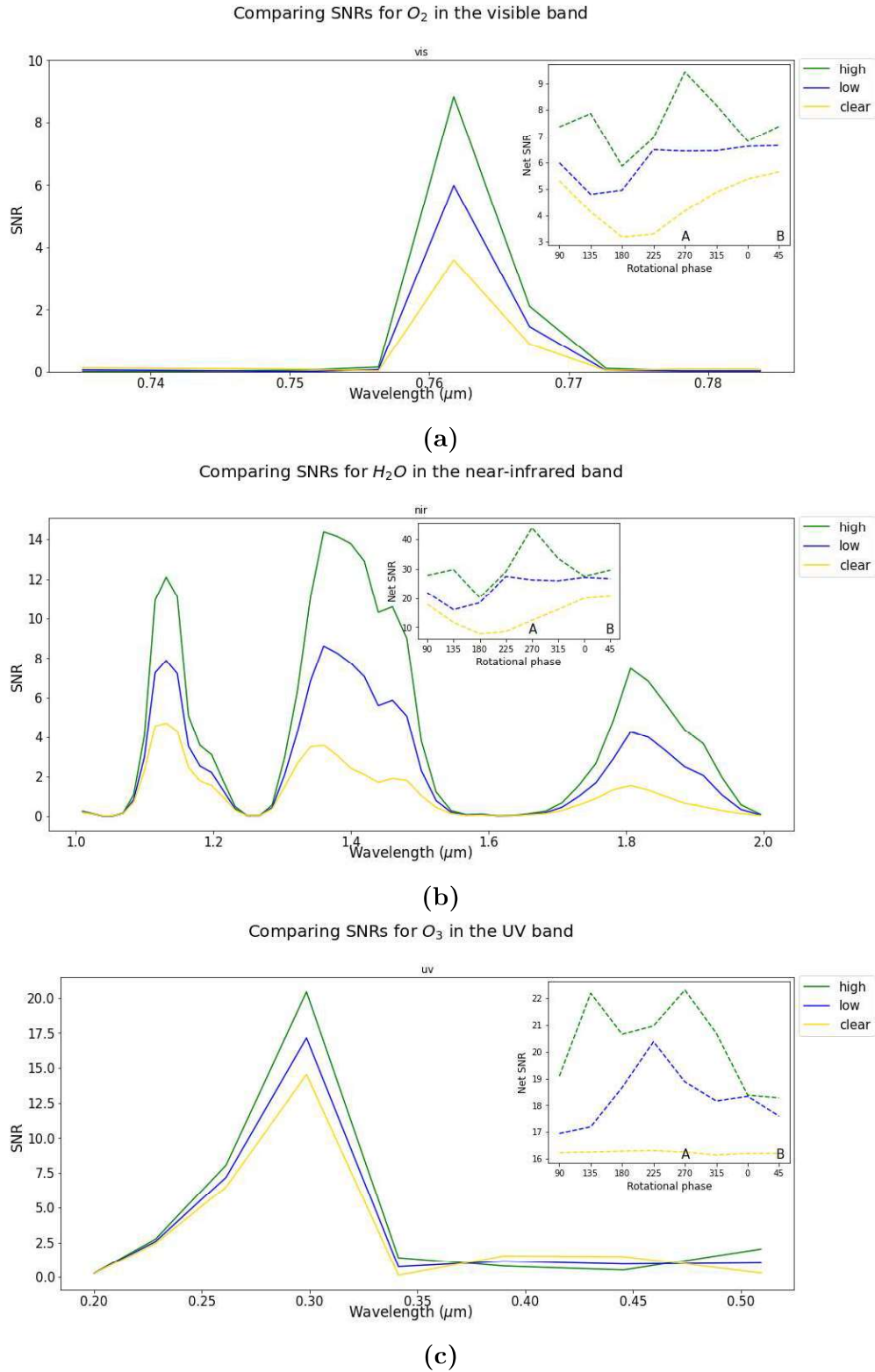
Figure B.7: The wavelength-dependent SNRs for (a) O_2 in the visible band centered around 0.76μm, (b) H_2O in the near-infrared band and (c) O_3 in the uv band for atmospheres with high/low and no cloud coverage. The insets show how the net SNRs evolve with rotational phase.

Comparing SNRs for O_2 in the visible band for disc A

(a)

Comparing SNRs for H_2O in the near-infrared band for disc A

(b)
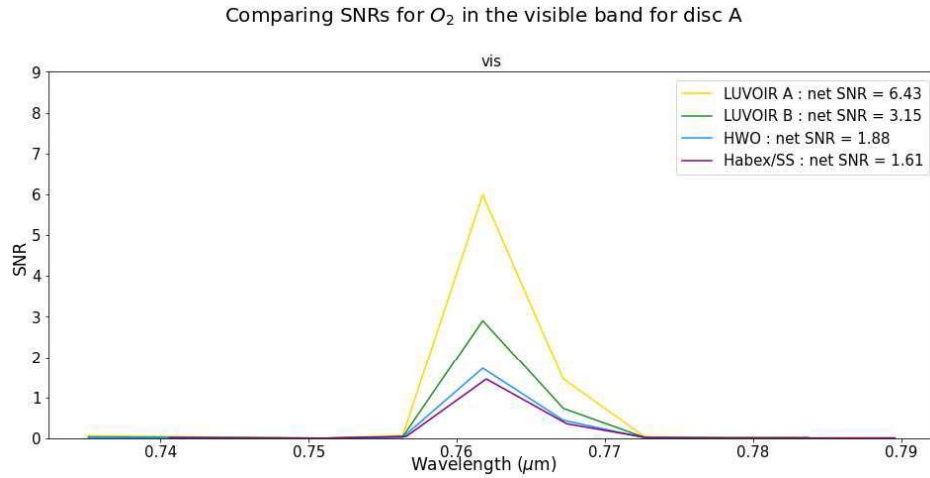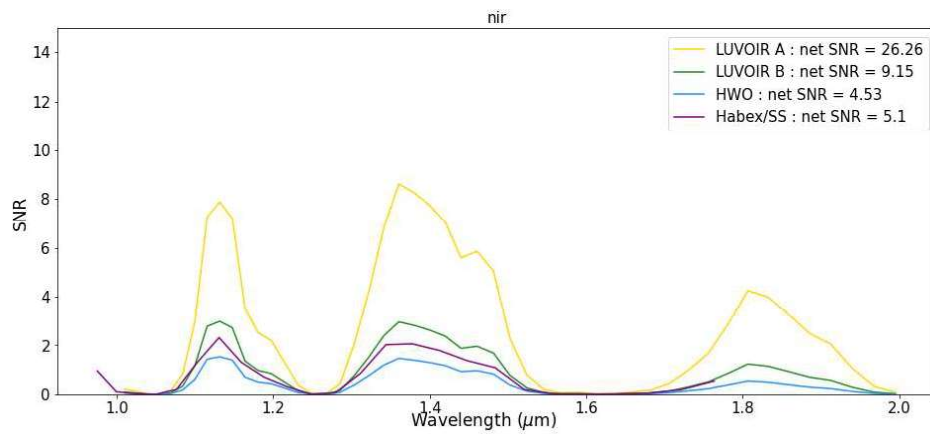
Comparing SNRs for O_3 in the uv band for disc A
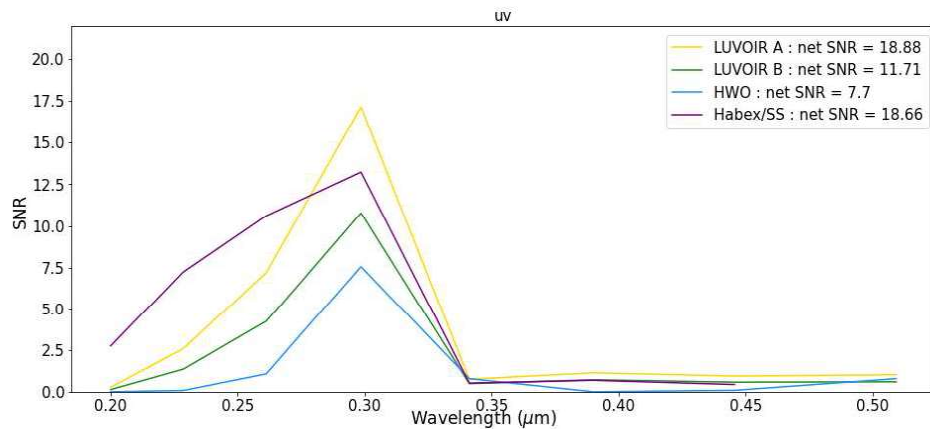
(c)

Figure B.8: The wavelength-dependent SNRs for (a) O_2 in the visible band centered around $0.76\mu m$, (b) H_2O in the near-infrared band and (c) O_3 in the uv band for disc A with an atmosphere with low cloud coverage. The net SNRs for the entire wavelength band are given in the legend.

References

Akeson, R.L., Chen, X., Ciardi, D., Crane, M., Good, J., Harbut, M., Jackson, E., Kane, S.R., Laity, A.C., Leifer, S., Lynn, M., McElroy, D.L., Papin, M., Plavchan, P., Ramírez, S.V., Rey, R., von Braun, K., Wittman, M., Abajian, M., ... Zhang, A. (2013). The nasa exoplanet archive: Data and tools for exoplanet research. *Publications of the Astronomical Society of the Pacific*, *125*(930), 989–999.

Arnold, L., Gillet, S., Lardière, O., Riaud, P., & Schneider, J. (2002). A test for the search for life on extrasolar planets: Looking for the terrestrial vegetation signature in the earthshine spectrum. *Astronomy amp; Astrophysics*, *392*(1), 231–237.

Batygin, K., & Laughlin, G. (2015). Jupiter's decisive role in the inner solar system's early evolution. *Proceedings of the National Academy of Sciences*, *112*(14), 4214–4217.

Brooke, T., Knacke, R., Encrenaz, T., Drossart, P., Crisp, D., & Feuchtgruber, H. (1998). Models of the iso 3-μm reflection spectrum of jupiter. *Icarus*, *136*(1), 1–13.

Buras, R., Dowling, T., & Emde, C. (2011). New secondary-scattering correction in disort with increased efficiency for forward scattering. *Journal of Quantitative Spectroscopy and Radiative Transfer*, *112*(12), 2028–2034.

Cahoy, K.L., Marley, M.S., & Fortney, J.J. (2010). Exoplanet albedo spectra and colors as a function of planet phase, separation, and metallicity. *The Astrophysical Journal*, *724*(1), 189–214.

Checlair, J.H., Villanueva, G.L., Hayworth, B.P., Olson, S.L., Komacek, T.D., Robinson, T.D., Popović, P., Yang, H., & Abbot, D.S. (2021). Probing the capability of future direct-imaging missions to spectrally constrain the frequency of earth-like planets. *The Astronomical Journal*, *161*(3), 150.

Dong, S., & Zhu, Z. (2013). Fast rise of "neptune-size" planets (4-8 $R_\oplus$) from p $\sim$ 10 to $\sim$ 250 days—statistics of kepler planet candidates up to $\sim$ 0.75 au. *The Astrophysical Journal*, *778*(1), 53.

Edwards, D. (1992). Genln2: A general line-by-line atmospheric transmittance and radiance model. version 3.0 description and users guide. *NCAR/TN-367-STR, National Center for Atmospheric Research, Boulder, Co.*

Fang, J., & Margot, J.-L. (2012). Architecture of planetary systems based on kepler data: Number of planets and coplanarity. *The Astrophysical Journal*, *761*(2), 92.

Friedl, M., & Sulla-Menashe, D. (2015). Mcd12c1 modis/terra+aqua land cover type yearly l3 global 0.05deg cmg v006 [data set]. *NASA EOSDIS Land Processes Distributed Active Archive Center.*

Gao, P., Wakeford, H.R., Moran, S.E., & Parmentier, V. (2021). Aerosols in exoplanet atmospheres.

Gaudi, B.S., Meyer, M., & Christiansen, J. (2021, October). The demographics of exoplanets. In *Exofrontiers*, IOP Publishing.

Gaudi, B.S., Seager, S., Mennesson, B., Kiessling, A., Warfield, K., Cahoy, K., Clarke, J.T., Domagal-Goldman, S., Feinberg, L., Guyon, O., et al. (2020). The habitable exoplanet observatory (habex) mission concept study final report. *arXiv preprint arXiv:2001.06683.*

Gelaro, R., McCarty, W., Suárez, M.J., Todling, R., Molod, A., Takacs, L., Randles, C.A., Darmenov, A., Bosilovich, M.G., Reichle, R., et al. (2017). The modern-era retrospective analysis for research and applications, version 2 (merra-2). *Journal of climate, 30*(14), 5419–5454.

Global Modeling and Assimilation Office (GMAO). (2015). MERRA-2 inst3_3d_asm_Nv: 3d,3-Hourly,Instantaneous, Model-Level, Assimilation, Assimilated Meteorological Fields V5.12.4.

Gordon, I.E., Rothman, L.S., Hargreaves, R., Hashemi, R., Karlovets, E.V., Skinner, F., Conway, E.K., Hill, C., Kochanov, R.V., Tan, Y., et al. (2022). The hitran2020 molecular spectroscopic database. *Journal of quantitative spectroscopy and radiative transfer, 277*, 107949.

Gordon, I.E., Rothman, L.S., Hill, C., Kochanov, R.V., Tan, Y., Bernath, P.F., Birk, M., Boudon, V., Campargue, A., Chance, K., et al. (2017). The hitran2016 molecular spectroscopic database. *Journal of Quantitative Spectroscopy and Radiative Transfer, 203*, 3–69.

Hamdani, S., Arnold, L., Foellmi, C., Berthier, J., Billeres, M., Briot, D., François, P., Riaud, P., & Schneider, J. (2006). Biomarkers in disk-averaged near-uv to near-ir earth spectra using earthshine observations. *Astronomy & Astrophysics, 460*(2), 617–624.

Hansen, J.E., & Hovenier, J. (1974). Interpretation of the polarization of venus. *Journal of Atmospheric Sciences, 31*(4), 1137–1160.

Hearty, T., Song, I., Kim, S., & Tinetti, G. (2009). Mid-infrared properties of disk averaged observations of earth with airs. *The Astrophysical Journal, 693*(2), 1763–1774.

Helling, C. (2019). Exoplanet clouds. *Annual Review of Earth and Planetary Sciences, 47*, 583–606.

Howard, A.W., Marcy, G.W., Bryson, S.T., Jenkins, J.M., Rowe, J.F., Batalha, N.M., Borucki, W.J., Koch, D.G., Dunham, E.W., Gautier, T.N., et al. (2012). Planet occurrence within 0.25 au of solar-type stars from kepler. *The Astrophysical Journal Supplement Series, 201*(2), 15.

Keller-Rudek, H., Moortgat, G.K., Sander, R., & Sörensen, R. (2013). The mpi-mainz uv/vis spectral atlas of gaseous molecules of atmospheric interest. *Earth System Science Data, 5*(2), 365–373.

Kitzmann, D., Patzer, A.B.C., von Paris, P., Godolt, M., & Rauer, H. (2011a). Clouds in the atmospheres of extrasolar planets: Iii. impact of low and high-level clouds on the reflection spectra of earth-like planets. *Astronomy amp; Astrophysics, 534*, A63.

Kitzmann, D., Patzer, A.B.C., von Paris, P., Godolt, M., & Rauer, H. (2011b). Clouds in the atmospheres of extrasolar planets: Ii. thermal emission spectra of earth-like planets influenced by low and high-level clouds. *Astronomy amp; Astrophysics, 531*, A62.

Kokaly, R., Clark, R., Swayze, G., Livo, K., Hoefen, T., Pearson, N., Wise, R., Benzel, W., Lowers, H., Driscoll, R., et al. (2017). Usgs spectral library version 7 data: Us geological survey data release. *United States Geological Survey (USGS): Reston, VA, USA, 61*.

Kopparapu, R., Arney, G., Haqq-Misra, J., Lustig-Yaeger, J., & Villanueva, G. (2021). Nitrogen dioxide pollution as a signature of extraterrestrial technology. *The Astrophysical Journal, 908*(2), 164.

Kopparapu, R.K., Hébrard, E., Belikov, R., Batalha, N.M., Mulders, G.D., Stark, C., Teal, D., Domagal-Goldman, S., & Mandell, A. (2018). Exoplanet classification and yield estimates for direct imaging missions. *The Astrophysical Journal, 856*(2), 122.

Kopparapu, R.K., Ramirez, R., Kasting, J.F., Eymet, V., Robinson, T.D., Mahadevan, S., Terrien, R.C., Domagal-Goldman, S., Meadows, V., & Deshpande, R. (2013). Habitable zones around main-sequence stars: New estimates. *The Astrophysical Journal, 765*(2), 131.

Kopparapu, R.K., Wolf, E.T., & Meadows, V.S. (2020). Characterizing exoplanet habitability. *Planetary Astrobiology, 449*.

Krissansen-Totton, J., Bergsman, D.S., & Catling, D.C. (2016). On detecting biospheres from chemical thermodynamic disequilibrium in planetary atmospheres. *Astrobiology, 16*(1), 39–67.

Krissansen-Totton, J., Olson, S., & Catling, D.C. (2018). Disequilibrium biosignatures over earth history and implications for detecting exoplanet life. *Science advances, 4*(1).

Lissauer, J.J., Dawson, R.I., & Tremaine, S. (2014). Advances in exoplanet science from kepler. *Nature, 513*(7518), 336–344.

Lustig-Yaeger, J., Meadows, V.S., & Lincowski, A.P. (2019). The detectability and characterization of the trappist-1 exoplanet atmospheres with jwst. *The Astronomical Journal, 158*(1), 27.

LUVOIR Team. (2019). The luvoir mission concept study final report. *arXiv preprint arXiv:1912.06219*.

Marley, M.S., Ackerman, A.S., Cuzzi, J.N., & Kitzmann, D. (2013). Clouds and hazes in exoplanet atmospheres. *Comparative climatology of terrestrial planets, 1*, 367–391.

Marley, M.S., Gelino, C., Stephens, D., Lunine, J.I., & Freedman, R. (1999). Reflected spectra and albedos of extrasolar giant planets. i. clear and cloudy atmospheres. *The Astrophysical Journal, 513*(2), 879.

Marois, C., Zuckerman, B., Konopacky, Q.M., Macintosh, B., & Barman, T. (2010). Images of a fourth planet orbiting hr 8799. *Nature, 468*(7327), 1080–1083.

Massie, S., & Hervig, M. (2013). Hitran 2012 refractive indices. *Journal of Quantitative Spectroscopy and Radiative Transfer, 130*, 373–380.

Mayor, M., & Queloz, D. (1995). A jupiter-mass companion to a solar-type star. *Nature, 378*(6555), 355–359.

Miguel, Y., Guilera, O.M., & Brunini, A. (2011). The diversity of planetary system architectures: Contrasting theory with observations. *Monthly Notices of the Royal Astronomical Society, 417*(1), 314–332.

Montanes-Rodriguez, P., Pallé, E., Goode, P., & Martín-Torres, F. (2006). Vegetation signature in the observed globally integrated spectrum of earth considering simultaneous cloud data: Applications for extrasolar planets. *The Astrophysical Journal, 651*(1), 544.

Montmessin, F., Gondet, B., Bibring, J.-P., Langevin, Y., Drossart, P., Forget, F., & Fouchet, T. (2007). Hyperspectral imaging of convective co2 ice clouds in the equatorial mesosphere of mars. *Journal of Geophysical Research: Planets, 112*(E11).

Nakajima, T., & Tanaka, M. (1988). Algorithms for radiative intensity calculations in moderately thick atmospheres using a truncation approximation. *Journal of Quantitative Spectroscopy and Radiative Transfer, 40*(1), 51–69.

National Academies of Sciences, E., & Medicine. (2023). *Pathways to discovery in astronomy and astrophysics for the 2020s* The National Academies Press.

Oklopčić, A., Hirata, C.M., & Heng, K. (2017). How does the shape of the stellar spectrum affect the raman scattering features in the albedo of exoplanets? *The Astrophysical Journal, 846*(2), 91.

Pollack, J.B., Rages, K., Baines, K.H., Bergstralh, J.T., Wenkert, D., & Danielson, G.E. (1986). Estimates of the bolometric albedos and radiation balance of uranus and neptune. *Icarus, 65*(2-3), 442–466.

Radley, C., Fueglistaler, S., & Donner, L. (2014). Cloud and radiative balance changes in response to enso in observations and models. *Journal of climate, 27*(9), 3100–3113.

Rossow, W.B., & Schiffer, R.A. (1999). Advances in understanding clouds from isccp. *Bulletin of the American Meteorological Society, 80*(11), 2261–2288.

Rothman, L.S., Gordon, I., Barber, R., Dothe, H., Gamache, R.R., Goldman, A., Perevalov, V., Tashkun, S., & Tennyson, J. (2010). Hitemp, the high-temperature molecular spectroscopic database. *Journal of Quantitative Spectroscopy and Radiative Transfer, 111*(15), 2139–2150.

Sahu, R.K., Choudhury, G., Vissa, N.K., Tyagi, B., & Nayak, S. (2022). The impact of el-niño and la-niña on the pre-monsoon convective systems over eastern india. *Atmosphere, 13*(8), 1261.

Sánchez-Lavega, A., Pérez-Hoyos, S., & Hueso, R. (2004). Clouds in planetary atmospheres: A useful application of the clausius–clapeyron equation. *American Journal of Physics, 72*(6), 767–774.

Schwieterman, E.W., Kiang, N.Y., Parenteau, M.N., Harman, C.E., DasSarma, S., Fisher, T.M., Arney, G.N., Hartnett, H.E., Reinhard, C.T., Olson, S.L., et al. (2018). Exoplanet biosignatures: A review of remotely detectable signs of life. *Astrobiology, 18*(6), 663–708.

Seager, S., Bains, W., & Hu, R. (2013). Biosignature gases in h2-dominated atmospheres on rocky exoplanets. *The Astrophysical Journal, 777*(2), 95.

Sneep, M., & Ubachs, W. (2005). Direct measurement of the rayleigh scattering cross section in various gases. *Journal of Quantitative Spectroscopy and Radiative Transfer, 92*(3), 293–310.

Stamnes, K., Tsay, S.-C., Wiscombe, W., & Jayaweera, K. (1988). Numerically stable algorithm for discrete-ordinate-method radiative transfer in multiple scattering and emitting layered media. *Applied optics, 27*(12), 2502–2509.

Stamnes, K., Tsay, S.-C., Wiscombe, W., & Laszlo, I. (2000). Disort, a general-purpose fortran program for discrete-ordinate-method radiative transfer in scattering and emitting layered media: Documentation of methodology.

Sudarsky, D., Burrows, A., & Hubeny, I. (2003). Theoretical spectra and atmospheres of extrasolar giant planets. *The Astrophysical Journal, 588*(2), 1121–1148.

Tinetti, G., Rashby, S., & Yung, Y.L. (2006a). Detectability of red-edge-shifted vegetation on terrestrial planets orbiting m stars. *The Astrophysical Journal, 644*(2), L129.

Tinetti, G., Rashby, S., & Yung, Y.L. (2006b). Detectability of red-edge-shifted vegetation on terrestrial planets orbiting m stars. *The Astrophysical Journal, 644*(2), L129.

Vasquez, M., Schreier, F., García, S.G., Kitzmann, D., Patzer, B., Rauer, H., & Trautmann, T. (2013). Infrared radiative transfer in atmospheres of earth-like planets around f, g, k, and m stars-ii. thermal emission spectra influenced by clouds. *Astronomy & Astrophysics, 557*, A46.

Villanueva, G.L., Smith, M.D., Protopapa, S., Faggi, S., & Mandell, A.M. (2018). Planetary spectrum generator: An accurate online radiative transfer suite for atmospheres, comets, small bodies and exoplanets. *Journal of Quantitative Spectroscopy and Radiative Transfer, 217*, 86–104.

Villanueva, G.L., Liuzzi, G., Faggi, S., Protopapa, S., Kofman, V., Fauchez, T., Stone, S.W., & Mandell, A.M. (2022). *Fundamentals of the Planetary Spectrum Generator*.

Villanueva, G., Mumma, M., Novak, R., Käufl, H., Hartogh, P., Encrenaz, T., Tokunaga, A., Khayat, A., & Smith, M. (2015). Strong water isotopic anomalies in the martian atmosphere: Probing current and ancient reservoirs. *Science, 348*(6231), 218–221.

Wiscombe, W. (1977). The delta–m method: Rapid yet accurate radiative flux calculations for strongly asymmetric phase functions. *Journal of Atmospheric Sciences, 34*(9), 1408–1422.

Wolff, M., Smith, M., Clancy, R., Arvidson, R., Kahre, M., Seelos Iv, F., Murchie, S., & Savijärvi, H. (2009). Wavelength dependence of dust aerosol single scattering albedo as observed by the compact reconnaissance imaging spectrometer. *Journal of Geophysical Research: Planets, 114*(E2).

Wolszczan, A., & Frail, D.A. (1992). A planetary system around the millisecond pulsar psr1257+ 12. *Nature,* *355*(6356), 145–147.

Yang, Y., Russell, L.M., Xu, L., Lou, S., Lamjiri, M.A., Somerville, R.C., Miller, A.J., Cayan, D.R., DeFlorio, M.J., Ghan, S.J., et al. (2016). Impacts of enso events on cloud radiative effects in preindustrial conditions: Changes in cloud fraction and their dependence on interactive aerosol emissions and concentrations. *Journal of Geophysical Research: Atmospheres, 121*(11), 6321–6335.

Youdin, A.N. (2011). The exoplanet census: A general method applied to kepler. *The Astrophysical Journal, 742*(1), 38.

Young, A.H., Knapp, K.R., Inamdar, A., Hankins, W., & Rossow, W.B. (2018). The international satellite cloud climatology project h-series climate data record product. *Earth System Science Data, 10*(1), 583–593.

Young, A., Robinson, T., Krissansen-Totton, J., Schwieterman, E.W., Wogan, N., Way, M., Sohl, L., Arney, G., Reinhard, C., Line, M., et al. (2023). Constraining chemical disequilibrium biosignatures for proterozoic earth-like exoplanets using reflectance spectra.

Young, A.V., Robinson, T.D., Krissansen-Totton, J., Schwieterman, E.W., Wogan, N.F., Way, M.J., Sohl, L.E., Arney, G.N., Reinhard, C.T., Line, M.R., et al. (2024). Inferring chemical disequilibrium biosignatures for proterozoic earth-like exoplanets. *Nature Astronomy, 8*(1), 101–110.